Experimental Investigation of Flow Structures in a Centrifugal Pump Impeller using Particle Image Velocimetry

Pedersen, Nicholas; Sørensen, Jens Nørkær; Larsen, Poul Scheel

Publication date:
2001

Document Version
Publisher's PDF, also known as Version of record

ET-PHD 2000-05

Experimental Investigation of Flow Structures in a Centrifugal Pump Impeller using Particle Image Velocimetry

by

Nicholas Pedersen

Dissertation submitted to Technical University of Denmark in partial fulfillment of the requirements for the degree of Doctor of Philosophy in Mechanical Engineering

Fluid Mechanics
Department of Energy Engineering
Technical University of Denmark
November, 2000

Fluid Mechanics
Department of Energy Engineering
Building 403
Technical University of Denmark
DK-2800 Lyngby, Denmark

Printed in Denmark by DTU-Tryk, Lyngby

ET-PHD 2000-05 / ISBN 87-7475-239-1

This thesis has been typeset using LaTeX2e.

Preface

This dissertation is submitted as a partial fulfillment of the requirements for the Ph.D. degree. The dissertation is based on research work carried out during the period September 1997 to November 2000 at the Department of Energy Engineering, Fluid Mechanics Section, at the Technical University of Denmark. The work has been carried out under the guidance of Professor, Ph.D. Poul Scheel Larsen of the Department of Energy Engineering and Project Manager, Ph.D. Christian Brix Jacobsen from Grundfos Management A/S. The study was partially supported by grants from Grundfos A/S, Bjerringbro, and the Technical University of Denmark.

I would like to express my deepest gratitude to my supervisors for their continuous support and inspiration. I also wish to thank my colleagues at the Fluid Mechanics Section for creating an open and friendly atmosphere. A special thank goes to Ulrik Ullum for many fruitful discussions and for keeping me company in the laboratory.

The Fluid Dynamic Engineering group at Grundfos Management A/S is deeply acknowledged for their kind assistance and interest in my work. My special thanks to Markus Lipp for his invaluable help in designing the impeller test rig.

I also express my gratitude to Poul Scheel Larsen and Lone Engen for hours of proof-reading.

Finally, I would like to thank Rikke for her love and her patience with me during the course of my study.

Technical University of Denmark
Copenhagen, November 2000

Nicholas Pedersen
M.Sc., Mech.Eng.

Abstract

The non-intrusive, instantaneous optical measurement technique, Particle Image Velocimetry (PIV), was applied to two physically complex flows of engineering relevancy, the flow past a square cylinder in uniform cross-flow and the flow within the passages of a rotating centrifugal pump impeller.

First, in order to demonstrate the feasibility of the PIV technique in an unsteady flow field, conditionally sampled velocity vector maps were collected in the near wake of a square cylinder in uniform cross-flow. Ensemble averaged flow statistics calculated at each of four equidistant phases of the vortex shedding cycle showed good qualitative agreement with previous experimental and numerical investigations. Based on the PIV data base, an experimental *a priori* test of five subgrid-scale (SGS) models used in Large Eddy Simulations of turbulent flows was performed. The study compared the measured instantaneous SGS stresses and SGS dissipation with the model predictions. Overall, the results were consistent with previous findings in simpler flows based on both experimental and DNS data, only now confirmed in a more complex flow.

The main part of the work concerned the application of PIV to the rotating passages of a medium specific-speed centrifugal pump impeller of industrial design. In order to allow optical access, the impeller was manufactured entirely in perspex. The experimental setup and technique proved to be efficient in providing reliable and detailed data over a full blade passage, also in the close vicinity of walls due to the use of fluorescent seeding. Measurements performed at the design operating point, $Q = Q_d$, showed a well-behaved vane congruent flow with no separation occurring, and revealed a distinct flow congruence between all six passages. The flow was dominated by rotational effects apart from local curvature effects in the inlet section.

The focus of the impeller investigation was to identify steady and unsteady flow features at severe off-design conditions. At quarter-load, $Q = 0.25Q_d$, a previously unreported steady 'two-channel' phenomenon consisting of alternate stalled and unstalled passages was observed, with distinct flow congruence between every second passage. A large high-turbulent recirculation cell blocked the inlet to the stalled passage and a strong relative eddy dominated the remaining parts of the passage causing backflow along the blade pressure side at large radii. The detected stall phenomenon was steady, non-rotating and not initiated via the interaction with stationary components.

A quantitative comparison of PIV blade-to-blade distributions of flow variables with LDV mean data showed a satisfactory agreement. Overall, it was concluded that the accuracy of flow statistics calculated by ensemble averaging a large number of instantaneous PIV samples is comparable to LDV. A significant advantage of using the PIV technique over LDV is the considerably reduced run times and the additional ability to identify instantaneous spatial flow structures.

Synopsis

Particle Image Velocimetry (PIV), der er en optisk måleteknik, er blevet anvendt i to fysisk komplekse strømninger af ingeniørmæssig relevans, strømningen bag en kvadratisk cylinder samt det interne strømningsfelt i en roterende centrifugalpumpe.

Først, med henblik på at illustrere PIV teknikkens velegnethed til måling af instationære strømninger, blev et stort antal konditioneret opsamlede hastighedsfelter optaget i kølvandet bag en kvadratisk cylinder placeret i et ensformigt hastighedsfelt. Ensemble midlede data, beregnet for hver af fire ækvidistante faser af hvirvelprocessen, viste god overensstemmelse med tidligere eksperimentelle og numeriske undersøgelser. Baseret på denne PIV database foretoges en eksperimentel *a priori* test af fem subgrid-skala (SGS) modelller som anvendes i Large Eddy Simuleringer af turbulente strømninger. Undersøgelsen sammenlignede målte, øjeblikkelige SGS spændinger samt SGS dissipation med modelforudsigelserne. Resultaterne var generelt i god overensstemmelse med tidligere undersøgelser i simple strømninger baseret på både eksperimentelle og DNS data, og er nu også bekræftet i en mere kompleks strømning.

Hoveddelen af arbejdet omhandlede anvendelsen af PIV til at måle hastighedsfeltet i skovlkanalerne i en centrifugalpumpe med medium specifikt omløbstal og af industrielt design. For at muliggøre optisk adgang, var hele løbehjulet fremstillet i plexiglas. Forsøgsopstillingen viste sig effektiv til at bibringe pålidelige og detaljerede data over en hel kanal, også i umiddelbar nærhed af væggene, som følge af brugen af flourescerende seeding. Målinger udført i designpunktet, $Q = Q_d$, viste en skovlkongruent strømning uden separationseffekter, og viste kongruens mellem strømningen i alle 6 kanaler. Strømningen var domineret af rotationseffekter undtagen i indløbet.

Et hovedformål med pumpeundersøgelserne var en identifikation af stationære og instationære strømningseffekter optrædende under drift langt fra designpunktet. Ved kvart-last, $Q = 0.25Q_d$, observeredes et hidtil urapporteret stationært 'to-kanals'-fænomen bestående af skiftevis afløste og ikke-afløste kanaler. Strømningen i hver anden kanal var kongruent. En stor høj-turbulent recirkulationszone blokerede indløbet til den afløste kanal og en stærk potentialhvirvel dominerede den resterende del af kanalen, og gav ved udløbet anledning til tilbagestrømning langs skovlblades trykside. Det detekterede afløsningsfænomen var stationært, ikke-roterende og ikke initieret via interaktion med stationære komponenter.

En kvantitativ sammenligning af PIV strømningsvariable med LDA middeldata viste en tilfredsstillende overensstemmelse. En generel konklusion var, at nøjagtigheden af strømningsstatistik beregnet via ensemble-midling af et stort antal individuelle PIV hastighedsfelter er sammenlignelig med det opnåelige med LDA. En betydelig fordel ved at anvende PIV teknikken i forhold til LDA er en anselig tidsreduktion og muligheden for at identificere øjeblikkelige spatiale strømningsstrukturer.

Contents

Chapter 1

Introduction

Centrifugal pumps are used in a wide variety of engineering applications ranging from water circulation in domestic houses to fuel supply in space crafts. Although its operating principle of employing centrifugal effects to increase fluid pressure has been in use for more than a century, many details of the complex internal flow field that develops in a centrifugal impeller are still not very well understood. Not only is the flow turbulent, it is also influenced by the combined effects of curvature, separation and system rotation and is, furthermore, often unsteady. Due to this inherent complexity, the development in the hydraulic design of pump impellers has to a large extent relied on empirical correlations, acquired through systematic model testings and simplified theoretical considerations, as well as on the experience and intuition of the designer. Over the years, as new models have emerged from gradual improvements of existing types of designs, this has resulted in reliable and quite efficient pumps.

During this process, much fundamental knowledge of the physical phenomena that govern the impeller flow has been gained from experimental and numerical techniques that consider the flow field as steady and thus only depict the time-averaged flow field. Experimental methods of this type include one-point techniques such as pressure probes, hot-wire anemometry and Laser Doppler Velocimetry (LDV). In fact, the non-intrusive character of LDV represented a break-through in turbomachinery measurement techniques and LDV is now routinely employed in industry. This has been paralleled with significant advances in the numerical simulation of engineering flows using statistical turbulence models based on the Reynolds-averaged Navier Stokes (RANS) equations. As a result, mean methods of both experimental and numerical nature have been incorporated into the pump design cycle and have shown to provide reliable information on both global performance data such as pressure rise and efficiency and on the main characteristics of the velocity field. Therefore, mean techniques will probably continue to be the preferred design and analysis tool for years to come.

However, the quest for more efficient, more reliable and more flexible products raises the need for a more detailed knowledge of the local and instantaneous features of the internal flow in pump impellers. As well as attaining high efficiencies it is desirable to make the machine less sensitive to off-design operation. In order to meet these challenging requirements the designers have to look more and more to the three-dimensional unsteady aspects of the flow. It is well-known that the RANS turbulence models, e.g. the $k - \epsilon$ model, have difficulties in predicting flows where separation and curvature

effects are important [101]. Also, the averaging over long data records prohibit experimental techniques such as LDV of measuring unsteady phenomena associated with e.g. rotor-stator interaction and rotating stall which may seriously deteriorate the pump performance. Therefore, a more complete picture of the flow physics relies on the development and application of both experimental and numerical methods that incorporate a description of the unsteady features of the flow.

1.1 Unsteady techniques

Particle Image Velocimetry (PIV) is a rapidly evolving optical technique that measures the instantaneous velocity field in a two-dimensional plane of a flow field. The technique hence enables the identification of instantaneous spatial flow structures but, at the same time, also offers the calculation of turbulence statistics by ensemble averaging a large number of independent samples. Consequently, both steady and unsteady flow phenomena may be investigated with PIV. Furthermore, because PIV measures an entire plane simultaneously, it reduces acquisition times considerably compared to one-point techniques and therefore represents a powerful alternative or supplement to LDV. The temporal resolution attainable with PIV is, however, still restricted by current hardware technology which does not allow to resolve the fast time scales present in most industrial flows. Nevertheless, the ability to provide snapshots of the unsteady spatial flow structures has made PIV attractive for the study of a variety of flows. Within the last few years, the technique has also been applied to numerous engineering flows, see Grant [39] for an overview.

On the numerical side, there has been a parallel development of the unsteady Large Eddy Simulation (LES) technique which may be considered the numerical counterpart of PIV. While RANS models have proved inadequate and resolution requirements at the same time prohibit the use of Direct Numerical Simulations (DNS) in most engineering applications, this intermediate approach is rapidly growing. Conceptually, the LES technique is suitable for the prediction of complex unsteady flows because it resolves the large energy-carrying scales, whereas only the small scales are modeled. As these are more universal and homogeneous, this gives hope of allowing a single simple model, a socalled subgrid-scale (SGS) model, to represent them in all situations. However, LES has traditionally been used mostly as an academic tool for turbulence research, and the move towards industrial applications therefore requires a careful evaluation of the LES results and of the SGS models themselves, see e.g. Byskov [17].

1.2 PIV and LES as complementary tools

As both PIV and LES are instantaneous whole-field techniques, a fruitful symbiosis between these two techniques will certainly be established in the near future. As a contribution to this end, and in order to demonstrate the feasibility of the PIV technique in an unsteady flow with complex physics, the first part of the present work was concerned with PIV measurements of the two-dimensional flow past a square cylinder in uniform cross-flow. This flow has served as a workshop testcase for LES studies [102] and a large body of data is therefore available for comparing the velocity fields

and derived quantities attained with PIV and LES, respectively. However, the present aim was not to perform such an *a posteriori* comparison, but rather to use the instantaneous PIV data in order to evaluate the performance of five commonly used SGS models *a priori*, i.e. at model level. This experimental test compares the measured subgrid-scale quantities with those predicted by the SGS models. This gives indications on the abilities of the models to predict a flow involving separation and periodic unsteadiness, as is also typical for the flow field encountered in centrifugal impellers.

1.3 PIV in turbomachinery

Following this feasibility study of the PIV technique in a complex unsteady flow field, the main part of the present work concerned the application of PIV to the rotating passages of a centrifugal pump impeller. Although the last decade has shown various applications of PIV and related techniques to rotating machinery covering both pumps, fans and compressors, as discussed in a recent review by Wernet [121], most PIV studies in pumps have focused on the flow in the stationary components of the pump stage, i.e. diffusers or volutes. PIV measurements inside the rotating passages themselves are very scarce, and in the few cases known to the author, the investigations have been confined to simple model geometries [89, 46, 8] and have, furthermore, not focused on the instantaneous flow structures.

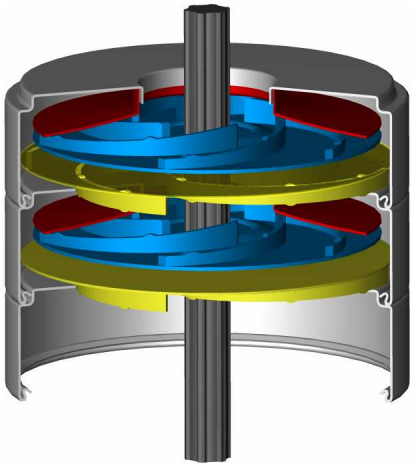

Figure 1.1: *Two stages of a multi-stage pump illustrating the shrouded centrifugal pump impeller under study [40].*

Therefore, with the purpose of gaining more detailed knowledge of the complex flow phenomena that develop in a centrifugal impeller at design as well as at severe off-design operating conditions, the present study concerned the acquisition of PIV data in the shrouded impeller geometry illustrated in figure 1.1. The figure shows two stages of a multi-stage pump typically used for water distribution and pressure boosting in industry. Each stage consists of a rotating impeller, the Grundfos CR4 [40], and a stationary return channel that guides the fluid to the next pump stage. In order to allow optical access, the present measurements were undertaken in a specially designed test rig with a scaled CR4 model impeller manufactured entirely in perspex.

1.4 Objectives of work

Summarizing the discussions above, the objectives of the present work may be divided into two categories. Firstly, PIV measurements of the near wake of the unsteady flow past a square cylinder in uniform cross-flow were performed. The objectives were:

- to demonstrate the feasibility of the PIV technique to provide details of the instantaneous spatial structures, as well as reliable turbulence statistics, in a complex flow involving separation and periodic unsteadiness
- to use planar PIV data as a tool for an *a priori* evaluation of subgrid-scale models used in Large Eddy Simulations of turbulent flows.

Secondly, the main part of the work concerned the application of PIV to a centrifugal pump impeller. The objectives were:

- to provide detailed instantaneous data of the flow field in the rotating passages of a centrifugal pump impeller of industrial design
- to investigate steady and unsteady flow phenomena occurring at both design and severe off-design conditions
- to assess the accuracy of ensemble averaged PIV data by comparison with LDV data acquired under the same operating conditions
- to study the nature of the flow distortion induced by rotor-stator interaction between the impeller vanes and a stationary vaned diffuser

As a last point the optical impeller measurements also served to establish a detailed database that allows an *a posteriori* evaluation of a recent Large Eddy Simulation performed by Byskov [18] of the present impeller flow.

1.5 Outline of the dissertation

The dissertation is organized into three parts.

Part A, consisting of Chapter 2, gives a general introduction to the PIV technique. Experimental design rules are provided and measurement uncertainty limits discussed.

Part B concerns the PIV measurements of the flow past a square cylinder. Chapter 3 presents the instantaneous and ensemble-averaged PIV data and describes the complex flow field whereas Chapter 4 focuses on the use of these data for the evaluation of subgrid-scale models used in LES.

Part C, the main part of the dissertation, concerns the PIV measurements performed in a centrifugal pump impeller. Chapter 5 gives a brief overview of the theory of pump flows with the aim of identifying flow phenomena related to off-design operation. Chapter 6 presents the experimental setup and gives details of the PIV and LDV measurement procedures and data analysis methods. Chapter 7 presents the PIV results, focusing on an identification of the qualitative features of the flow. Chapter 8 performs a more quantitative analysis and compares the PIV data with LDV data and with recent LES results obtained by Byskov [18] in the same impeller flow.

Finally, chapter 9 draws general conclusions and discusses the future perspectives of the study.

Part A

PIV

Chapter 2

Particle Image Velocimetry

Particle Image Velocimetry (PIV) is a non-intrusive optical measurement technique that enables the mapping of instantaneous velocity distributions within planar cross-sections of a flow field. This powerful approach to flow measurement has undergone tremendous development since it was first recognized as a separate method in the early 1980s [2]. This chapter describes the principle and basic system components of the PIV technique with the focus on digital cross-correlation PIV which is the technique used in the present work. Important parameters that should be observed and optimized in each of the four individual steps of the PIV technique are described, and a set of experimental design rules are given. The factors that determine the measurement uncertainty and limit the attainable dynamic ranges of velocity and spatial resolution are also discussed. Finally, the subject of post-processing PIV data in order to derive the out-of-plane vorticity component and turbulence statistics is briefly discussed.

2.1 Introduction

The rapid evolution of PIV within the last decade has relied on parallel developments in optics, pulsed lasers, computers and digital recording and image analysis methods. Originally based on photographic recordings, the predominant variant of the technique today is digital particle image velocimetry (DPIV) which was introduced in the early 1990s by Willert and Gharib [127] and Westerweel [122]. In DPIV, images are acquired digitally and analyzed computationally, eliminating all photographic or opto-mechanical processing steps. This has lead to a speed-up of processing times of about two orders of magnitude and has made it feasible to study flow statistics with this quantitative visualization technique. Furthermore, the appearance of integrated commercial PIV systems has spread the measurement technique from academic fluid dynamics laboratories to industry. Grant [39] provides a general overview of the development stages and various perturbations of the PIV technique and also describes the wide spectrum of applications that PIV is used for today, ranging from geometrically simple flow configurations for the study of turbulence to highly specialized engineering applications.

2.1.1 Principle

The basic principle of PIV is quite simple and consists of four general steps as shown in figure 2.1. The flow field is seeded with small tracer particles (seeding) and illuminated

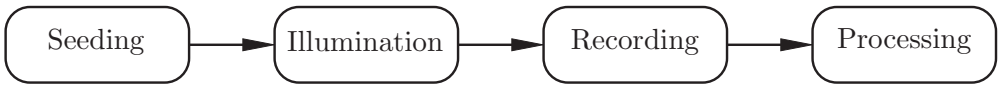

Figure 2.1: *The four general steps of the PIV technique.*

by a plane light sheet. The sheet is pulsed at two very closely spaced instants in time and the light scattered from the particles is recorded either on a single photographic negative or, in DPIV, on two separate frames on a digital CCD camera, placed at right angles to the light sheet. The data processing stage consists of subdividing the recorded image into small interrogation areas and subsequently determine the average particle image displacement $\Delta\vec{X}$ in each region. This distance and knowledge of the time interval Δt between the two pulses and the magnification M between the illumination and recording planes then allows the calculation of the instantaneous velocity field, $\vec{u} = \Delta\vec{X}/M\Delta t$.

2.1.2 Image modes

Three different modes of PIV may be distinguished depending on the particle image density. To quantify this, Adrian [2] defined a dimensionless source density as

$$N_S = C\Delta z_0 \frac{\pi}{4}\frac{d_t^2}{M^2} \tag{2.1}$$

where C is the number of tracer particles per unit volume, Δz_0 is the light sheet thickness and d_t the particle image diameter. At low particle density ($N_S \ll 1$), the distance between individual particles is much larger than the particle diameter and distinct particle pairs may therefore be identified and tracked between the two images. This mode of operation is therefore referred to as Particle Tracking Velocimetry (PTV). In the case of very high seeding concentration ($N_S \gg 1$), individual particles overlap and a speckle pattern will form when illuminated by a coherent light source. This is the situation encountered in Laser Speckle Velocimetry (LSV).

The normal operating mode for PIV is characterized by medium particle density. In this case individual particle images are still visible but it is no longer possible to identify matching particle pairs. Rather than trying to track each individual particle, a statistical approach is therefore applied, as will be explained later. It may be noted that although PIV is referred to as a quantitative visualization technique, a purely visual inspection of a PIV image does not reveal much of the underlying flow structures. The reason is that a successful velocity evaluation requires a homogeneous distribution of tracer particles. This is contrary to traditional visualization techniques that rely on an inhomogeneous or local distribution of tracer particles, e.g. dye, to make flow structures visible.

2.2 PIV setup

A brief description of the PIV system components associated with each of the four steps shown in figure 2.1 is given below. The emphasis is on providing generally applicable guidelines for proper setup of a PIV experiment. The discussion will focus on cross-correlation DPIV, although the more general acronym PIV will be maintained. For a thorough description of the individual system components, including a discussion of photographic PIV, the reader is referred to the recent book on PIV by Raffel et al. [99] and references therein.

2.2.1 Seeding

As the seeding particles suspended in the fluid take the role as the actual velocity probes, they should in fact be considered part of the instrumentation hardware. It has already been noted that a uniform and sufficiently high concentration of flow seeding is a prerequisite for any PIV experiment, and another equally important requirement is to avoid slip between the particles and the flow field of interest. The seeding particles should therefore, ideally, be neutrally buoyant and as small as possible, yet large enough to scatter sufficient light. A compromise between reducing the particle size to improve flow tracking and increasing the particle size to improve light scattering is thus necessary. In the present work, however, the tracking characteristics of the particles are of greater concern and this subject is therefore considered below.

Tracking characteristics

The specification of limits on the diameter d_p and density ρ_p of seeding particles is usually based on their ability to faithfully follow spatial and temporal gradients in the flow. This may be quantified in terms of the slip velocity which is the instantaneous velocity $\Delta u = u_p - u_f$ of the particle (index p) relative to the fluid (index f), and the cut-off frequency f_c which is a measure of the fastest turbulent fluctuations that the particles can follow within a certain accuracy. To estimate how the physical properties of the seeding particles influence these two parameters, Eq. (2.2) is often used as a starting point. It describes the unsteady motion of a spherical particle suspended in a turbulent fluid and was derived by Basset in 1888 (see also e.g. Melling [76]):

$$\underbrace{\frac{\pi d_p^3}{6}\,\rho_p \frac{du_p}{dt} \;=\; -3\pi\rho_f \nu d_p\,\Delta u}_{\text{Stokes' drag law}} + \frac{\pi d_p^3}{6}\,\rho_p \frac{du_f}{dt} \;-\; \frac{1}{2}\frac{\pi d_p^3}{6}\,\rho_p \frac{d(\Delta u)}{dt} \;-\; F_{hist} \qquad (2.2)$$

where ρ_f and ν are the density and kinematic viscosity of the fluid, respectively, and body forces have been neglected. The first two terms of Eq. (2.2) are the acceleration force and viscous resistance, respectively, equivalent to Stokes' drag law. The third term is the pressure gradient force and the fourth term is known as the added mass and represents the fluid resistance to the accelerating sphere. The final term, F_{hist}, is the so-called Basset history integral which defines the resistance caused by the unsteadiness of the flow field [76].

An extensive discussion of Eq. (2.2) and its solution for turbulent flow under different conditions has been given by Mei [75]. Solutions may e.g. be expressed in terms

of the relative amplitude and phase response of the instantaneous fluid and particle motions [49] or as the ratio of the fluctuating energies of the time-averaged motions [20]. Qualitatively, the solutions are dictated by the density ratio $R = \rho_p/\rho_f$ between the particle and fluid which, in turn, depends on whether the experiment is performed in a gas or a liquid.

Large density ratios

For liquid or solid particles suspended in gases, corresponding to PIV experiments in air, R is normally of the order 10^3 and Eq. (2.2) reduces to Stokes' drag law which is the equation of particle motion in the limit of creeping flow. In this case the velocity slip may be estimated from

$$\Delta u = -\frac{d_p^2 R}{18\nu}\,\frac{du_p}{dt} = \tau_p\,\frac{du_p}{dt} \tag{2.3}$$

provided the acceleration du_p/dt is known. The relaxation time $\tau_p = d_p^2 R/18\nu$ is a measure of the characteristic response time of the particles to velocity changes in the fluid which are typically assumed exponentially [99]. The ratio between τ_p and a characteristic time scale τ_f for the turbulence in the fluid, e.g. the Kolmogorov time scale, defines the Stokes' number $S = \tau_p/\tau_f$.

In order to estimate the cut-off frequency f_c of seeding particles, Mei [75] considered the unsteady drag on a stationary sphere experiencing a high-frequency oscillation of the fluid flow $u(t) = \tilde{u}(\omega)e^{-i\omega t}$ in which $\tilde{u}(\omega)$ is the amplitude of the velocity fluctuation with angular frequency ω. Mei [75] then showed that the energy transfer function is given by

$$|H(\omega)|^2 = |H(S_\varepsilon)|^2 = \frac{(1+S_\varepsilon)^2 + (S_\varepsilon + \frac{2}{3}\,S_\varepsilon^2)^2}{(1+S_\varepsilon)^2 + [S_\varepsilon + \frac{2}{3}\,S_\varepsilon^2 + \frac{4}{9}(R-1)S_\varepsilon^2]^2} \tag{2.4}$$

where $H(\omega)$ is the frequency response function of the particle and $S_\varepsilon = d_p\,\sqrt{\omega/8\nu}$ is a Stokes number. Defining cut-off frequencies of the particle based on either 50% or 200% energy response, $S_{\varepsilon,c} = \{S_\varepsilon : |H(S_\varepsilon)|^2 = 1/2 \text{ or } 2\}$, the cut-off Stokes' number $S_{\varepsilon,c}$ can be obtained from Eq. (2.4) as a function of the density ratio R. For this purpose Mei [75] provided the following interpolation formula:

$$S_{\varepsilon,c} \approx \left[\left(\frac{3}{2R^{1/2}}\right)^{1.05} + \left(\frac{0.932}{R-1.621}\right)^{1.05}\right]^{1/1.05} \qquad \text{for } R > 1.621 \tag{2.5}$$

This, finally, allows the cut-off frequency of the particle to be estimated from

$$f_c \approx \frac{\nu}{\pi}\left(\frac{2S_{\varepsilon,c}}{d_p}\right)^2 \tag{2.6}$$

Eq. (2.6) will be used in section 3.2 to estimate f_c for the particles used in the PIV measurements of the air flow past a square cylinder. A survey by Melling [76] of a range of seeding materials showed that a diameter of 2–3 μm is generally acceptable for a frequency response of 1 kHz, requiring that the particles follow the fluid motion within 1%. A better frequency response up to 10 kHz generally requires particle diameters not exceeding 1 μm.

Small density ratios

For small particles with a density close to that of the fluid, which is the typical situation encountered when performing PIV measurements in water, Eq. (2.2) is more difficult to solve. Furthermore, body forces which were explicitly neglected in Eq. (2.2) may be of importance. Hence, Agüí and Jiménez [5] alternatively applied the concept of the energy transfer function and found that the tracking error of the velocity may be estimated from

$$\frac{|\Delta u|^2}{|u_f|^2} \approx 0.018 \frac{(R-1)^2}{S_0^2} \tag{2.7}$$

where S_0 is a Stokes number defined as $S_0 = d_p\sqrt{\nu/\omega_0}$ and $\omega_0 = 2\pi f_0$ is the angular frequency of the turbulence fluctuations associated with the typical eddy frequency f_0. This gives the following estimate of the slip velocity for small density ratios [27]:

$$\left(\frac{\Delta u}{u_f}\right)^2 \approx \left(\frac{\rho_p - \rho_f}{\rho_f}\right)^2 \frac{d_p^2\, f_0}{9\,\nu} \tag{2.8}$$

Eq. (2.8) will be used in section 6.4.2 to estimate the slip velocity associated with the seeding particles used in the centrifugal impeller measurements.

2.2.2 Illumination and recording

A pulsed double-cavity Nd:YAG laser is generally required in PIV to provide sufficient illumination energy in short duration pulses to record unblurred images of the particles in the flow. The pulsing laser beams are manipulated into a two-dimensional light-sheet by cylindrical and spherical lenses, see e.g. Stanislas and Monnier [111] for practical guidelines on the optical setup.

In the prevailing PIV variant today, cross-correlation DPIV, the light scattered from the illuminated particles is recorded on digital cameras with light-sensitive CCD sensors that sample the light intensity over small areas referred to as pixels. These cross correlation cameras store the two exposures on separate frames and thereby eliminate the directional ambiguity associated with double-exposed images. Present digital cameras typically contain CCD arrays with 1024^2 to 2048^2 pixels. This resolution is still moderate compared to photographic PIV but high-resolution CCD cameras are likely to become available in the near future. In terms of temporal resolution, the maximum achievable repetition rate of both Nd:YAG lasers and cross correlation CCD cameras is in the order of 10–30 Hz which is much slower than the time scales of most flows. Therefore, although PIV is an instantaneous technique, true time-resolved recordings of fast flows such as those investigated in this work are still not feasible.

An important parameter influencing the accuracy of PIV is the size of the recorded particle images in the recording plane. This depends not only on the particle diameter d_p but also on the point response function of the camera lens. In the case of diffraction-limited imaging, the point response function is an Airy function and the image of a finite-diameter particle will form a diffraction pattern with diameter (see e.g. [3])

$$d_s = 2.44(M+1)f^{\#}\lambda \tag{2.9}$$

where $f^{\#} = f/D_a$ is the numerical aperture (f-number) of the camera lens, defined as the ratio between its focal length f and aperture diameter D_a, and λ is the laser light wavelength. Neglecting lens aberrations, an estimate of the total particle image diameter d_t is given by [3]

$$d_t = \sqrt{M^2 d_p^2 + d_s^2} \tag{2.10}$$

It is seen that for small magnifications M which arise when measuring large areas in the flow, the particle image size is mainly governed by the diffraction-limited spot, $d_t \approx d_s$. Furthermore, in order to obtain a sharp image the particle needs to fall within the focal depth δz of the camera lens which may be estimated from [4]

$$\delta z = 4\left(1 + \frac{1}{M}\right)^2 f^{\#2}\lambda \tag{2.11}$$

Raising the numerical aperture $f^{\#}$ leads to an increase of both the particle image diameter and the focal depth, but in turn causes a reduction of the light intensity falling on the CCD. The above implies that PIV measurements require a careful optimization of the parameters d_p, M and $f^{\#}$.

2.2.3 Image processing

In order to extract the displacement information from PIV images, a statistical method is applied. This consists of determining the average linear displacement in each interrogation area IA using cross correlation techniques. The discrete spatial cross-correlation Φ with respect to two images is given as [99]

$$\Phi(k,l) = \sum_{i=1}^{D_I}\sum_{j=1}^{D_I} I_1(i,j) I_2(i+k, j+l) \tag{2.12}$$

where I_1 and I_2 are the light intensities, i.e. 2D gray scale values, extracted from the two images and D_I is the pixel width of the square interrogation area. By applying Eq. (2.12) for different shifts (k,l), a correlation plane is formed which statistically measures the degree of match between the particle images in the two interrogation areas. The peak position in this correlation plane then represents an estimate of the particle displacement.

Computationally, the double summation in Eq. (2.12) is expensive and is more effectively performed in the frequency domain. Advantage is therefore taken of the correlation theorem which states that the cross-correlation of two functions is equivalent to a complex conjugate multiplication of their Fourier transforms $\mathcal{F}$ [99]

$$\Phi(k,l) = \mathcal{F}^{-1}[\mathcal{F}(I_1)\mathcal{F}^*(I_2)] \tag{2.13}$$

where $\mathcal{F}^{-1}$ denotes an inverse Fourier transform and * a complex conjugate. Implementing Eq. (2.13) using FFT algorithms reduces the number of operations to $\mathcal{O}(N^2 log_2 N)$ compared to $\mathcal{O}(N^4)$ operations in the spatial domain. Figure 2.2 shows the general steps of the FFT based velocity vector evaluation procedure. For details on the theory and implementation of DPIV, the reader is referred to Willert and Gharib [127] and Westerweel [122].

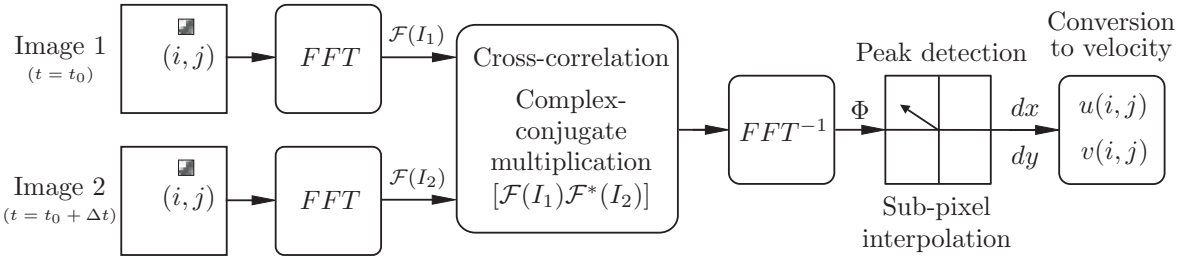

Figure 2.2: *PIV cross-correlation velocity evaluation implemented using Fast Fourier Transforms (after Willert and Gharib [127]).*

As the correlation function only exists for integer shifts, the maximum correlation value only permits the displacement to be determined with an uncertainty of ±0.5 pixel. To increase the accuracy, sub-pixel interpolation schemes are applied which typically estimate the peak location to within ±0.1 pixel. Commonly used interpolation schemes are the Centroid estimator and the Parabolic and Gaussian peak fits, which are all 3-point estimators. The Gaussian estimator generally provides a better approximation of the actual peak shape and is therefore frequently used. Several authors have investigated the effect of peak-finding schemes on the velocity data, see e.g. [122, 117].

Following the vector evaluation procedure, it is common to apply some sort of validation criterion in order to detect and remove spurious vectors that result from poor correlations due to insufficient seeding density or low signal-to-noise ratio *SNR*. A commonly applied detection criteria is the median displacement scheme by Westerweel [123], but a variety of alternative methods to detect these so-called outliers and possibly replace them with vectors interpolated from the surrounding data have been developed, see e.g. Huang et al. [50].

2.3 Measurement uncertainty and resolution

The performance of a PIV experiment may be characterized by the accuracy of the instantaneous velocity estimations, the detection rate and the spatial resolution of the measurements. In this section, the most important aspects influencing these parameters are reviewed, and a set of general design rules for PIV measurements are given.

2.3.1 Measurement errors

The accuracy of PIV depends on both the nature of the flow field, the experimental setup and the interrogation method. Generally, the total measurement error ϵ_t may be separated into a bias error ϵ_{bias} and a random error or measurement uncertainty ϵ_{rms}, i.e. $\epsilon_t = \epsilon_{bias} + \epsilon_{rms}$ [99]. In the literature, Monte Carlo simulations based on synthetic PIV images with known displacements have been frequently used as a tool to quantify the errors, see e.g. [60, 70, 117].

The dominating contribution to the bias error ϵ_{bias} stems from the estimation of the correlation peak location or, more specifically, the estimation of the fractional displacements performed by the sub-pixel interpolation scheme. When the size d_t of

the imaged particle is too small with respect to the pixel size d_r, the 3-point sub-pixel estimators tend to bias the displacements toward integer pixel values due to an under-sampling of the image field. This effect is known as 'pixel locking' and causes an unrecoverable bias error. Several studies, e.g. [70, 125, 117], have shown that this bias error may be reduced by ensuring that the recorded particle images cover at least 1–2 pixels, i.e. $d_t/d_r \sim 1$–2. In fact, the estimation error has a minimum at $d_t/d_r \sim 2$, with a value that is proportional to d_t/D_I [124]. Pixel-locking may also be reduced by using an estimator that more accurately approximates the correlation peak shape. A recent comparative study by Ullum [117] of four commonly used sub-pixel interpolation schemes revealed that relatively low bias errors are associated with the Gaussian estimator and an iterative scheme known as Whittaker's reconstruction, which was first applied to PIV by Lourenco and Krothapalli [70]. In comparison, the Centroid estimator only showed a high accuracy for small d_t/d_r whereas acceptable performance of the Parabolic peak finder was confined to large d_t/d_r [117].

Another type of bias errors stems from distortions of the correlation function itself. This may be induced e.g. by the presence of velocity gradients within the interrogation area *IA* which will result in a broadening of the displacement-correlation peak. As the total volume of the distribution remains constant, a broadening results in a reduction of the peak amplitude and hence a decreased detection probability [124]. Furthermore, the estimated displacement across the interrogation area will be biased towards lower values because particles with large displacements are more likely to move out of the *IA* between the two illuminations. This effect is referred to as in-plane loss-of-pairs. Similarly, three-dimensional motion in the direction perpendicular to the light sheet may also cause particles to leave the interrogation area and result in out-of-plane loss-of-pairs. Both effects set an upper limit on the pulse separation Δt as is also imposed by the fact that PIV is not capable of taking the curvature of the particle trajectory into account, i.e. it recovers only the average linear shift between the two exposures.

Other error sources may include background noise, lens aberrations or electronic noise associated with the digital pixelization of the image. Huang et al. [50] and Forliti et al. [35] provide detailed analyses of errors in cross-correlation DPIV and also suggest procedures to reduce them. Although the general uncertainty trends in different setups are similar, Forliti et al. [35] argue that a detailed quantification of DPIV errors requires an *in situ* calibration against a flow field with known properties.

2.3.2 Resolution limits

When investigating turbulent flows, an essential parameter of the PIV system is its spatial resolution. Because each evaluated velocity vector represents a spatial average over the interrogation area *IA*, the spatial resolution is just the size of the *IA* in the fluid, $d_I = D_I/M$. This length should, ideally, be small relative to the length scales of the flow field. The lower limit of the spatial resolution is ultimately governed by the seeding density and the particle displacement between the two illumination pulses. However, to retain a high accuracy, the pulse separation Δt cannot be made arbitrarily small because the displacement must be larger than the uncertainty in the measurement. This implies that a trade-off between accuracy and resolution is generally necessary in PIV measurements.

To quantify this uncertainty trade-off and fully describe the capabilities of a PIV system, Adrian [4] introduced the related term dynamic spatial range *DSR*. *DSR* is defined as the linear dimension l_x of the field-of-view in the fluid divided by the smallest resolvable spatial variation and is therefore at least

$$DSR = \frac{l_x}{\Delta x_{max}} = \frac{L_x}{M \Delta x_{max}} \tag{2.14}$$

where Δx_{max} is the particle displacement associated with the maximum full-scale velocity $u_{max} = \Delta x_{max}/\Delta t$ and L_x is the format of the recording medium. Essentially, *DSR* corresponds to the number of independent vectors that can be measured across the field-of-view. The simplest means of improving the spatial resolution is to magnify the images, but this is accomplished at the cost of a reduced field-of-view. Furthermore, optimization of *DSR* conflicts with the desire to resolve large velocity differences in the flow field which is expressed in terms of the dynamic range of the measurement. Adrian [4] defined the dynamic velocity range *DVR* as

$$DVR = \frac{u_{max}}{\sigma_u} = \frac{M \Delta x_{max}}{k_t \, d_t} \tag{2.15}$$

where the rms error σ_u defines the minimum resolvable velocity fluctuation and k_t is a constant that depends on the ability of the interrogation algorithm to measure displacements accurately. The lower end of the dynamic range is thus determined by the requirement that the corresponding displacement can be distinguished from the noise floor in the correlation plane. The higher end, in return, is dictated by the restriction that the displacement should not exceed a certain fraction of the IA side length to minimize loss-of-pairs. It follows immediately from equations (2.14) and (2.15) that

$$(DSR)(DVR) = \frac{L_x}{k_t \, d_t} \tag{2.16}$$

Eq. (2.16) states that the capability of a PIV system to have both a large dynamic spatial range and a large dynamic velocity range is determined by a dimensionless constant $L_x/k_t d_t$ that is a characteristic of the system. Eq. (2.16) therefore expresses the necessary trade-off between resolution and accuracy in PIV. Large values of both *DSR* and *DVR* are required for turbulence research, and Adrian [4] therefore estimated the values of the constant $L_x/k_t d_t$ attainable with various types of recording media.

2.3.3 Experimental design rules

As implied above, several factors must be optimized both when acquiring the PIV data and in the subsequent image processing stage in order to ensure desired levels of both accuracy and resolution. In an actual PIV setup, the hardware generally fixes λ, d_r and possibly Δz_0, and tracking characteristics set an upper bound on d_p. Furthermore, the desire to sample a field-of-view with a certain size dictates M. This leaves the parameters C, $f^{\#}$, Δt to be optimized at the recording stage and the IA side length $d_I = D_I/M$ and the sub-pixel estimator, among other parameters, at the processing stage. Based on Monte Carlo simulations, Keane and Adrian [60, 61] formulated the following general design rules to yield optimal performance of the PIV analysis:

- image density: $\mathcal{N}_I = C d_I^2 \Delta z_0 > 10$
- spatial gradients: $M|\Delta\vec{u}|\Delta t/D_I < d_t/D_I \approx 3$–$5\%$
- in-plane motion: $|\Delta X| < \frac{1}{4} D_I$
- out-of-plane motion: $|\Delta z| = |u_z|\Delta t < \frac{1}{4}\Delta z_0$

The first criterion states that the number $\mathcal{N}_I$ of matching particle image pairs within each interrogation area should be at least 10. This is essential for two reasons. First, a high seeding concentration raises the probability of a valid displacement detection and, secondly, it reduces the measurement uncertainty simply because more particle pairs increase the signal-to-noise ratio SNR. A high seeding concentration C is also necessary in order to reduce D_I and thereby enhance the spatial resolution. The second criterion above states that the effect of velocity gradients is insignificant when the velocity variations $|\Delta\vec{u}|$ over the IA are not larger than 3–5% [124]. The third inequality expresses the so-called 'one-quarter' rule that the in-plane image displacement $|\Delta X|$ should not exceed 25% of the IA side length D_I, and the fourth criterion is a similar requirement for the out-of-plane displacement $|\Delta z|$ with respect to the light sheet thickness Δz_0.

To the above design rules should be added the requirement $d_t/d_r \sim 1$–2 in order to avoid pixel-locking effects, as previously discussed. One way of increasing d_t is to slightly defocus the particle image. However, Westerweel [125] has shown that whereas this reduces the bias error it, in return, increases the random error and therefore leaves no real net improvement. Given the experimental restriction $d_t/d_r \sim 1$–2, a better approach is therefore to use equations (2.9) and (2.10) to determine the relation between the image magnification M and the minimum f-number $f^\#$ for a given tracer size d_p and pixel width d_r. This relation is shown graphically in figure 2.3 for particle diameters of 2 μm and 30 μm, respectively, corresponding to the seeding particles used in the present PIV measurements, see Parts B and C of this thesis.

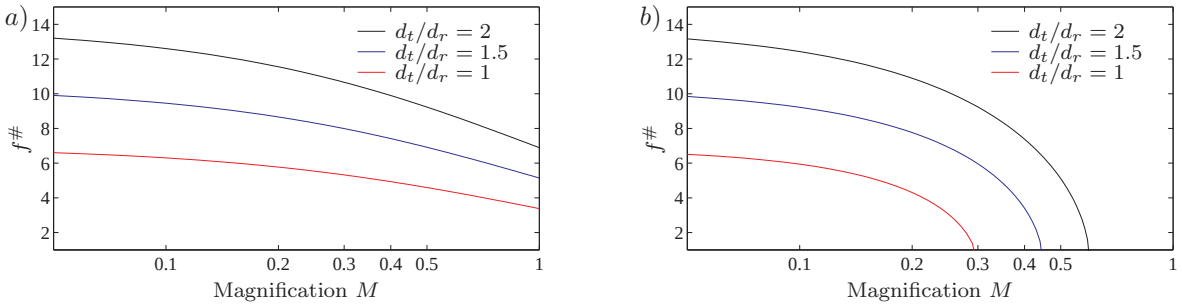

Figure 2.3: *The minimum numerical aperture $f^\#$ of the camera lens as a function of the image magnification M. a) 2 μm diameter particles b) 30 μm diameter particles.*

Summing up, a recommended experimental design procedure consists of the following steps (see also Keane and Adrian [60]). First the tracer size d_p is chosen to ensure good tracking characteristics obeying the guidelines given in section 2.2.1. Then figure 2.3 is consulted to determine $f^\#$ for the desired M. Alternatively, Adrian [4]

provides the following formulas to determine the optimum magnification M_{opt} and f-number $f^{\#}_{opt}$ that will avoid errors, e.g. pixel locking, due to the finite resolution of the recording medium:

$$M_{opt} = \frac{c_r d_r}{(1.5\,\delta z\,\lambda + d_p^2)^{1/2}}\,, \qquad f^{\#}_{opt} = \frac{0.5(\delta z/\lambda)^{1/2}}{1 + 1/M_{opt}} \tag{2.17}$$

where c_r is the optimum particle image pixel width, i.e. $c_r = d_t/d_r = 2$ [124]. Next, based on *a priori* knowledge of the flow field, D_I and Δz_0 is chosen to maintain the desired spatial resolution and restrict out-of-plane motion, respectively. The seeding density C is raised to fulfill $\mathcal{N}_I > 10$ and finally the pulse separation is adjusted to minimize velocity gradients and loss-of-pairs:

$$\Delta t \;<\; \min\left\{ \frac{d_t}{(M|\Delta\vec{u}|}\,, \frac{D_I}{4Mu}\,, \frac{\Delta z_0}{4u_z} \right\} \tag{2.18}$$

Studies suggest that proper setup of the experiment following the above design rules yield instantaneous velocity estimates accurate to within 1% [122]. Generally, the measurement precision is determined by the particle-image diameter d_t/D_I, whereas the measurement reliability is governed by the image density $\mathcal{N}_I$. An interesting observation by Westerweel [124] is that the measurement resolution is determined by d_t/D_I and not by d_r/D_I. This implies that even though photographs offer many more pixels than CCD arrays, the resulting precision is similar as long as d_t/D_I is equal. The reason for this is that an increase in the resolution of the recording medium will not add more information, at least not when $d_t/d_r > 1$, but merely distribute it over more samples, i.e. over-sample the data [124, 4]. Photographs are still superior in the respect, however, that they can view a larger area of the flow field because of their larger format L_x.

2.3.4 Optimization of PIV evaluation

The above guidelines pertain to standard cross-correlation PIV analysis. In the last few years, substantial effort has been devoted to the development of new interrogation algorithms that improve the accuracy and/or spatial resolution. Based on the bounds stated in the previous section, Keane et al. [62] found that the relative uncertainty in the measured velocity $|\delta(\vec{u})|$ satisfies

$$|\delta(\vec{u})| > 2k_t \left(\frac{|\nabla\vec{u}|}{M} d_t \right)^{1/2} \tag{2.19}$$

where $|\nabla\vec{u}|$ is the spatial rate of change of the velocity field. Eq. (2.19) shows that the error may be reduced by increasing the magnification M, decreasing the particle image diameter d_t, or decreasing the error in locating the correlation peak as specified by k_t.

Westerweel et al. [126] demonstrated that the measurement uncertainty ϵ_{rms} scales proportional to the displacement when $|\Delta X| < 0.5$ pixel whereas it attains a higher constant value at larger displacements. One way of reducing the error k_t is therefore to ensure that $|\Delta X|$ does not exceed 0.5 pixel by offsetting the interrogation area in the second image with respect to the first *IA*, with an amount that equals the

mean displacement vector. This also reduces the number of in-plane loss-of-pairs and therefore raises the correlation peak detectability. The window offset technique may be applied globally in flows that have a distinct mean flow velocity by offsetting the second *IA* with an integer pixel displacement that corresponds to the convection velocity.

In more complex flows, a local method referred to as adaptive correlation or multiple pass interrogation is more suitable, see Scarano and Riethmuller [105] and Ullum [117]. Multiple pass interrogation is an iterative procedure in which the *IA* is offset according to the *local* integer displacement found from an initial pass with no offset. The procedure is usually repeated until the integer offset vectors converge to $\pm$ 1 pixel which typically requires three passes [99]. A significant advantage of the multiple pass interrogation procedure is that it may be implemented in a hierarchical multi-grid approach where both the sampling grid and the *IA* side length D_I is simultaneously refined in the process. This is feasible because the one-quarter rule no longer applies and the procedure thus effectively de-couples accuracy and spatial resolution leading to a significant increase in the dynamic velocity range.

Keane et al. [62] suggested that to enhance the spatial resolution of the measurement even further, the initial statistical velocity evaluation can be followed by a subsequent particle tracking. This two-step procedure is referred to as super-resolution PIV and relies on a high seeding density. Several other improvements of the digital PIV evaluation are suggested in the vast amount of papers on PIV processing algorithms that appears on a continuous basis, see e.g. Hart [44]. Parallel to this, a rapid development in methods to extract the out-of-plane velocity component is evident. This extension of the traditional PIV technique is referred to as stereoscopic PIV and is already commercially available. Prasad [98] provides a review of the principles and current trends of stereoscopic PIV.

2.4 PIV post-processing

Given a PIV velocity vector field measured on a two-dimensional equidistant Cartesian grid, different fluid mechanical quantities may be estimated from the data. For instance, in the study of coherent flow structures the vorticity is a convenient measure of the rotation of fluid elements in the flow. This section briefly describes methods to derive the vorticity from planar PIV data. Furthermore, it gives estimates of the statistical uncertainties associated with calculation of flow statistics from a large number of instantaneous PIV velocity fields.

2.4.1 Vorticity estimation

For a three-dimensional velocity field $\vec{u} = (u, v, w)$, the vorticity vector $\vec{\Omega}$ is defined as the curl of $\vec{u}$

$$\vec{\Omega} = \nabla \times \vec{u} = \left(\frac{\partial w}{\partial y} - \frac{\partial v}{\partial z}\right)\vec{i}_x + \left(\frac{\partial u}{\partial z} - \frac{\partial w}{\partial x}\right)\vec{i}_y + \left(\frac{\partial v}{\partial x} - \frac{\partial u}{\partial y}\right)\vec{i}_z \tag{2.20}$$

As PIV generally only provides the planar u and v components, it only allows the determination of the out-of-plane vorticity component Ω_z, i.e. the projection on the

normal to the data plane

$$\Omega_z = \left(\frac{\partial v}{\partial x} - \frac{\partial u}{\partial y} \right) \tag{2.21}$$

Because of the discrete nature of the data, finite differencing has to be employed in the estimation of the spatial derivatives. A method for evaluating vorticity which is frequently used e.g. in commercial PIV software, is the second order accurate central difference scheme

$$\Omega_z(i,j) \approx \frac{v_{i+1,j} - v_{i-1,j}}{2\Delta x} - \frac{u_{i,j+1} - u_{i,j-1}}{2\Delta y} \tag{2.22}$$

The numerical differentiation introduces a truncation error and it is also known to be very sensitive to noise, i.e. the measurement uncertainty ϵ_{rms}, in the velocity data. To demonstrate how the error ϵ_Ω in the vorticity estimation depends on these two error sources, Eq. (2.22) may be rewritten as

$$\Omega_z(i,j) = \left(\frac{v_{i+1,j} - v_{i-1,j}}{2\Delta x} + \Delta x^2 \mathcal{R} + \frac{\epsilon_{rms}}{\Delta x} \right) - \left(\frac{u_{i,j+1} - u_{i,j-1}}{2\Delta y} + \Delta y^2 \mathcal{R} + \frac{\epsilon_{rms}}{\Delta y} \right) \tag{2.23}$$

where $\mathcal{R}$ stands for higher order terms. Eq. (2.23) shows that the present finite difference truncation error is of order $(\Delta x^2, \Delta y^2)$ and hence decreases rapidly when reducing the grid spacing, whereas the error associated with the measurement uncertainty scales inversely proportional to $(\Delta x, \Delta y)$. As pointed out by Lourenco and Krothapalli [70] this suggests that for a given velocity error, an optimum grid spacing exists for which the error in the vorticity estimate is minimized. In practice, however, the random error ϵ_{rms} usually dominates because small grid spacings are necessary in order to bring out small-scale features in the flow. This may lead to noisy vorticity estimates, especially in cases where neighboring velocity data are correlated due to the common practice of overlapping adjacent interrogation areas. Raffel et al. [99] suggest other extended 1D differential operators, e.g. a least-squares approach, that reduces this random error.

A true two-dimensional vorticity evaluation scheme is the circulation method. It is based on Stokes' theorem which states that the circulation Γ is related to the vorticity by $\Gamma = \oint_C \vec{u} \cdot \mathrm{d}\vec{l} = \int \vec{\Omega} \cdot \hat{n} \, \mathrm{d}S$ where $\vec{l}$ describes the closed contour path C around the surface S, and $\hat{n}$ the unit vector normal to S [99]. The out-of-plane vorticity at a point may therefore be obtained by calculating Γ around a small contour and divide by the enclosed area [122]

$$\Omega_z = \lim_{S \to 0} \oint_C \frac{\vec{u} \cdot \mathrm{d}\vec{l}}{S} \tag{2.24}$$

Choosing C as the rectangular contour formed by connecting the neighboring 8 points and using the trapezoidal rule for integration gives Ω_z at the grid point (i,j) as [99]

$$\begin{aligned} \Omega_z(i,j) \approx \frac{1}{4\Delta x \Delta y} \Big[& \frac{\Delta x}{2}(u_{i-1,j-1} + 2u_{i,j-1} + u_{i+1,j-1}) \\ & + \frac{\Delta y}{2}(v_{i+1,j-1} + 2v_{i+1,j} + v_{i+1,j+1}) \\ & - \frac{\Delta x}{2}(u_{i+1,j+1} + 2u_{i,j+1} + u_{i-1,j+1}) \\ & - \frac{\Delta y}{2}(v_{i-1,j+1} + 2v_{i-1,j} + v_{i-1,j-1}) \Big] \end{aligned} \tag{2.25}$$

A crude conservative estimate of the accuracy attainable with the vorticity estimators in equations (2.22) and (2.25) is 10–20%, or one order of magnitude larger than the noise level in the PIV velocity data. However, the use of appropriate smoothing algorithms, e.g. 3×3 Gaussian filters, prior to the derivative calculation may improve this considerably, as shown in a detailed study by Luff et al. [71]. An adaptive vorticity scheme has also been proposed by Lourenco and Krothapalli [70].

2.4.2 Flow statistics

Flow statistics may be calculated from PIV data by ensemble averaging a large number of instantaneous velocity fields collected independently in a stochastically stationary flow. This yields estimates of turbulent properties at each grid point (i, j) in the measurement plane and thus enables comparisons with mean data stemming from e.g. LDV measurements or CFD simulations based on RANS turbulence models. For example, if N denotes the total number of vector maps in an ensemble, estimates of the ensemble average and standard deviation of the u-component of the velocity are calculated from

$$\langle u(i,j)\rangle = \frac{1}{N}\sum_{n=1}^{N} u(i,j,n) \quad \text{and} \quad s_u(i,j) = \sqrt{\frac{1}{N}\sum_{n=1}^{N}\left[u(i,j,n) - \langle u(i,j)\rangle\right]^2}, \tag{2.26}$$

respectively, and similarly for the v-component. Based on standard error estimates, which have been shown to apply to ensemble averaged PIV data by Ullum et al. [119], the uncertainty in the mean velocity and standard deviation estimated from N statistically uncorrelated samples can be written as

$$\epsilon_\mu = z_c \, \frac{s_u}{\sqrt{N}} \quad \text{and} \quad \epsilon_s = z_c \, \frac{s_u}{\sqrt{2N}}\,, \tag{2.27}$$

respectively, where z_c is the confidence factor which is equal to 1.96 for a 95% confidence interval, see e.g. Wernet [121]. Having established the accuracy of the instantaneous PIV velocity fields to about 1%, equation (2.27) shows how the statistical errors drop quite rapidly by raising the number of samples.

2.5 Summary

This chapter provided a general introduction to Particle Image Velocimetry with the focus on digital cross-correlation PIV which is the technique used in the present work. Important parameters that should be observed and optimized in each of the four individual steps of the PIV technique were described, and guidelines for estimating the tracking characteristics of seeding particles and a set of general experimental design rules introduced. Attention was also devoted to a discussion of the factors that determine the measurement uncertainty and limit the attainable dynamic ranges of velocity and spatial resolution. As PIV is a rapidly evolving technique, a brief discussion of the current trends and improvements of the digital interrogation procedure was also included. Finally, the subject of post-processing of PIV data was touched upon, including an algorithm for calculating the out-of-plane component of the vorticity vector. The experimental guidelines introduced in this chapter provide the basis for the setup of the PIV measurements that will be presented in Parts B and C of this dissertation.

Part B

Square cylinder

Chapter 3

Flow past a square cylinder

In order to demonstrate the feasibility of the PIV technique as a tool to provide reliable turbulence measurements in a topologically complex unsteady flow, a large number of conditionally sampled PIV vector maps were acquired in the near wake region of two-dimensional flow past a stationary square cylinder. This chapter describes the experimental setup and acquisition procedures and presents sample instantaneous and ensemble averaged PIV results. As this type of flow is well-described in the literature, the current aim is not to perform a detailed study of the flow physics, but rather to demonstrate the main features of the flow and the quality of the PIV data. Besides showing the capabilities of the PIV technique, the main objective is to provide instantaneous planar data that enables an experimental *a priori* test of various subgrid-scale models used in LES. This test will be presented in the next chapter.

3.1 Introduction

The unsteady flow past a cylinder of square cross-section is a convenient test case for both experimental and computational studies because even though the geometry is simple, the physics of the flow is very complex, involving phenomena like unsteady separation, streamline curvature, recirculation and large-scale turbulent coherent structures. Traditionally, most work on flow past bluff bodies has focused on the circular cylinder, but in recent years the flow around rectangular cylinders has received a great deal of attention, mainly as a result of increasing computer capabilities and the need to test new turbulence models, see e.g. Rodi et al. [102] for an overview.

In the general case of a rectangular cylinder with side length D and height H exposed to a uniform cross flow with bulk velocity U_∞, the flow physics depends on the Reynolds number $Re_D = U_\infty D/\nu$ and on the side ratio D/H. At extremely low Reynolds numbers, the flow separates at the trailing edges rather than at the leading edges where the separation is indiscernible owing to immediate reattachment [88]. As Re_D is increased, a pair of steady symmetric vortices forms behind the body. Above a critical Reynolds number around 50 [109], this twin-vortex arrangement becomes unstable, and vortices are shed alternately from the upper and lower side of the cylinder. This gives rise to an oscillating antisymmetric wake flow pattern referred to as a von Kármán vortex street. Contrary to the case of the circular cylinder, the separation points remain fixed at the leading edges of the rectangular cylinder and a flapping

shear layer develops on the sides. The vortex shedding is characterized by a constant dimensionless shedding frequency, the Strouhal-number $St = f_s D/U_\infty$, where f_s is the dominating wake frequency. At about $Re_D = 200$, the flow undergoes transition and turbulence effects become more and more pronounced. Sohankar [109] performed an extensive numerical study of the flow past square cylinders at low to moderate Reynolds numbers, $Re_D = 45$–500, and described the transition scenario in detail.

The present study focuses on the fully turbulent regime with $Re_D = 4000$ and $H/D = 1$. In a broad range of Reynolds numbers roughly spanning 10^3–10^5, global quantities of the flow such as the Strouhal number, mean drag, base pressure and RMS drag and lift forces have been shown to vary only little with Re_D [88, 109]. Experimental investigations relevant for this study therefore include detailed LDV measurements performed by Durao et al. [30] at $Re_D = 1.4{\cdot}10^4$ and by Lyn et al. [72] at $Re_D = 2.2{\cdot}10^4$. The latter investigation included phase-averaged velocity statistics of the near wake of a square cylinder and discussed the flow structure and its topology in detail. Recently, Nakagawa et al. [87] also obtained LDV data at $Re_D = 3000$, close to the present value.

The flow past a square cylinder has also proved to be an excellent test case for comparative turbulence model studies. This is substantiated in the organization of a number of workshops such as the "Workshop on Large Eddy Simulation of Flows past Bluff Bodies", see Rodi et al. [102], that has used the configuration of Lyn et al. [72] as reference. Whereas statistical RANS turbulence models have revealed difficulties in predicting the complex unsteady phenomena, the LES simulations show a better agreement with experimental data [102]. However, the numerical research to date has seemed to focus on mean fields, despite of the time-dependent nature of the data.

Although the vortices are predominantly two-dimensional, Murakami and Mochida [85] have shown that a 2D approach is insufficient from a numerical point of view. They compared 2D and 3D LES computations and found that the 2D simulation did not accurately reproduce the fluctuating lift and drag forces. This was attributed to the fact that vortex stretching and other energy transfer mechanisms important for the energy cascade are essentially three-dimensional phenomena [114]. Furthermore, experimental studies have shown that large-scale 3D structures exist which may lead to a modulation of the shedding frequency. For instance, Wu et al. [128] found evidence of longitudinal vortices that are inclined to and superimposed on the Kármán vortices. Nevertheless, 3D effects are not investigated in the present work.

3.2 Experimental setup

Figure 3.1 shows a schematic of the experimental setup. The PIV measurements were performed in a 300 mm wide and 600 mm high wind tunnel test section that allowed optical access through glass walls on three sides. A cylinder of square cross-section with side length $D = 40$ mm was mounted in the vertical midplane of the test section, 400 mm downstream of the inlet contraction. The cylinder spanned the entire height of the wind tunnel and its sides were aligned with the inlet flow direction (x) and the normal direction (y). The experiments were conducted at a uniform bulk velocity U_∞ of 1.5 m/s, corresponding to $Re_D = 4000$. The upstream inlet flow had a turbulent intensity below 1%.

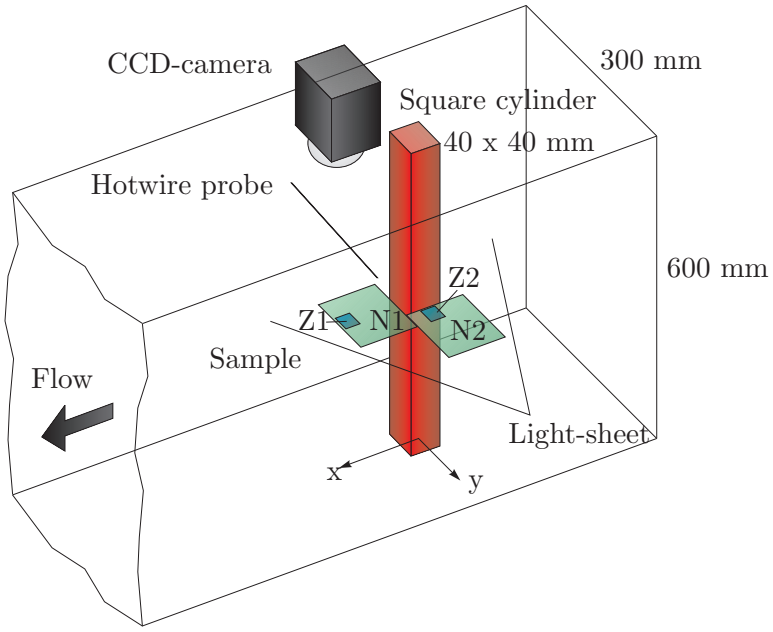

Figure 3.1: *Schematic of the experimental setup. N1 and N2 denote sample areas of size 66×66 mm^2, and Z1 and Z2 sample areas of size 9×9 mm^2. In chapter 4, reference will further be made to N3, which denotes a sample area that is displaced 20 mm in the x-direction with respect to N1.*

To obtain PIV velocity data, the wind tunnel was seeded with 2–4 μm mean diameter glycerol droplets that were generated using a Laskin type seeding generator. According to Eq. (2.6) of section 2.2.1 this particle diameter and the density ratio of $R = 10^3$ lead to a cut-off frequency f_c of roughly $5 \cdot 10^3$ Hz which is fully sufficient for the present purposes. The light source of the PIV system was a Continuum Surelite I-10 double-cavity Nd:YAG laser with an output of 200 mJ per pulse and a pulse duration of 4–6 ns. An articulated light-guiding arm directed the pulsing laser beams to the test section where cylindrical optics produced a plane light sheet. The light sheet was positioned in the horizontal (x, y) mid-plane of the wind tunnel and had an approximate thickness of 1.5 mm. PIV images were captured by a 1k × 1k Kodak Megaplus ES1.0 cross-correlation CCD camera that was equipped with a 60 mm Nikon Micro Nikkor lens and placed at right angles to the laser sheet. The image sets were processed into velocity vector maps by a Dantec FlowMap PIV 2000 Processor using the cross-correlation method. This use of dedicated hardware resulted in fast processing times but also restricted the choice of sub-pixel interpolation scheme to the parabolic peak finder, which is stable but generally more prone to pixel-locking effects, as previously discussed in section 2.3.1.

To bring out different characteristics of the periodic flow, the PIV data were conditionally sampled at 4 phases of the vortex shedding cycle. This was accomplished by triggering the acquisition of PIV images with the signal from a hot-wire probe located outside the separated shear layer, 15 mm to one side of the cylinder, see figure 3.1. This position was selected as it provided a stable sinusoidal signal with large amplitude, yet did not disturb the sampled flow field. The shedding frequency was $f_s = 5 \pm 0.1$ Hz which corresponds to a Strouhal number of $St = 0.133 \pm 0.003$. This value is in agree-

ment with previous investigations [19, 72, 30, 87, 102] and with a survey by Okajima [88] that reported $St \approx 0.13$ for the range of Reynolds numbers between 10^2 and $2 \cdot 10^4$.

Figure 3.1 illustrates the locations and sizes of the four different sample areas that were measured. The field-of-views denoted N1 and N2 were located at the rear and side faces of the cylinder, respectively, and sampled areas of size 66×66 mm^2. This corresponds to a magnification factor M of 0.136 and will be referred to as normal mode. In order to resolve finer structures, zoom optics were used to measure two 9×9 mm^2 areas denoted Z1 and Z2. Z1 was centered in the wake 75 mm downstream of the rear face of the cylinder and Z2 was located within the recirculation zone on the side of the cylinder, see figure 3.1. The field-of-views Z1 and Z2 were recorded at $M = 1.00$ and will be referred to as zoom mode. The time Δt between the two laser pulses was optimized according to the design rules given in section 2.3.3, yielding values of 250 μs and 55 μs in normal and zoom modes, respectively.

Each velocity vector was determined from an interrogation area IA of 32×32 pixels, corresponding to $d_{I,N} \approx 2.2$ mm and $d_{I,Z} \approx 0.32$ mm in normal and zoom mode, respectively. The interrogation areas were overlapped 50% yielding 60×60 vectors per vector map with a distance of $\delta_N = 1.1$ mm and $\delta_Z = 0.16$ mm between vectors. In each field-of-view, sample sizes of 1000 vector maps in each of four phases were collected. Based on turbulence intensities of ∼30%, this lead to an accuracy of 3% on the mean, comparable to the uncertainty of the wind tunnel bulk velocity, and 2% on fluctuating components of velocity, stated according to Eq. (2.27) at confidence levels of 95%. The acquisition time of 1000 conditionally sampled image pairs was of the order of 2 hours.

3.3 Results

This section presents a selection of ensemble-averaged and instantaneous PIV data acquired in field-of-views N1, N2 and Z2, respectively. Reference will be made to phases 1–4 which denote the four different phases of the shedding cycle, equidistantly spaced in time, that were conditionally sampled. Specifically, phase 1 is defined as the instant in time t_1 where the amplitude of the low-pass filtered hot-wire signal exceeds a certain threshold value. Based on t_1 and the mean shedding period $T_s = 1/f_s$ of 200 ms, phase k is then given as $t_k = t_1 + k\,T_s/4$ where $k = 2$–4.

3.3.1 Field-of-view N1

Figure 3.2 shows the ensemble averaged flow field measured in field-of-view N1 which is located in the near wake region immediately behind the cylinder, centered around $(x, y) = (53, 0)$. The free stream flow direction is from left to right and the first column of velocity vectors is situated about 2 mm downstream of the rear side of the cylinder. Origo of the measurement coordinate system is placed at the centerline of the square cylinder such that its corners are situated at $(x, y) = (\pm 20, \pm 20)$ mm.

The left column of figure 3.2 presents ensemble averaged velocity fields $\langle \vec{u} \rangle$ based on 1000 instantaneous PIV realizations in each phase, and the right column shows the corresponding sectional streamlines in order to highlight the details of the shedding motion. The sectional streamlines were obtained by integrating the velocity field to give the spatial distribution of the stream function $\psi = \psi_0 + \int (u dy - v dx)$. The integration

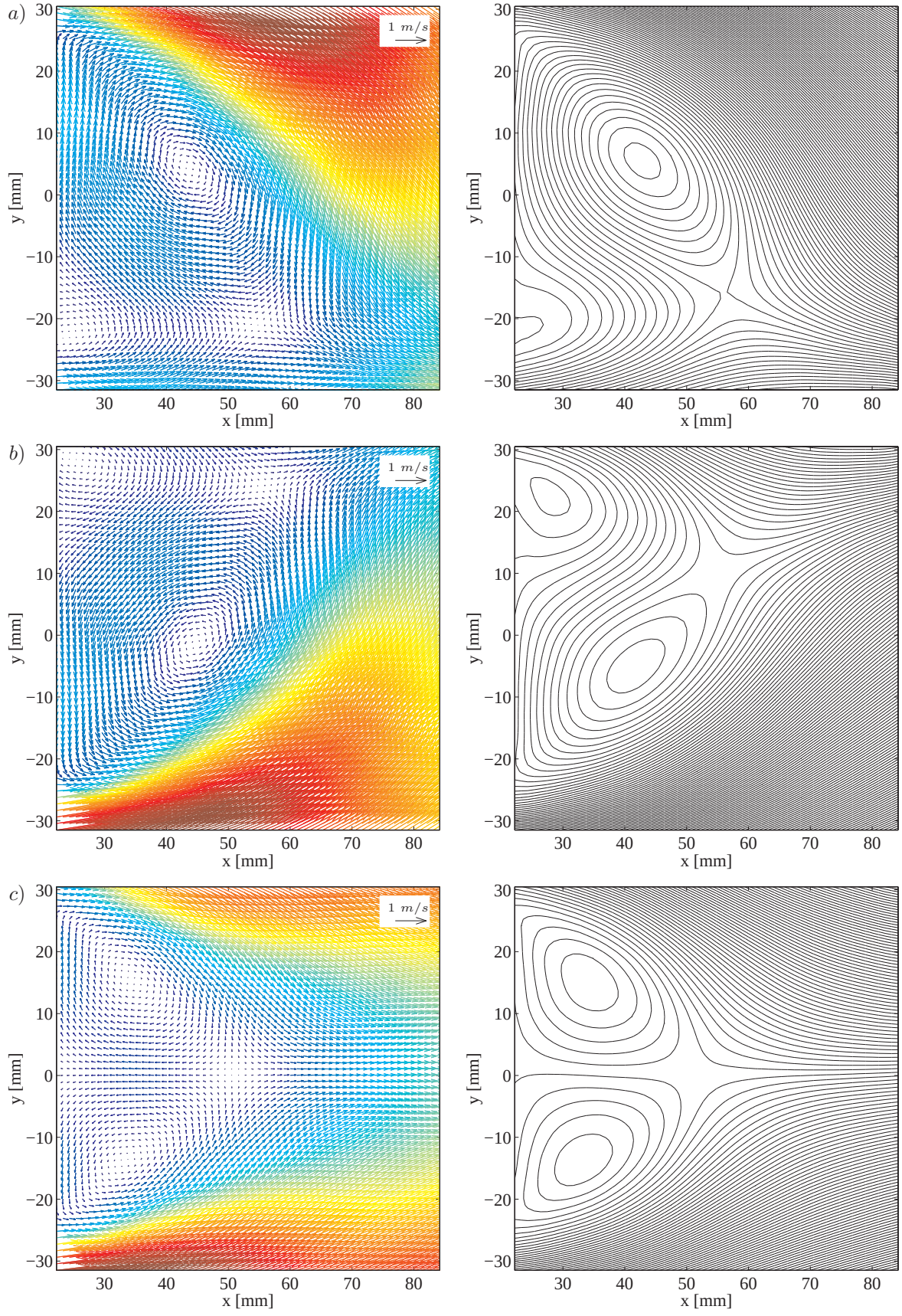

Figure 3.2: *Vector maps of the ensemble averaged velocity field based on 1000 instantaneous samples (left) and corresponding sectional streamlines (right). a) Phase 1 b) Phase 3 c) Mean of all phases 1–4. Field-of-view N1.*

between two neighboring points was done by means of a trapezoidal approximation and the iterative procedure was initiated by specifying an arbitrary value of $\psi_0 = 0$ at a starting point that was located in the center of the velocity field to minimize the accumulation of integral errors. Furthermore, following the scheme proposed by Imaichi and Ohmi [54], the stream function was calculated using two different integration routes along the x- and y-directions, respectively, and ψ at each mesh point then obtained as the arithmetical average of these two values.

Figure 3.2a shows the PIV data obtained in phase 1. Both the vector map and the sectional streamlines give clear evidence of the shedding motion. A large clockwise rotating vortex previously shed from the upper side of the cylinder extends over most of the field-of-view, and a small counter-rotating vortex is about to emerge from the lower cylinder side ($y = -20$ mm). The vector map is color-coded according to the local speed and reveals large differences between velocity magnitudes in the recirculation zone and in the free stream. The streamline plot in figure 3.2a shows both a streamline center, located at $(x, y) \approx (42, 5)$, and a saddle point at $(x, y) \approx (55, -15)$. As discussed extensively by Lyn et al. [72], these two critical points are intimately related to turbulence and its production. This issue will be explored later when observing the out-of-plane vorticity component and Reynolds stresses of the flow.

Figure 3.2b gives the results of phase 3 which is displaced half a shedding period from phase 1. Consequently, the flow topology is mirrored around the centerline $y = 0$, but is otherwise similar to that of figure 3.2a. This fact confirms the validity of the current conditional sampling procedure and the stability of the shedding process. As a result, the average of all acquired phases 1–4 given in figure 3.2c shows a perfectly symmetrical time-mean flow field. The mean field is characterized by two counter-rotating, equally large vortices that form a significant recirculation zone. Figure 3.2c thus corresponds to the mean field obtainable with steady approaches such as hot-wire anemometry, LDV and RANS-based turbulence models.

Figure 3.3 shows the distribution of the time-mean streamwise velocity component $\overline{U}$ along the centerline behind the cylinder. It compares the present PIV results ($Re_D = 4000$) with the LDV measurements of Lyn et al. [72] and previous 3D numerical simulations performed by the author [19] using the commercial CFD code Star-CD, all at $Re_D = 2.2 \cdot 10^4$. Despite the difference in Reynolds numbers, the comparison is feasible because within the turbulent regime the aerodynamic characteristics are relatively insensitive to Reynolds number [88], as already discussed.

Some discrepancies in the predicted velocity recovery in the wake are evident from figure 3.3. However, when comparing the length L_r of the time-mean recirculation zone behind the cylinder, the PIV, LDV and LES results agree within 8% with values of L_r/D of 1.33, 1.38 and 1.28, respectively. Only the steady simulation using the $k - \epsilon$ turbulence model, which is generally known to perform poorly in separated flow regions, predicts a significantly too long recirculation zone ($L_r/D = 1.58$) as was also observed by Rodi et al. [102]. Focusing on the recirculation zone itself, it is interesting to note that the two unsteady techniques, the present PIV and the LES which is based on a Smagorinsky model, agree well on the location and magnitude of the negative velocity peak at $x/D \approx 0.9$. The LDV profile does not resolve this velocity peak, because experimental restrictions prevented Lyn et al. [72] from obtaining data any closer than 10 millimeters from the cylinder side.

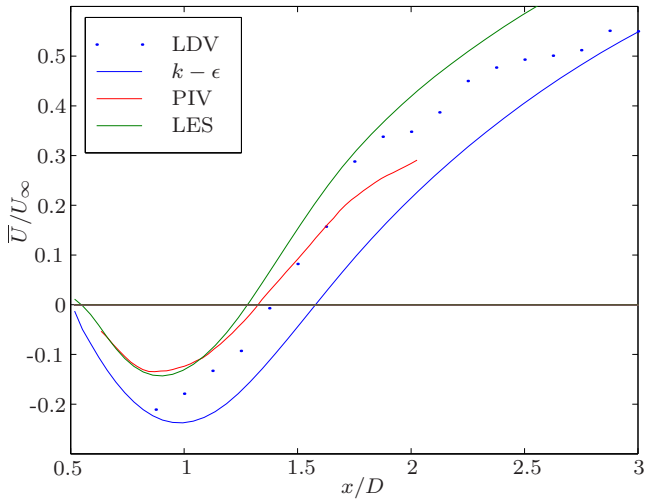

Figure 3.3: *Mean streamwise velocity $\overline{U}/U_\infty$ along the centerline $y = 0$ behind the square cylinder. Present PIV results obtained at $Re_D = 4000$ are compared with LDV data [72] and numerical 3D simulations [19] obtained at $Re_D = 2.2 \cdot 10^4$.*

In order to give an impression of the instantaneous flow structures, figure 3.4 shows PIV snapshots acquired in phase 1 and 3, respectively, together with the corresponding velocity fields after the phase average has been subtracted. Turbulent motion over a wide range of length scales is visible and figure 3.4 thus expresses the additional information on the spatial structures of the flow that is readily attainable with PIV. A similar reasoning applies to figure 3.5 which shows the magnitude of the out-of-plane vorticity component, $|\Omega_z|$, estimated from the data using the circulation method, Eq. (2.25). The instantaneous sample in figure 3.5a reveals intermittent regions of positive and negative vorticity that are not deducible from the ensemble average of phase 3 given in part b of the figure.

Figure 3.6a–c shows contour plots of the Reynolds normal and shear stresses calculated from the ensemble of 1000 realizations in phase 3. The spatial distributions of the three stress components differ significantly from each other as a result of the anisotropy of the flow. Comparison with the streamline plot in figure 3.2b reveals that both the peak of the dominating normal stress $\langle vv \rangle$ and that of the vorticity distribution shown in figure 3.5b coincide with the location of the streamline center. This is in agreement with previous findings [72, 87] and also with a model of the plane turbulent near wake that was introduced, among others, by Hussain and Hayakawa [53]. According to this model, turbulence is produced by vortex stretching in the streamline saddle region, resulting in high Reynolds shear stresses $\langle -uv \rangle$ there, and is then convected towards the streamline center which consequently is associated with high values of turbulent kinetic energy (which in the present case is dictated by $\langle vv \rangle$). The speculated correlation between streamline saddles and regions of high $\langle -uv \rangle$ is also supported by figure 3.6c, although high values are also observed away from the streamline saddle. Figure 3.6d, finally, shows $\overline{\langle vv \rangle}$ based on all phases and again demonstrates the symmetry of the time-mean flow.

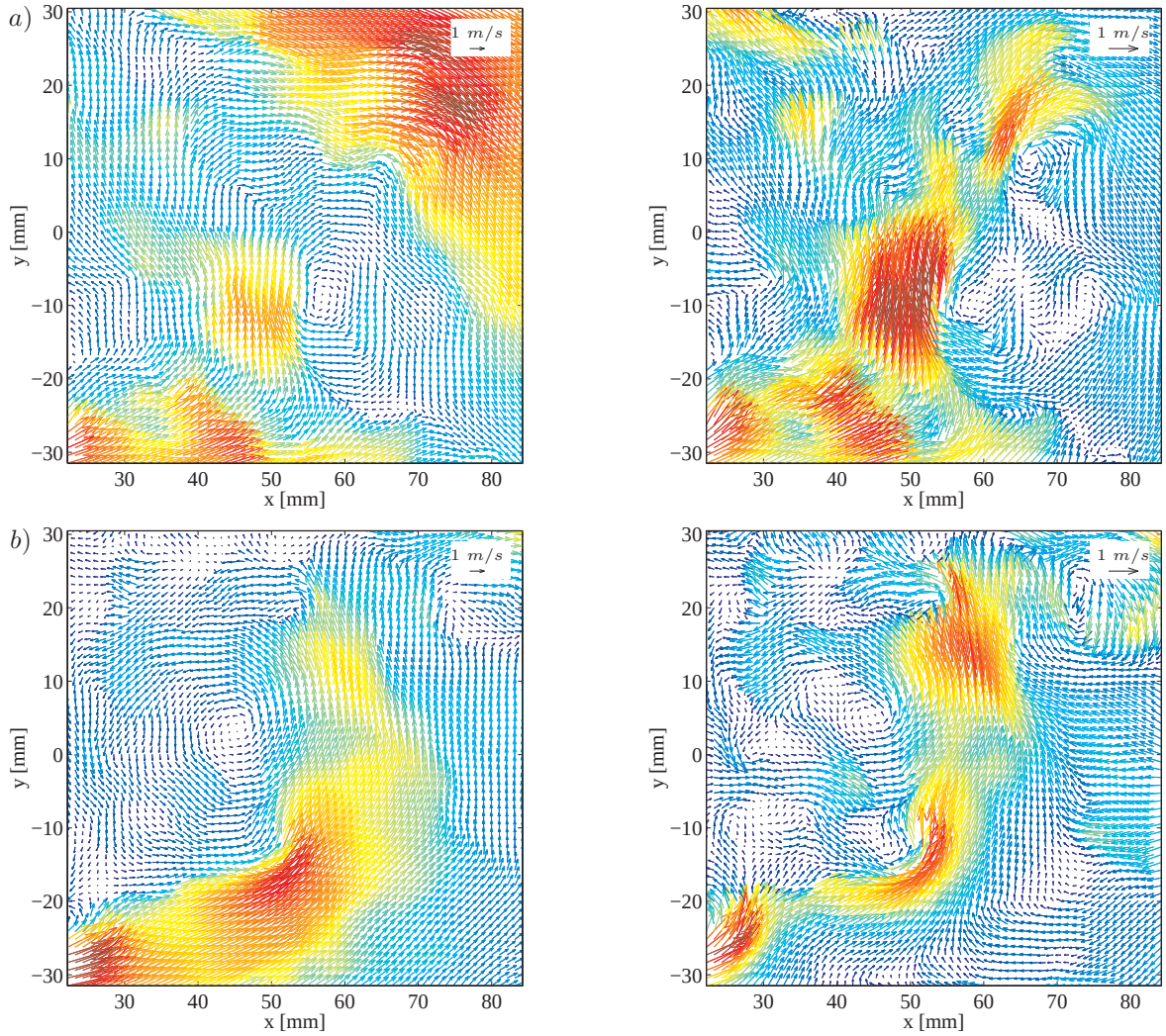

Figure 3.4: *Sample instantaneous velocity vector maps (left) and the corresponding instantaneous deviation $\vec{U}-\langle\vec{U}\rangle$ (right) from the ensemble averages shown in figure 3.2. Color-coding according to the local speed. a) Phase 1 b) Phase 3. Field-of-view N1.*

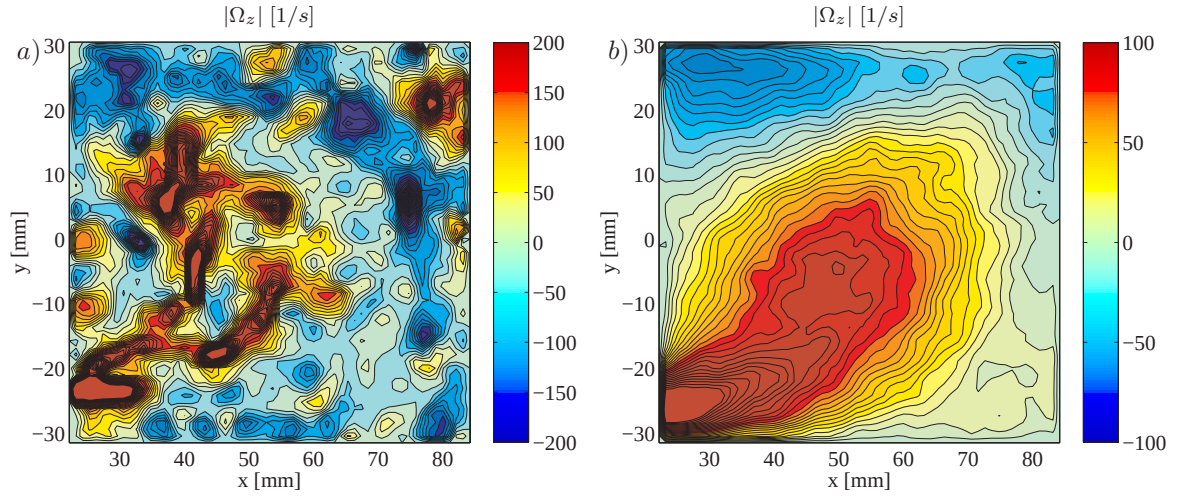

Figure 3.5: *Out-of-plane vorticity component $|\Omega_z|$. a) Instantaneous sample acquired in phase 3 b) Ensemble average of phase 3. Field-of-view N1.*

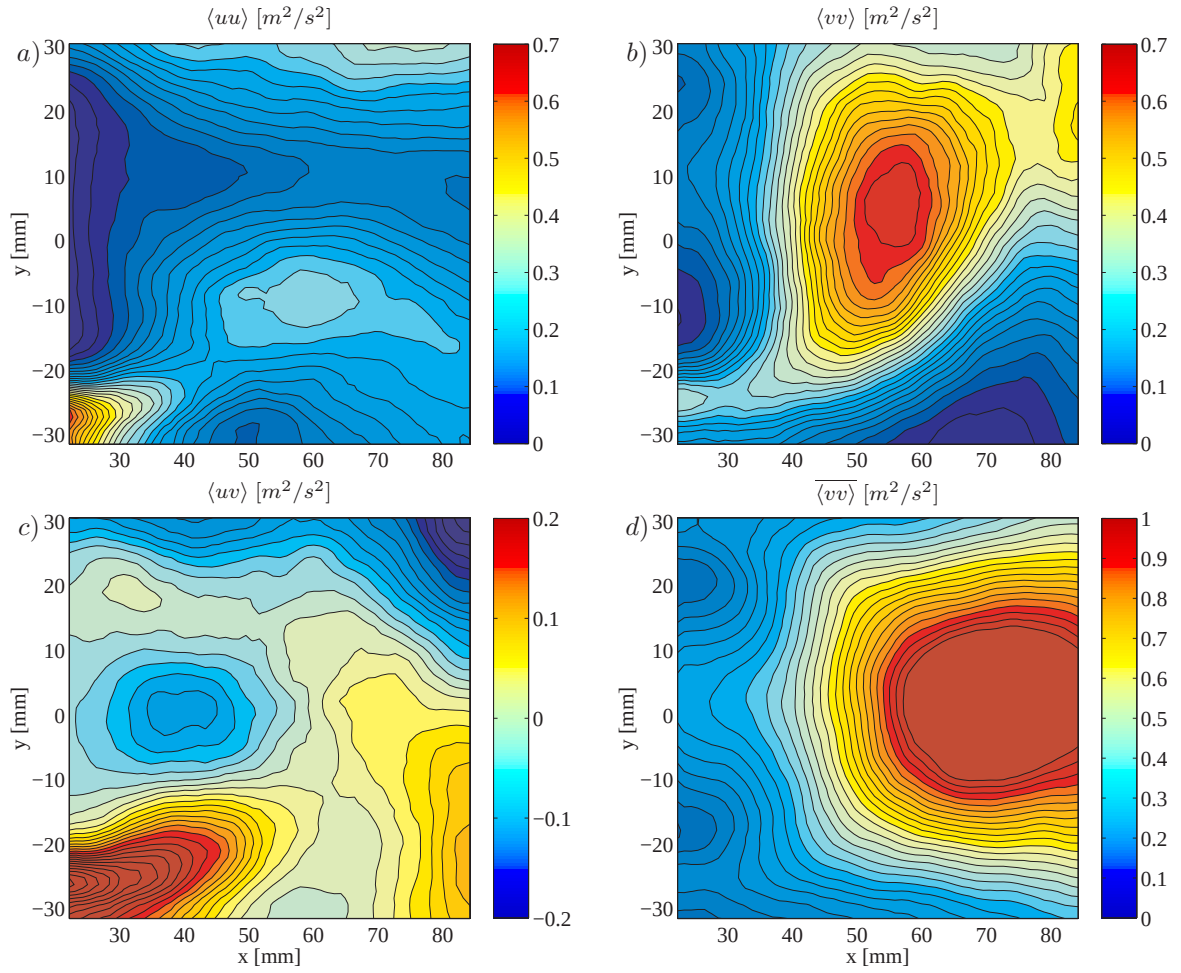

Figure 3.6: *Reynolds normal and shear stresses. a) $\langle uu \rangle$ of phase 3 b) $\langle vv \rangle$ of phase 3 c) $\langle uv \rangle$ of phase 3 d) $\overline{\langle vv \rangle}$ based on all phases 1–4. Field-of-view N1.*

When analyzing the flow topology of the vortex street, an interesting parameter is the convection velocity U_c of the vortices. Nakagawa et al. [87], for instance, determined U_c/U_∞ to lie in the range 0.7–0.85 by detecting the streamwise velocity of the movement of the vorticity peaks. Based on U_c, the streamwise separation of successive vortices, L_u, may be obtained as $L_u = U_c/f_s$. Since the shape of the shed vortex is almost circular, L_u is also a reasonable indication of the vortex length scale in normal direction. In the present work, however, a determination of U_c is hampered by the relatively small field-of-view and the fact that only four phases are resolved. It is expected, though, that the value of $L_u/D \approx 6$ that was reported by both Nakagawa et al. [87] and Lyn et al. [72] also applies in the current case.

One measure of the eddy sizes in the flow is the Taylor length scale λ. For anisotropy, four different spatial Taylor scales may be estimated from the data from single-point ensemble averages, see Ullum et al. [118]. Such data processing was not carried out, but nevertheless anisotropic Taylor scales, along with isotropic Kolmogorov scales, remain convenient measures of the flow. Using the expressions given by Tennekes and Lumley [114], an estimate of the Kolmogorov scale is $\eta = (\nu^3/\epsilon)^{1/4} \sim 0.2$ mm where the dissipation rate, $\epsilon \approx u_{rms}^3/l_i$, was estimated from the RMS-velocities of the flow assuming an integral scale of $l_i = D$. These crude approximations lead to a Taylor scale of $\lambda \sim 4$ mm and a microscale Reynolds number of $Re_\lambda \sim 200$.

Based on the mainly qualitative assessment of both phase averaged and time-mean data performed in this section, it is concluded that the PIV results agree well with both previous experimental data [72, 30, 87] and LES results [102, 19].

3.3.2 Field-of-view N2

This section presents selected results acquired in field-of-view N2 located at the upper side of the cylinder. The attention is directed towards the temporal and spatial variations of the shear layer and recirculation zone in the immediate vicinity of the cylinder side and, consequently, the portion of N2 (see figure 3.1) that measures the free stream flow further away from the cylinder has been omitted from the following figures. The first row of vectors is situated less than 3 millimeters from the cylinder.

The ensemble averaged velocity fields of figure 3.7 reveal that the periodic separation from the leading edge of the cylinder, located at $(x, y) = (-20, 20)$, causes a flapping motion of the shear layer during the course of the shedding cycle. As a result, the recirculation region that forms along the cylinder side also experiences a large-amplitude forcing at the vortex shedding frequency, f_s. In phase 1, the streamline plot in figure 3.2a revealed that a vortex was about to shed from the lower side of the cylinder. Consequently, the transverse extent of the separated region on the upper cylinder side, figure 3.7a, is declined. In phase 3, the situation is reversed and the separated region in figure 3.7c exhibits a streamwise growth that is approximately linear. While phase 1 and 3 thus represent two extremes of the forcing cycle, phases 2 and 4 accordingly reveal separated regions with intermediate extents.

Figure 3.8 demonstrates the significance of instantaneous velocity fluctuations in the flow. As the innermost portion of the flapping shear layer moves much more slowly than the outer part which is in contact with the free stream, a complex pattern of discrete swirling vortices is formed. However, the instantaneous samples still comply

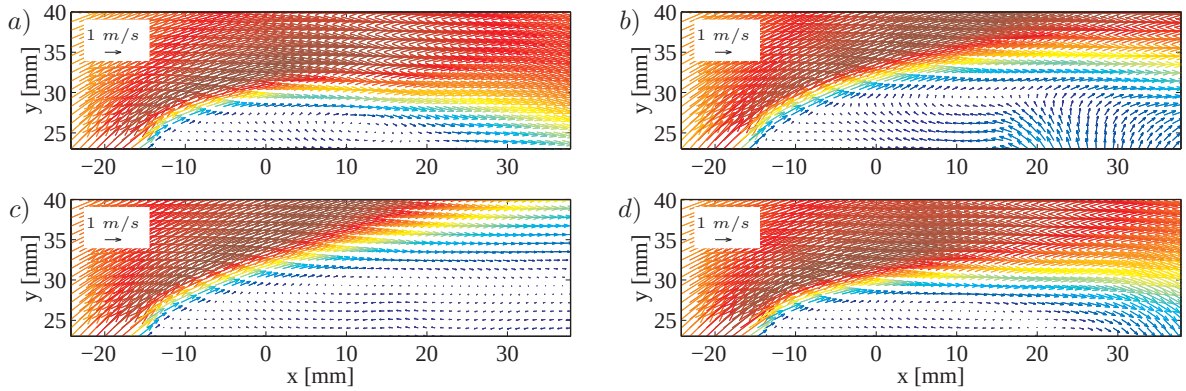

Figure 3.7: *Vector maps of the ensemble averaged velocity fields based on 1000 instantaneous samples. Color-coding according to the local speed. a) Phase 1 b) Phase 2 c) Phase 3 d) Phase 4. Field-of-view N2.*

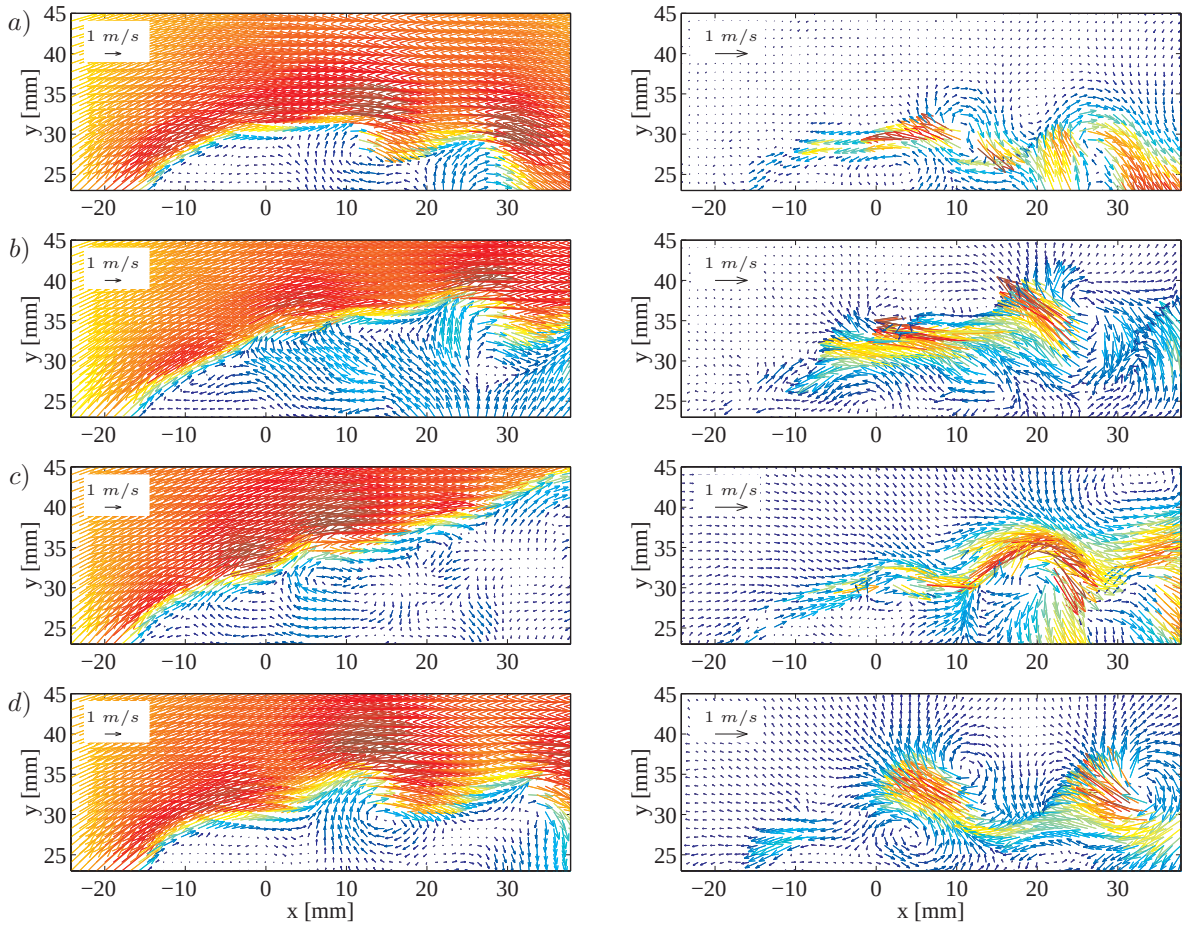

Figure 3.8: *Sample instantaneous velocity vector maps (left) and the corresponding instantaneous deviation $\vec{U} - \langle\vec{U}\rangle$ from the ensemble averages shown in figure 3.7. Color-coding according to the local speed. a) Phase 1 b) Phase 2 c) Phase 4 d) Phase 4. Field-of-view N2.*

to the periodic 'breathing' motion of the recirculation zone. In the right column of figure 3.8, the corresponding phase average has been subtracted from each sample to illustrate the wide range of length scales present in the recirculation zone.

Figure 3.9a shows $|\Omega_z|$ based on the instantaneous deviation velocities $\vec{U} - \langle\vec{U}\rangle$ of figure 3.8c and gives evidence of instantaneous trails of counter-rotating fluid cells that are convected along the separation line. These instantaneous structures have been smeared out in the time-mean vorticity distribution, figure 3.9b. Finally, figure 3.9c and d give the Reynolds normal stresses of the flow. The flapping of the shear layer gives rise to large values of $\overline{\langle uu\rangle}$ whereas $\overline{\langle vv\rangle}$ is relatively low in the vicinity of the cylinder side.

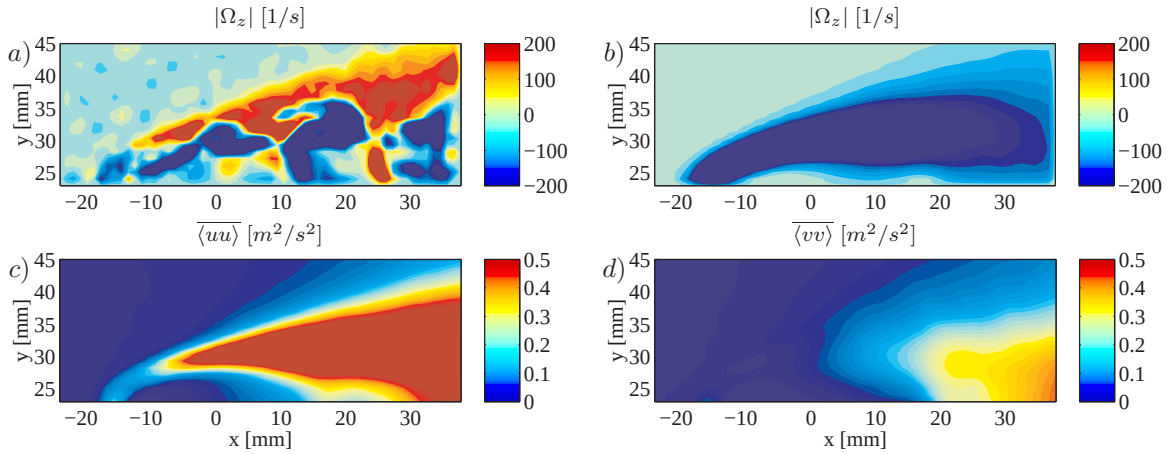

Figure 3.9: *a) $|\Omega_z|$ based on instantaneous deviation $\vec{U} - \langle\vec{U}\rangle$ (shown in figure 3.8c) b) $|\Omega_z|$ based on the mean of all phases 1–4 c) $\overline{\langle uu\rangle}$ d) $\overline{\langle vv\rangle}$. Field-of-view N2.*

3.3.3 Field-of-view Z2

Figure 3.10 shows sample PIV results acquired using zoom optics in field-of-view Z2 which is centered on the side of the cylinder and thus measures a sub-area of N2, but at a dramatically increased spatial resolution. Each vector is determined from interrogation areas of width $d_{I,Z} \approx 0.32$ mm which is only about twice the Kolmogorov scale estimated in section 3.3.1, and the first vector is evaluated at a position less than 1 mm from the wall.

The ensemble averaged streamline plot based on all acquired phases, figure 3.10a, reveals a well-defined time-mean recirculation zone extending about 8 millimeters from the cylinder face. As before the instantaneous samples, figures 3.10b–d, illustrate the complexity of the instantaneous spatial flow structures within the recirculation zone. The zoom mode results thus demonstrate that although PIV is mainly intended for measuring the large-scale structures of the flow, appropriate setup of the recording and processing parameters may enable to resolve also the smaller scales of the flow, e.g. the Taylor microscales, as was also shown by Ullum et al. [119] for the case of grid turbulence.

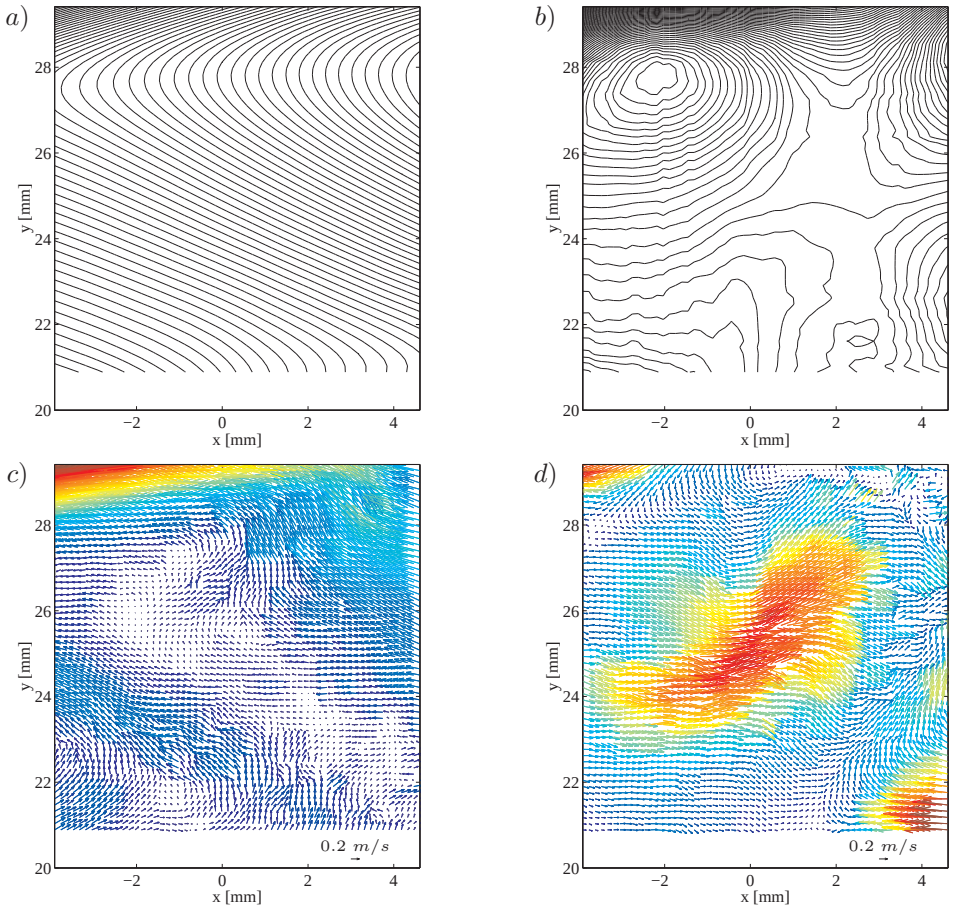

Figure 3.10: *a) Sectional streamlines based on mean of all phases b) Sample instantaneous sectional streamlines c)–d) Sample instantaneous deviations* $\vec{U} - \langle \vec{U} \rangle$ *from the ensemble averaged velocity field. Field-of-view Z2.*

3.4 Summary

In order to demonstrate the capabilities of the PIV technique in the study of a complex unsteady flow, this chapter presented PIV measurements of the two-dimensional flow past a stationary square cylinder. A statistically large number of conditionally sampled velocity vector maps were collected at four equidistant phases of the vortex shedding cycle, resolving both large and small scales of the flow.

Normal mode measurements of the near wake behind the cylinder confirmed that the flow is not only temporally but also spatially extremely complex with direct interaction between the two separated shear layers. Ensemble averaged statistics calculated at each phase showed good agreement with previous experimental and numerical investigations, and thus demonstrated that reliable turbulence statistics in a flow without homogeneous directions may be deduced from a large ensemble of PIV data, with the additional benefit of providing details on the instantaneous spatial flow structures.

Normal mode measurements of the recirculation zone that forms on the cylinder side because of flow separation at the leading edge revealed a periodic flapping of the shear layer. This caused the transverse extent of the recirculation zone to vary and led to the creation of complex instantaneous vortical structures. This flow region was also investigated in zoom mode resolving the smaller scales of the flow.

The present PIV setup allowed measurements 1–3 millimeters from the faces of the cylinder which is closer than previous experimental investigations. Combined with the instantaneous nature of the data, the present data base may therefore be used to give additional insight into the physics of the flow. For instance, the question whether the unsteady turbulent flow in the immediate vicinity of the cylinder resembles that of simple steady or unsteady turbulent flows, e.g. the flow around a bluff plate or the forced mixing-layer, may be addressed. This issue was investigated by Lyn and Rodi [73] using phase-resolved one-component LDV data. The data may also be explored further by the calculation of spatial correlation coefficients etc. However, this is beyond the scope of the present study which instead focuses on the use of the PIV data base as a tool to evaluate subgrid scale models used in Large Eddy Simulations, as will be described next.

Chapter 4

Experimental testing of LES

The move towards increased use of the Large Eddy Simulation (LES) technique in industrial applications raises the need for detailed evaluation of the models used in LES and their applicability to complex inhomogeneous flows. As a contribution to this end, the current PIV data base on the flow past a square cylinder is used to perform an experimental *a priori* test of the subgrid-scale (SGS) physics in this complex flow field, involving separation and the presence of large-scale coherent structures. The test compares the measured local SGS stresses and SGS dissipation to the predictions of five popular subgrid-scale models used in LES. It is also investigated how the SGS models drain energy from the resolved field, and SGS model coefficients are deduced from the experimental data in order to enable a comparison with the values usually employed in LES.

4.1 Introduction

In the LES technique, the large non-universal flow structures that are directly affected by the boundary conditions are computed explicitly, as in DNS, while the small scales are modeled via a subgrid-scale (SGS) model. The effect on the resolved scaled of having discarded the small scales appear through the subgrid-scale stress tensor τ_{ij} and the success of a LES depends to a large extent on the ability of the SGS model to represent this term. Because the modeling is done at a length scale smaller than the integral scale of the flow, it is hoped that the models can be simpler and more universal than their counterparts for Reynolds stresses [77]. However, while the development of RANS turbulence models have benefited from numerous measurements of the Reynolds stresses in a great variety of flows, only little is known about the subgrid-scale stresses. The physical modeling of the subgrid-scale stresses is often based on engineering approximations and relatively simple dimensional arguments, and a validation of the LES results and of the SGS models themselves is, therefore, essential.

In order to evaluate the correctness of a SGS model, two different methods of testing may be performed. The most straightforward is to perform a simulation for a particular flow using a complete LES code and then compare the results, e.g. mean velocities and statistical moments, with experimental data, as was e.g. done in the LES workshop organized by Rodi et al. [102]. While agreement of this form is desired for any simulation, this approach called *a posteriori* testing [96] has the disadvantage that

it is influenced by the numerical solution procedure. It therefore obstructs SGS model evaluation since the filtering, modeling and numerical parts of LES are interrelated in an unclear way.

A priori studies, on the other hand, decouple the individual LES components and enable testing of the physical content of the SGS model, without actually performing a LES [96]. *A priori* tests were pioneered by Clark et al. [24] and McMillan and Ferziger [74] and consist of using fully resolved velocity fields to compare the local instantaneous SGS stresses with the prediction of a SGS model. The method yields useful information on the physical phenomena that govern energy transfer between the resolved and unresolved scales [97] and has also led to the development of new SGS models [10, 69]. Traditionally, *a priori* tests have been based on DNS data which are fully 3D and may be filtered to give the exact subgrid-scale stresses or any derived quantity. The major drawback of DNS based *a priori* analyses is the restriction to simple near-equilibrium flows with low Reynolds numbers. Consequently, such studies have mainly concentrated on isotropic turbulence [24, 96].

To investigate the SGS physics of more complex flows, *a priori* tests may instead be based on experimental data, which offer the opportunity to substantially raise the Reynolds numbers, at the expense of more incomplete data sets. Experimental *a priori* studies using one-point hotwire anemometry data have been performed by Meneveau [77] in grid turbulence and recently by O'Neil and Meneveau [90] in the wake of a circular cylinder in uniform cross flow. Since PIV is an instantaneous whole-field measurement technique, it is also well suited to this task as demonstrated by Liu et al. [69], who investigated the subgrid-scale physics in the far-field of a turbulent free jet. The objective of the present study is to supplement these previous investigations with a study of the instantaneous SGS quantities in the wake and shear layer regions of the flow past a square cylinder. A key issue is to demonstrate the influence of large-scale coherent structures on SGS events.

4.2 Large Eddy Simulation

This section briefly outlines the theory behind LES and describes the main characteristics of the five SGS models that are tested. For an in-depth description of the history and evolution of LES, see e.g. the comprehensive reviews given by Rogallo and Moin [103] and, more recently, Lesieur and Métais [66].

In order to distinguish between small and large eddies in LES, a spatial filter is introduced that separates the turbulent motion into large resolved scales and unresolved subgrid-scales (SGS). Formally, this spatial low-pass filtering operation is defined by

$$\bar{f}(x) = \int f(x')G(x,x')dx' \tag{4.1}$$

where G is the filter function that determines the size and structure of the small scales. G may be defined explicitly or implicitly implied by the discretization mesh. Application of the filter operation, Eq. (4.1), to the Navier-Stokes and continuity equations gives the filtered governing equations for the large-scale variables

$$\frac{\partial \bar{u}_i}{\partial t} + \frac{\partial}{\partial x_j}(\bar{u}_i\bar{u}_j) = -\frac{1}{\rho}\frac{\partial \bar{p}}{\partial x_i} - \frac{\partial \tau_{ij}}{\partial x_j} + \nu\frac{\partial^2 \bar{u}_i}{\partial x_j \partial x_j} \tag{4.2}$$

$$\frac{\partial \bar{u}_i}{\partial x_i} = 0 \tag{4.3}$$

which are solved in LES. The unresolved scales of motion act on the resolved velocity field as stresses which are termed subgrid-scale stresses

$$\tau_{ij} = \overline{u_i u_j} - \bar{u}_i \bar{u}_j \tag{4.4}$$

and must be modeled by a SGS model to close the system of equations. The role of the SGS model is to parameterize the unresolved subgrid scales as a function of the resolved velocity field.

4.2.1 Subgrid scale models

Five SGS models, based on two different base models, are considered in this study. The simplest and most commonly used subgrid-scale model is the Smagorinsky model [107]

$$\tau_{ij}^{SM} = -2\Delta^2 C_S^2 |\bar{S}| \bar{S}_{ij} \tag{4.5}$$

where C_S is a dimensionless model coefficient, Δ the characteristic filter width which typically is set proportional (or equal) to the volume $(\Delta x \Delta y \Delta z)^{1/3}$ of the computational cell, and $|\bar{S}| = \sqrt{2\bar{S}_{ij}\bar{S}_{ij}}$ is the magnitude of the large-scale strain-rate tensor $\bar{S}_{ij} = \frac{1}{2}\left(\partial \bar{u}_i/\partial x_j + \partial \bar{u}_j/\partial x_i\right)$. The Smagorinsky model is thus an eddy-viscosity type model that assumes that the SGS stress tensor and the resolved rate of strain are aligned. Furthermore, the model is based on the equilibrium assumption that energy production and dissipation in the small scales are in balance, and it thus implicitly assumes that the subgrid-scales adjust instantaneously to changes in the large field [94]. Previous *a priori* studies [24, 96, 68] have shown that these features are not realistic and, consequently, eddy-viscosity models have proved unable to reproduce the details of the SGS stresses and the energy exchange on a local and instantaneous level. Despite this incorrect local behavior, the simple Smagorinsky model predicts the global mean dissipation fairly accurately and it has therefore been successfully applied to many flows.

Another model which has gained substantial interest in recent years is the scale-similarity model, originally proposed by Bardina et al. [10]. This type of model employs multiple filtering operations to identify the smallest scales of the resolved field as these have been shown to be the most active in the interaction with the unresolved scales [97]. In the form most commonly used today, the scale-similarity model reads [69]

$$\tau_{ij}^{SS} = C_L \mathcal{L}_{ij}; \qquad \mathcal{L}_{ij} = \left(\widehat{\bar{u}_i \bar{u}_j} - \hat{\bar{u}}_i \hat{\bar{u}}_j\right) \tag{4.6}$$

where $\mathcal{L}_{ij}$ are the resolved turbulent stresses and a hat denotes a second filtering operation performed at scale $\hat{\Delta} = 2\Delta$ as opposed to Δ in the original Bardina model [10]. This revised similarity model was proposed by Liu et al. [69] based on a detailed analysis of the SGS energy fluxes between consecutive velocity bands in the far-field of a round jet. They observed that the local stresses at different filter levels are similar and, consequently, C_L is expected to be of the order one [90]. Whereas the scale-similarity model has shown a high degree of correlation with the real SGS stresses in *a priori* tests [69, 90], it generally does not dissipate enough energy. It is therefore usually combined with the Smagorinsky model to yield a mixed model

$$\tau_{ij}^{MX} = \tau_{ij}^{SM} + \tau_{ij}^{SS} \tag{4.7}$$

that has been frequently used and with considerable success, as discussed by Sarghini et al. [104] in a recent review of scale-similar models.

The SGS models presented so far all involve model coefficients which need to be prescribed in a LES. Since different flow regions may require different coefficient values, it has shown beneficial to use a dynamic procedure, introduced by Germano et al. [38], to determine the model coefficients iteratively from the energy content of the smallest resolved scales. This dynamic procedure also involves multiple filters and yields model coefficients that varies in both space and time and thus enables the simulation to adjust to the local state of the flow. It may, however, also lead to numerical instabilities which are usually avoided by averaging over regions of homogeneity [38], if they exist, or along fluid pathlines [79]. A localized dynamic procedure proposed by Piomelli and Liu [95] is also applicable to complex flows as recently demonstrated by Byskov [17].

In the present study, two dynamic SGS models are considered. The first is the original local dynamic variant of the Smagorinsky model [38, 67]

$$\tau_{ij}^{DSM} = -2\Delta^2 C_{S,DSM}^2 |\bar{S}|\bar{S}_{ij}; \qquad C_{S,DSM}^2 = \frac{M_{ij}\mathcal{L}_{ij}}{M_{ij}M_{ij}} \tag{4.8}$$

where $M_{ij} = 2\Delta^2(\widehat{|\bar{S}|\bar{S}}_{ij} - 4|\hat{\bar{S}}|\hat{\bar{S}}_{ij})$, and the second is a dynamic version of the mixed model given by (see e.g. [104, 130])

$$\tau_{ij}^{DMX} = -2\Delta^2 C_{S,DMX}^2 |\bar{S}|\bar{S}_{ij} + C_{L,DMX}\left(\widehat{\bar{u}_i\bar{u}_j} - \hat{\bar{u}}_i\hat{\bar{u}}_j\right) \tag{4.9}$$

The two model coefficients in Eq. (4.9) are determined simultaneously by applying the dynamic procedure, i.e. the Germano identity [38] and the least-squares error minimization procedure introduced by Lilly [67]. This involves an additional filtering at a scale $2\hat{\Delta} = 4\Delta$ and results in rather lengthy expressions for $C_{S,DMX}^2$ and $C_{L,DMX}$ which, for the sake of brevity, are not given here but can be found in e.g. Meneveau and Katz [78]. Several other SGS models have been proposed in the literature, but the equations (4.5)–(4.9) represent the five commonly used model variants that are investigated in the present *a priori* study.

4.3 Experimental *a priori* test

This section presents the main results from an experimental *a priori* test based on the planar PIV data presented in the previous chapter. The analysis procedure follows the approach described by Liu et al. [69]. The general idea is to use the two-dimensional PIV data, given at a discrete mesh with spacing δ, to evaluate the 'true' subgrid stresses τ_{ij} according to their definition, Eq. (4.4). This is then compared to the predictions of the five SGS models, which are calculated from equations (4.5)–(4.9) by sampling the PIV data at a coarser mesh with spacing $\Delta > \delta$, representing the mesh size resolution affordable for LES. In this way the test is consistent with the limited information available in an actual LES.

As the PIV data are only two-dimensional, only certain components of the SGS stress tensors can be evaluated, and merely by the application of two main assumptions. The first is that a 2D filtering of the PIV data in the plane of the light sheet may,

without loss of generality, replace the 3D filtering usually employed in *a priori* tests based on DNS data. This is supported by the findings of Murray et al. [86] who showed 2D filtering to be nearly equivalent to 3D filtering, at least above $y^+ \simeq 10$, i.e. outside the buffer layer of wall-bounded flows. The other working assumption is that the small scales are isotropic. This assumption of SGS isotropy may not strictly hold, especially not for large filter widths Δ/δ, but it is not expected to influence trends and qualitative results significantly.

In order to investigate the influence of the LES mesh size on the SGS model performance, the analysis is repeated for different filter widths in the range $\Delta/\delta = 3$–17. Furthermore, it utilizes PIV data acquired in both normal and zoom mode, i.e. $\delta = \delta_N$ and $\delta = \delta_Z$, respectively. Expressed in terms of the Kolmogorov scale estimated in section 3.3.1, this corresponds to filter widths of $\Delta/\eta = 15$–95 and $\Delta/\eta = 2$–14 in normal and zoom mode, respectively. The results presented in the following are based on 1000 instantaneous PIV vector maps collected in phase 3 of the vortex shedding cycle in field-of-views N3/Z1 in the wake and N2/Z2 on the side of the cylinder, see figure 3.1.

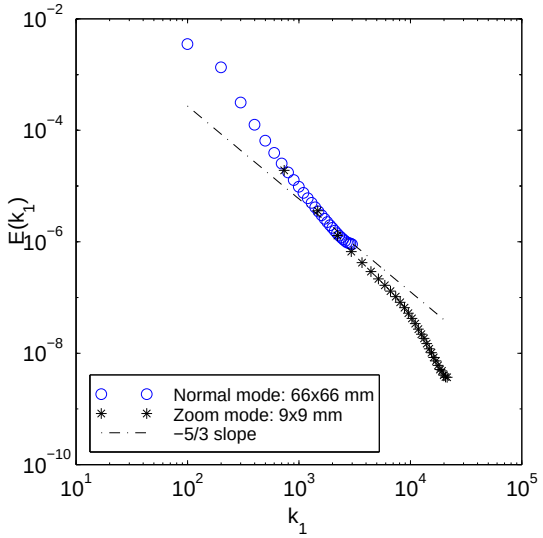

Figure 4.1: *Estimate of the spatial 1D energy spectrum of the PIV velocity fields measured in normal and zoom modes, respectively, as a function of wave number.*

Figure 4.1 shows an estimate of the spatial 1D energy spectrum of the measured velocity fields as a function of wave number, calculated using the Blackmann-Tukey method, see e.g. Bendat and Piersol [12]. The spectrum indicates that the inertial-range scales of the flow are adequately resolved by the PIV measurements, although a departure from the familiar -5/3 Kolmogorov slope is seen in this complex flow field. However, the spectrum has proved to be very sensitive to measurement noise and the choice of window function and, consequently, too much weight should not be attributed to the slopes seen in figure 4.1. The important point to note is that for the present *a priori* analysis, the interest is not to resolve the dissipation range, but to filter the data at length scales which pertain to the inertial range [69].

4.3.1 SGS stresses

In order to calculate the measured and modeled SGS stresses, filtered velocities are obtained from the PIV data via

$$\bar{u}_i(x,y) = \frac{1}{(\Delta/\delta)^2} \sum\sum u_i(x',y') \tag{4.10}$$

where the summation is performed locally over a square with side length Δ and center at (x,y). This spatial averaging procedure is equivalent to a two-dimensional box filter with characteristic width Δ and therefore corresponds to the implicit filter frequently used in finite-volume based LES codes. Subsequently, the (11), (22) and (12)-components of the SGS stress tensor τ_{ij} are computed from the PIV data according to Eq. (4.4). Large-scale velocity gradients and thus the strain-rate tensor elements $\bar{S}_{ij}$ are obtained from centered finite differences sampled on the coarse (LES) mesh with spacing Δ, again refraining from using information stored on the fine (PIV) mesh which would not be available during an actual LES [69]. The magnitude of the local large-scale strain-rate tensor $|\bar{S}|$ is also needed. As the measured data only include $\bar{S}_{11}$, $\bar{S}_{22}$, $\bar{S}_{12}$ and $\bar{S}_{33} = -(\bar{S}_{11} + \bar{S}_{22})$, SGS isotropy, i.e. $\bar{S}_{23} \approx \bar{S}_{13} \approx \bar{S}_{12}$, is assumed for the remaining terms to give the following 2D-approximation for $|\bar{S}|$ [69]:

$$|\bar{S}| = \sqrt{2\bar{S}_{ij}\bar{S}_{ij}} \approx [4(\bar{S}_{11}^2 + \bar{S}_{22}^2 + \bar{S}_{11}\bar{S}_{22} + 3\bar{S}_{12}^2)]^{1/2} \tag{4.11}$$

Figure 4.2 shows a comparison of the ensemble averaged (22)-components of the SGS-stress tensor calculated in phase 3 in field-of-view N3, with a fixed filter width of $\Delta/\delta_N = 5$. It reveals that the mixed model (MX) reproduces the measured SGS stresses very well on a local basis. The MX contours are smoother than the measured τ_{22} because of the double-filtering performed in the similarity term. Comparing the SGS stress with the out-of-plane vorticity contour plot given in the lower right of figure 4.2 suggests that there exists a strong correlation between large-scale coherent structures and the SGS physics, as was also observed by Piomelli et al. [97] and O'Neil and Meneveau [90], although the exact relation is not clear.

Correlation coefficients

To quantify the prediction of the SGS models, correlation coefficients between the measured and modeled SGS stress tensors were calculated. The correlation coefficient ρ between two variables a and b is defined by

$$\rho(a,b) = \frac{\langle ab\rangle - \langle a\rangle\langle b\rangle}{[(\langle a^2\rangle - \langle a\rangle^2)(\langle b^2\rangle - \langle b\rangle^2)]^{1/2}} \tag{4.12}$$

Using Eq. (4.12) and by averaging over all available data points in the center of each PIV vector map and over all 1000 vector maps, individual elements of the correlation coefficients $\rho(\tau_{ij}^{PIV}, \tau_{ij}^{LES})$ are calculated. They give a measure of the abilities of the SGS models to reproduce the real stresses on a local and instantaneous basis. A high correlation is desirable, even though this is not a necessary condition for the prediction of correct flow statistics, as shown by Meneveau [77] who also noted that the real and

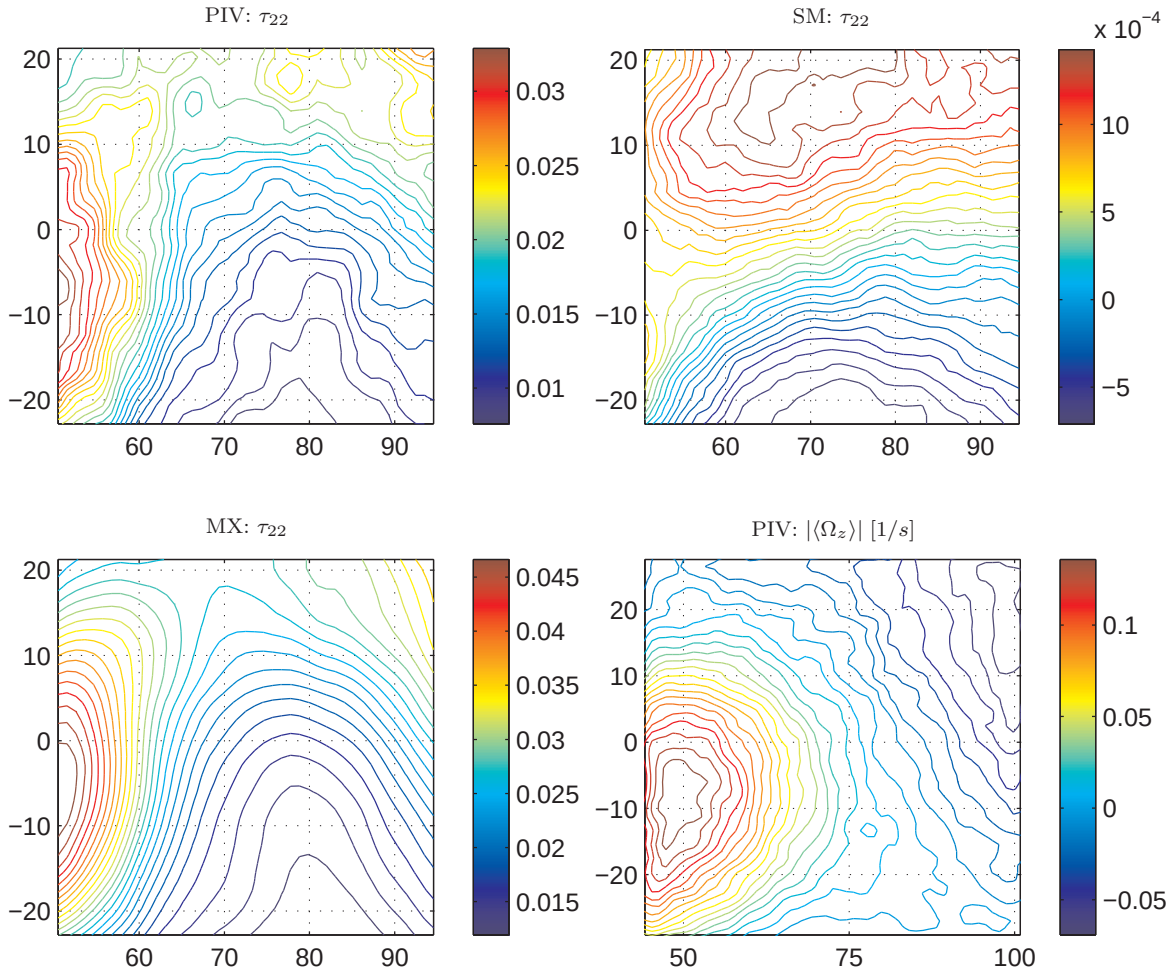

Figure 4.2: *Measured and modeled SGS stress tensor component τ_{22} calculated for a filter width of $\Delta/\delta_N = 5$ and based on ensemble averages of 1000 PIV vector maps acquired in phase 3. Also shown is the ensemble averaged out-of-plane vorticity $|\langle\Omega_z\rangle|$ (lower right). Field-of-view N3.*

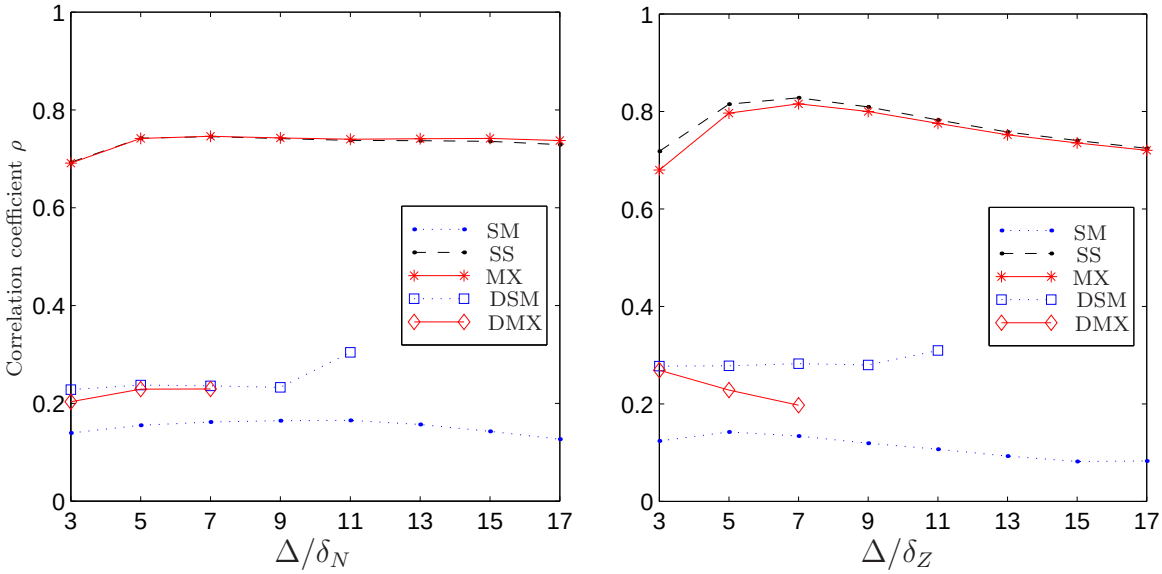

Figure 4.3: *Correlation coefficients ρ between measured and modeled SGS stress (mean of (11), (22) and (12) components) as a function of filter width Δ/δ. Left: Normal mode. Right: Zoom mode.*

modeled stress tensors could differ by an divergence-free tensor, e.g. a constant, and still allow for the correct flow statistics as the impact on Eq. (4.2) is identical.

Figure 4.3 shows the mean correlation coefficients between measured and modeled SGS stresses as a function of filter width Δ/δ for normal and zoom modes, respectively. Tests have shown that the ensemble of 1000 vector maps is fully sufficient to obtain statistical convergence of SGS quantities and correlation coefficients. As expected, a low correlation coefficient of $\rho = 0.15$ is obtained with the Smagorinsky model (SM), essentially because it falsely assumes that the SGS stresses and the local rate of strain are aligned. The scale similarity model (SS) is considerably better ($\rho = 0.7$–0.8) at reproducing the real stresses. These results are in agreement with former findings based on both experimental [77, 69, 90] and DNS data [24]. The mixed model (MX) is seen to attain the same high correlation as the similarity model itself. The reason is that the Smagorinsky part of the SGS stress is generally much smaller than the similarity part, see figure 4.2. Finally, the (local) dynamic model variants (DSM and DMX) reveal a better correlation ($\rho = 0.2$–0.3) than the standard Smagorinsky model, confirming the advantageous use of the dynamic procedure in non-equilibrium flows.

4.3.2 SGS energy dissipation

As the small dissipative scales are not resolved in a Large Eddy Simulation, the main characteristic of a SGS model should be its ability to remove energy from the large resolved scales [97]. Therefore, in this section it is explored how the subgrid-scale stresses affect the kinetic energy of the resolved field and hence to what extent the SGS models predict the correct SGS energy dissipation.

Piomelli et al. [93], among others, have shown that the net energy interchange between resolved and unresolved scales is governed by the SGS dissipation

$$\epsilon_{SGS} = \tau_{ij}\bar{S}_{ij} \tag{4.13}$$

which is, on the average, a dissipative term in the transport equation for the total resolved kinetic energy, $\frac{1}{2}\bar{q}^2 = \frac{1}{2}\bar{u}_i\bar{u}_i$, and a production term in the transport equation for SGS energy. It thus represents the drain that is usually associated with the energy cascade, of large-scale kinetic energy into unresolved motion. Locally, though, Piomelli et al. [93] found evidence of reversed energy flow from small to larger scales ($\epsilon_{SGS} > 0$) which is termed backscatter. It may be noted that in the context of LES, "dissipation" in the large-scale field does not imply the action of viscous forces, but refers to kinetic energy being transferred to the small-scale field [10].

In order to calculate the SGS energy dissipation, small-scale isotropy is again assumed for terms entering the contraction on the right-hand side of Eq. (4.13) which are not measured. The energy-flux from resolved to unresolved scales is thus estimated from [69]:

$$\Pi(\Delta) = -\langle\epsilon_{SGS}\rangle \approx -\frac{1}{2}\left(\langle\tau_{11}\bar{S}_{11}\rangle + \langle\tau_{22}\bar{S}_{22}\rangle - \langle\tau_{11}\bar{S}_{22}\rangle - \langle\tau_{22}\bar{S}_{11}\rangle + 12\langle\tau_{12}\bar{S}_{12}\rangle\right) \tag{4.14}$$

where the averages are performed over the entire data sets.

Figure 4.4 shows a comparison between the measured and predicted SGS energy-flux $\Pi = -\langle\epsilon_{SGS}\rangle$, calculated for a fixed filter width of $\Delta/\delta_N = 5$ in field-of-view N2 situated on one side of the cylinder, see figure 3.1. The velocity vector map and vorticity contour plot in the upper row of figure 4.4 show that the flow separates at the leading edge and creates a recirculation zone along the cylinder side wall, as discussed in section 3.3.2. From the PIV data, localized areas of highly negative Π, backscatter, are clearly visible in this complex flow region. The similarity and mixed models are seen to reproduce the details of the Π distribution very well whereas the purely dissipative Smagorinsky model smears out the contours and is unable to predict the qualitative features. However, a comparison of the mean value of Π predicted by the Smagorinsky model with the large-scale estimate $\epsilon \approx u_{rms}^3/l_i \sim 3$ of the overall energy dissipation, suggests that the two dissipation fluxes are of the same order of magnitude.

4.3.3 SGS model coefficients

Both SGS base models considered in this study contain a model coefficient that is set constant throughout the flow domain and needs to be prescribed in an actual LES. In order to ascertain the ability of the SGS models to predict the correct SGS energy dissipation with one single coefficient for different filter widths, values of C_S and C_L have been estimated from the experimental data. Following Meneveau [77], the model coefficients were deduced by assuming that the SGS models reproduce the mean SGS dissipation $\langle\epsilon_{SGS}\rangle$ correctly. This condition yields

$$C_S^2 = -\frac{\langle\tau_{ij}\bar{S}_{ij}\rangle}{2\Delta^2\langle|\bar{S}|\bar{S}_{ij}\bar{S}_{ij}\rangle} = -\frac{\langle\tau_{ij}\bar{S}_{ij}\rangle}{\Delta^2\langle|\bar{S}|^3\rangle} \tag{4.15}$$

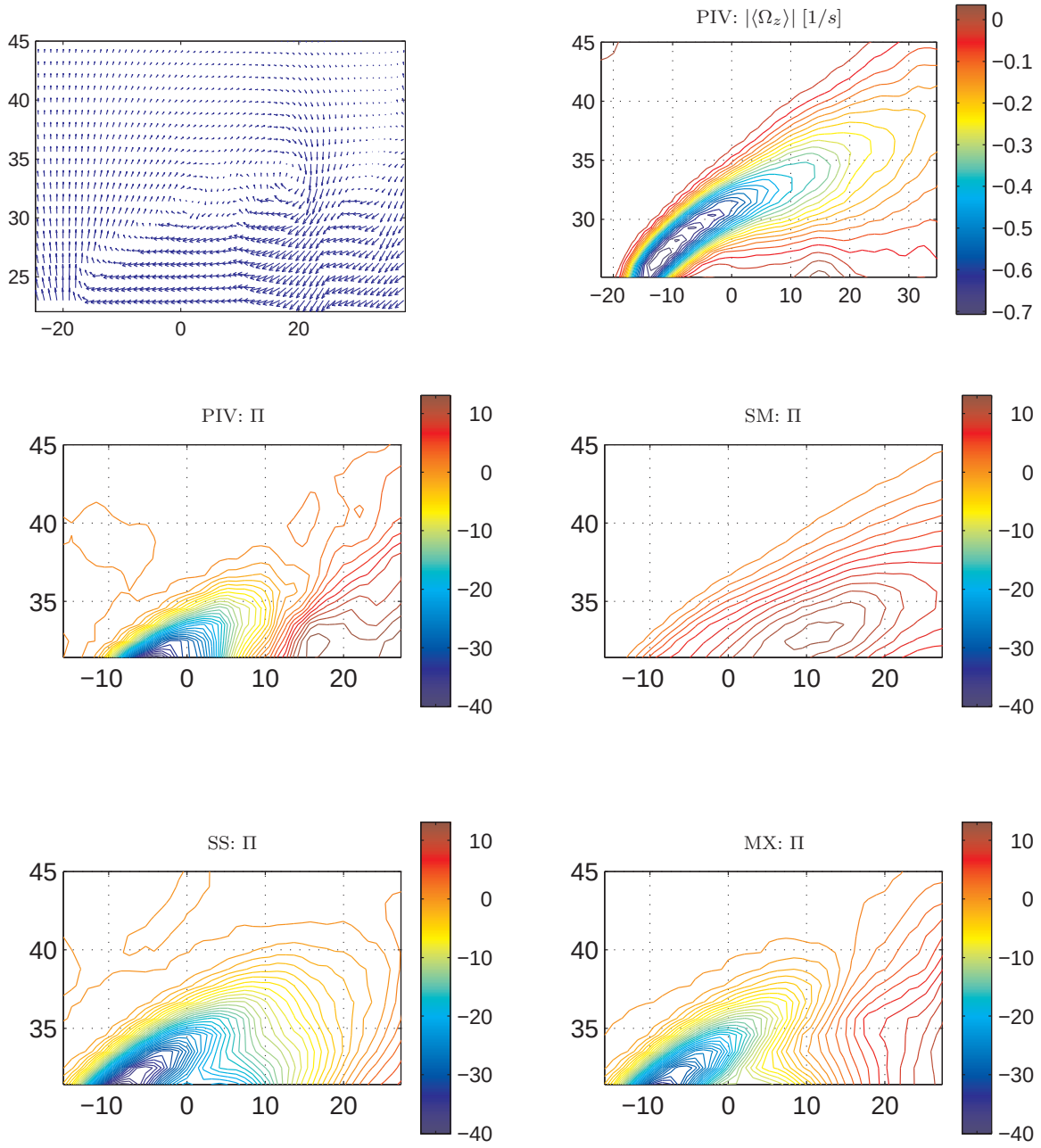

Figure 4.4: *Measured and modeled SGS energy-flux* $\Pi = -\langle\epsilon_{SGS}\rangle$ *calculated for a filter width of* $\Delta/\delta_N = 5$ *and based on ensemble averages of 1000 PIV vector maps acquired in phase 3. Also shown is a sample instantaneous velocity field (upper left) and the ensemble averaged out-of-plane vorticity* $|\langle\Omega_z\rangle|$ *in phase 3 (upper right). Field-of-view N2.*

for the Smagorinsky model coefficient and

$$C_L = -\frac{\langle \tau_{ij} \bar{S}_{ij} \rangle}{\langle \mathcal{L}_{ij} \bar{S}_{ij} \rangle} \tag{4.16}$$

for the similarity scale model coefficient.

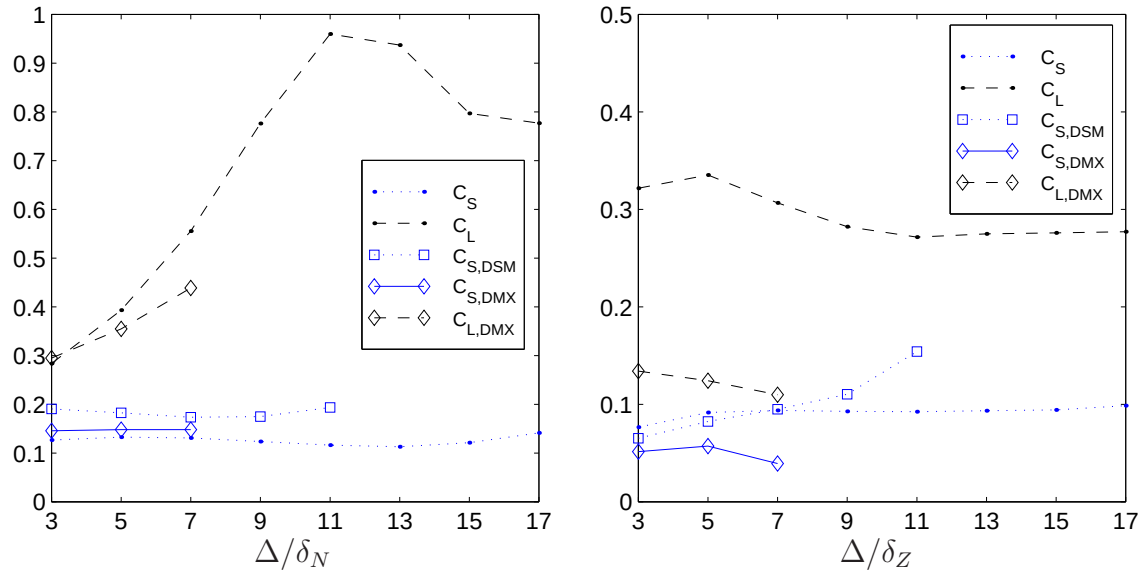

Figure 4.5: *SGS model coefficients C_S and C_L deduced from SGS dissipation balance (solid symbols) and $C_{S,DSM}$, $C_{S,DMX}$ and $C_{L,DMX}$ determined by the dynamic procedure (open symbols). Left: Normal mode. Right: Zoom mode.*

Figure 4.5 compares the model coefficients deduced from the SGS dissipation balances, equations (4.15) and (4.16), to those determined by the dynamic procedure, equations (4.8) and (4.9). Figure 4.5 reveals that the Smagorinsky coefficients obtained from the experimental data are fairly constant over the filter widths considered and are, furthermore, within usually accepted ranges, i.e. $0.06 < C_S < 0.2$. For the normal mode case (left), the dynamically determined coefficients $C_{S,DSM}$ and $C_{S,DMX}$ follow the same trends but overestimate C_S by up to 25%. The scale similarity coefficient C_L has the expected magnitude ($C_L \sim \mathcal{O}(1)$) [69], but its high variability in normal mode suggests that models involving a similarity term are best implemented in conjunction with the dynamic procedure. For the zoom data (right), the coefficients are generally lower and a greater discrepancy between values deduced from SGS dissipation balance and those determined from the dynamic procedure is observed. Here, however, the C_L is fairly constant and furthermore corresponds with the value of $C_L = 0.45 \pm 0.15$ recommended by Liu et al. [69]. Overall, the study suggests that the model coefficient values commonly employed in actual LES calculations are also applicable to the current complex flow.

4.4 Summary

Based on two-dimensional PIV data acquired in the near wake of a square cylinder, an experimental *a priori* test of subgrid-scale (SGS) models employed in Large Eddy Simulations of turbulent flows were performed. The study compared the measured instantaneous SGS stresses and SGS dissipation with the predictions of five commonly used SGS models, ranging from the simple Smagorinsky model over the scale similarity model to mixed and dynamic variants of these two base models.

The test confirmed previous findings that eddy-viscosity models such as the Smagorinsky model cannot reproduce the details of the stresses and of the energy exchange between resolved and unresolved scales very accurately on a local and instantaneous level. It also confirmed that, despite this incorrect local behavior, the Smagorinsky model still predicts the global dissipation fairly accurately. The reason seems to be that only the mean stresses are needed to compute the mean flow.

Mixed and dynamic models based on similarity between scales have proved better at reproducing the details of the SGS physics. This is consistent with previous findings in simpler flows based on both experimental and DNS data. The results suggest that the presence of large-scale coherent structures strongly affects the distribution of subgrid-scale stresses and dissipation. The present database can be explored further in order to elaborate on this correlation between large and small-scale events and on the influence of filter widths.

In conclusion, this and the previous chapters have demonstrated that the PIV technique may provide valuable information on a complex unsteady flow at a variety of levels. Apart from a direct insight into the instantaneous spatial structures, reliable turbulence statistics as well as subgrid-scale quantities usable for LES model evaluation may be deduced from a large ensemble of conditionally sampled vector maps. This promising observation concludes this part of the dissertation. In the next part, Part C, the feasibility of the PIV technique to complex flows will be further tested through the application of PIV to the rotating passages of a centrifugal pump impeller.

Part C

Centrifugal impeller

Chapter 5

Theory of pump flows

This chapter is the first of four chapters that concern the application of PIV to the rotating passages of a centrifugal pump impeller. The velocity field that develops in a pump impeller is exceedingly complex and results from interactions between a variety of inviscid and viscous flow phenomena. Therefore, in order to provide a basis for the interpretation of the acquired experimental data, this chapter gives a general introduction to the theory of pump flows and their prediction. Starting with simple idealized approaches, the chapter briefly describes different flow analysis methods at increasing levels of complexity. The aim is to illustrate the type of information that each method may be expected to provide on the impeller flow and, furthermore, to classify the different flow effects according to the mechanisms that generate them.

First, attention is devoted to the development of dimensionless parameters as these will be needed in the next chapter for the design of experimental operating conditions. Then, one- and two-dimensional inviscid analysis methods for predicting the relative velocity distribution in the impeller passage are described. Since viscous effects are important in real impeller flows, especially at off-design conditions, an introduction to secondary flow and a brief discussion of unsteady flow phenomena is also given. The chapter concludes with a summary of the flow features that may be of relevance in the impeller under investigation.

5.1 Introduction

The successful development of efficient pumps requires an understanding of a flow that is generally turbulent, three-dimensional, highly geometry-dependent and unsteady. Over the years, a variety of different analysis methods have been developed which may be used at different stages of the design process, depending on the type of information sought. In order of increasing complexity these methods include:

- Dimensional analysis
- 1D or mean line analysis
- 2D inviscid and viscous methods
- Advanced 3D viscous CFD methods

A natural starting point is a dimensional analysis which provides a tool for designing model tests and correlating the recorded data. A one-dimensional or mean line analysis gives the global characteristics of the flow field, whereas a two-dimensional approach is necessary to explain, at least approximately, local velocity distributions. The 3D equivalent would be expected to provide more details of the local flow features, including secondary flows, but is not explicitly treated here.

5.2 Dimensional analysis

Dimensional analysis is successfully applied to turbomachinery as a means of disclosing important dimensionless parameters characterizing the machine performance. These parameters are a useful tool in the design and testing of turbomachines as they allow scaling of performance characteristics between different operating conditions, e.g between model and full-scale pump geometries.

Dimensionless parameters follow from a dimensional analysis utilizing the Buckingham Π theorem. The first important step of such an analysis consists of identifying the independent variables that govern the quantities of interest. For a pump, central performance parameters are the head H, expressed as energy per unit weight, and the power input P. These are, in turn, functions of the volume flow rate Q, the angular speed ω of the impeller, the impeller diameter D, and fluid properties. This gives the following functional relationships

$$H = g_1\left(Q, \omega, D, \rho, \mu\right) \quad \text{and} \quad P = g_2\left(Q, \omega, D, \rho, \mu\right)$$

Application of the Π theorem now allows development of the significant dimensionless groups (see e.g. Fox and McDonald [37] for details)

$$\Pi_1 = \frac{gH}{\omega^2 D^2} = f_1\left(\frac{Q}{\omega D^3}, \frac{\rho\omega D^2}{\mu}\right), \qquad \Pi_3 = \frac{Q}{\omega D^3} \tag{5.1}$$

$$\Pi_2 = \frac{P}{\rho\omega^3 D^5} = f_2\left(\frac{Q}{\omega D^3}, \frac{\rho\omega D^2}{\mu}\right), \qquad \Pi_4 = \frac{\rho\omega D^2}{\mu} \tag{5.2}$$

The dimensionless head coefficient Π_1 and power coefficient Π_2 are seen to depend on two dimensionless groups, the flow coefficient, Π_3, and a form of Reynolds number, Π_4. The functions f_1 and f_2 must be determined experimentally.

5.2.1 Dimensionless parameters

From the generalized non-dimensional parameters introduced above, all essential pump parameters may be derived. This section presents the dimensionless parameters used in the present study. To facilitate comparison with pump investigations in the literature, two alternative formulations of each dimensionless parameter are given.

The Reynolds number is based on the impeller diameter D and a characteristic impeller speed, either the circumferential speed U_2 at the outlet, or $\omega = 2\pi f$

$$Re_I = \frac{U_2 D}{\nu} = \frac{\pi f D^2}{\nu} \quad \text{or} \quad Re_{II} = \frac{\omega D^2}{\nu} = \frac{2\pi f D^2}{\nu} = 2Re_I \tag{5.3}$$

The flow coefficient is defined by normalizing the volume flow rate using U_2 and the outlet area A_2

$$\phi_I = \frac{Q}{A_2\, U_2} = \frac{Q}{4 f b_2 \pi^2 R_2^2} \quad \text{or} \quad \phi_{II} = \frac{Q}{U_2\, \pi\, R_2^2} = \frac{Q}{2 f \pi^2 R_2^3} = \frac{2b_2}{R_2}\phi_I \tag{5.4}$$

where b_2 is the height of the impeller channel at the outlet, and the alternative form ϕ_{II} is defined by Ubaldi et al. [116]. Head coefficients are given by

$$\Psi_I = \frac{gH}{U_2^2} \quad \text{or} \quad \Psi_{II} = \frac{2gH}{U_2^2} = 2\psi_I \tag{5.5}$$

where Ψ_{II} expresses the head as a fraction of the maximum theoretical head obtainable at zero flow and no prerotation. Many other parameters may be deduced from the fundamental groupings given in Eqs. (5.1) and (5.2). One useful parameter is the specific speed N_s which is formed by combining the flow and head coefficients and eliminating the impeller diameter

$$N_s = \frac{{\Pi_3}^{1/2}}{{\Pi_1}^{3/4}} = \omega \frac{Q^{\frac{1}{2}}}{(gH)^{\frac{3}{4}}} = \omega \frac{(\phi_I A_2)^{\frac{1}{2}}}{U_2 (\psi_I / g)^{\frac{3}{4}}} \tag{5.6}$$

The specific speed at the design point is a form parameter used to characterize the hydraulic design features of a pump. A low N_s is effectively produced by a radial-flow pump and a high N_s by an axial-flow pump. While Eq. (5.6) is a dimensionless number, it is engineering practice to use an inconsistent set of units. Hence, adopting the convention used by most pump manufacturers, in the present study the specific speed is calculated as $N_s = nQ^{1/2}/H^{3/4}$ where n is the rotational speed expressed in revolutions per minute, rpm, and Q is stated in m^3/s and H in m.

5.2.2 Scaling laws

The dimensionless coefficients developed above may be used in conjunction with the similarity rules to establish the conditions that allow scaling of results obtained in model tests. Generally, the following similarity rules must be observed to ensure similar flows [37]:

- Geometric similarity: all dimensions must differ by the same scale ratio, preserving all angles.
- Kinematic similarity: all velocities at corresponding points must be in the same direction and related by a constant scale factor. In an impeller this is only true if there is no cavitation.
- Dynamic similarity: all forces at corresponding points must be parallel and related in magnitude by a constant scale factor.

When dynamic similarity exists, data acquired in a model may be scaled quantitatively to those of the actual pump. Based on the dimensionless Π groups developed in equations (5.1) and (5.2), complete dynamic similarity in pump performance tests would

require identical flow coefficients and Reynolds numbers. However, Reynolds number effects have been found to be an order of magnitude smaller than flow coefficient effects, provided the Reynolds number is high [112]. Therefore, assuming geometric and kinematic similarity, it suffices to duplicate the flow coefficient

$$\frac{Q_1}{\omega_1 D_1^3} = \frac{Q_2}{\omega_2 D_2^3} \tag{5.7}$$

to obtain dynamic similarity between a full-scale and a model flow, here denoted 1 and 2, respectively. This leads to

$$\frac{H_1}{\omega_1^2 D_1^2} = \frac{H_2}{\omega_2^2 D_2^2} \quad ; \quad \frac{P_1}{\rho_1 \omega_1^3 D_1^5} = \frac{P_2}{\rho_2 \omega_2^3 D_2^5} \tag{5.8}$$

The simple scaling relationships in equations (5.7) and (5.8) are known as the pump laws. These laws give a prediction of the change in performance occurring when altering the impeller diameter or the operating speed, and they will be used in the design of the experimental setup presented in the next chapter.

5.3 Mean line analysis

Using a one-dimensional mean line analysis it is possible to estimate the performance of a pump and to calculate the fluid properties at various stations throughout the machine. Application of the principle of conservation of angular momentum to the fluid flow through the impeller gives Euler's fundamental turbomachine equation

$$T = \dot{m}\,(R_2\,C_{t2} - R_1\,C_{t1}) \tag{5.9}$$

which relates the torque T applied at the shaft to the mass flow rate $\dot{m} = \rho Q$ and the absolute tangential velocities C_{t1} and C_{t2} at the inlet and outlet radii, R_1 and R_2, respectively. Introducing $P = T\omega$ and $U = r\omega$ gives an expression of the theoretical head

$$H = \frac{P}{\dot{m} g} = \frac{1}{g}\,(U_2\,C_{t2} - U_1\,C_{t1}) \tag{5.10}$$

According to Eq. (5.10), pressure is built up gradually when moving outwards in the impeller as both U and C_t increase. Euler's idealized theory is based on the assumption of an infinite number of blades, and consequently predicts a mean streamline in the impeller passage corresponding to the dotted line in figure 5.1.

The first exact mathematical theory that included the effect of a finite number of blades was given by Busemann in 1928. Busemann verified that, due to the finite number of blades, an incompressible, inviscid fluid will not follow the vanes. At the inlet, as indicated by the unbroken line in figure 5.1, the mean streamline is pushed towards the suction side, whereas at the outlet, it bends towards the pressure side because of the equalization of pressures that has to take place at the vane tip where streams from adjacent passages meet. The result, through a change of tangential velocities, is a decrease of the theoretical head, which is usually taken into account by defining a slip factor, see e.g. Stepanoff [112] for details.

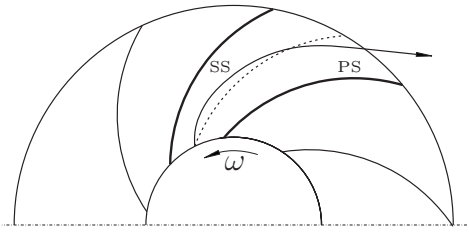

Figure 5.1: *Predicted mean streamline in an impeller passage assuming infinite (dotted line) and finite number (unbroken line) of blades, respectively.*

Based on Busemann's work, Traupel and Stanitz developed methods of computing the potential flow through an impeller, as further described by e.g. Lennemann [64]. These simple inviscid mean line methods may in many cases give a good overall prediction of the flow field, but when applied to impeller designs where viscous effects are significant, or when more details of the flow are sought for, at least a 2D flow analysis is necessary.

5.4 2D flow analysis

The flow field in a rotating impeller passage is influenced by both inviscid effects due to the rotation and viscous effects associated with the boundary layers developing at the passage walls. In order to conceptually separate these effects, first the basic inviscid forces acting on rotating flows are discussed, and then the combined effects of curvature and viscosity are included. As will become evident, this simple 2D analysis is capable of explaining many of the local flow features encountered in a centrifugal impeller.

5.4.1 Inviscid impeller flow

Consider the cross section of a rotating impeller shown in figure 5.2a. Assuming steady inviscid flow, a force balance for a fluid element in the impeller yields [48]

$$\frac{1}{\rho}\,\nabla p = -W\frac{\partial W}{\partial s}\,\vec{I}_s \;+\; \frac{W^2}{R_n}\,\vec{I}_n \;+\; \omega^2\,\vec{r} \;-\; 2\omega W\sin\sigma\,\vec{I}_n \tag{5.11}$$

where W is the relative velocity and s, n and b denote the streamwise, normal and binormal directions, respectively, $\vec{I}$ a unit vector and σ the angle between the meridional streamline and the axial direction. Eq. (5.11) shows that the pressure gradient is balanced by a sum of four forces. The first term on the RHS is the inertia force in the streamwise direction while the second term is the centrifugal force due to streamline curvature. Finally, the third and fourth terms are the centrifugal and Coriolis forces arising because the frame of reference is rotating. Written out in the streamwise and normal directions, Eq. (5.11) reads

$$\frac{1}{\rho}\frac{\partial p}{\partial s} \;=\; -\;W\frac{\partial W}{\partial s} \;+\omega^2 r\cos\beta \tag{5.12}$$

$$\frac{1}{\rho}\frac{\partial p}{\partial n} \;=\; \frac{W^2}{R_n} \qquad +\,\omega^2 r\sin\beta \;-\; 2\omega W\sin\sigma \tag{5.13}$$

where β is the angle between the streamline and the radius vector. The normal-force balance in Eq. (5.13), referred to as the Euler-n equation, may be used to explain how a pressure gradient is set up between the blades. In terms of magnitude, the radius of curvature R_n is generally very large in centrifugal impellers, and $sin\beta$ is small, why the dominating force in Eq. (5.13) is the Coriolis term. Hence the Coriolis forces are responsible for the generation of a transverse pressure gradient across the passage, which builds up high pressure on the blade pressure side. It may be noted, however, that no work is performed by the Coriolis forces as they act normal to the flow.

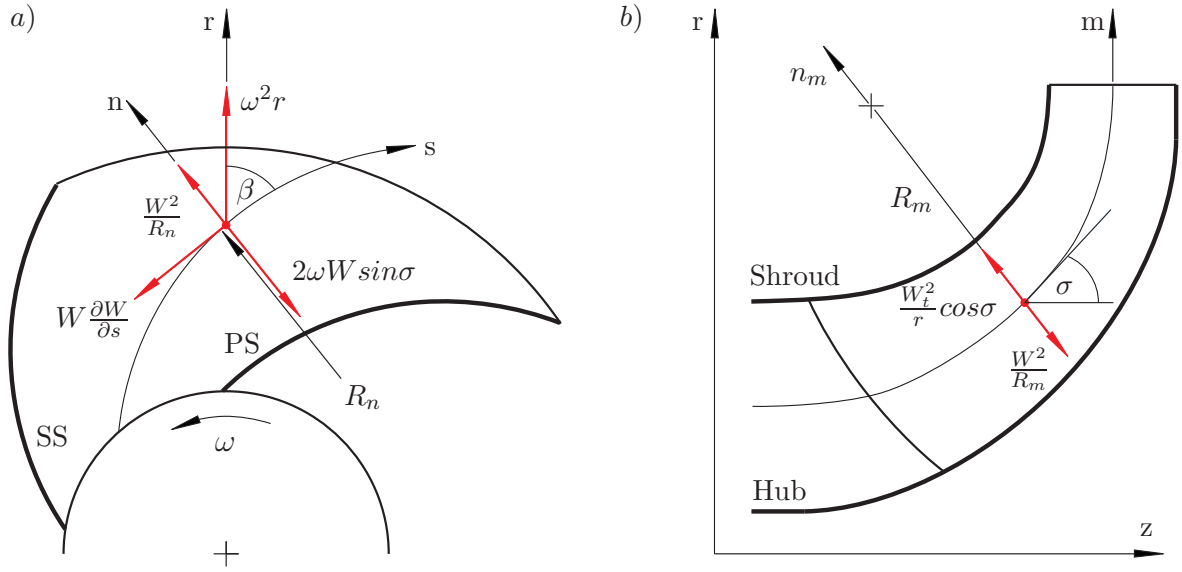

Figure 5.2: *Inviscid forces in a rotating impeller. a) blade-to-blade section b) meridional section. (After Hirsch et al. [48]).*

Considering the meridional section shown in figure 5.2b, the Euler-n equation along n_m leads to:

$$\frac{1}{\rho}\frac{\partial p}{\partial n_m} = \frac{W_t^2}{r}\cos\sigma - \frac{W^2}{R_m} \tag{5.14}$$

In the inlet region, the tangential velocity $W_t = W sin\beta$ is generally small, so the centrifugal term due to the high-curvature axial-to-radial bend dominates and leads to a pressure gradient directed from shroud to hub.

Application of the energy equation to the relative flow in the rotating impeller states that the rotary stagnation pressure

$$p^* = p + \frac{1}{2}\rho(W^2 - r^2\omega^2) \tag{5.15}$$

is preserved along a streamline, $\partial p^*/\partial s = 0$, in inviscid flow. Eq. (5.15) reduces to the familiar Bernouilli equation when traversing the passage along a circumferential line ($r\omega = const$). Therefore, in regions of low pressure the velocity is high, and vice versa. Summarizing, the inviscid balance of forces thus leads to an increase of relative velocity from pressure to suction side in the blade-to-blade surface and from hub to shroud in the meridional section. This ideal flow behavior may also be explained by the concept of the relative eddy.

The relative eddy

Pfleiderer [92] conceptually described the potential-flow pattern just derived from the Euler equations as the superposition of two flows, see figure 5.3. The first flow is the one that would develop in an enclosed passage with no throughflow, figure 5.3a. The cells of fluid rotate in a sense opposite to the impeller rotation and are termed relative eddies, a concept frequently referred to in turbomachinery. To this flow the throughflow in a non-rotating passage as seen in figure 5.3b is superposed. The relative flow resulting from the combined effects of rotation and curvature, figure 5.3c, once again shows low velocities on the pressure side and high velocities on the suction side.

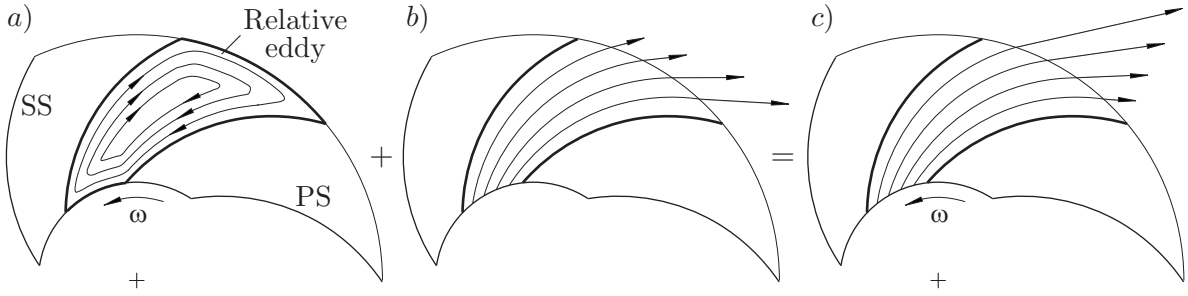

Figure 5.3: *Inviscid impeller flow seen as the superposition of a) the relative eddy arising in an impeller with no throughflow because of rotation and b) the flow arising in a non-rotating passage because of curvature.*

A potential-flow pattern dominated by the relative eddy has been reported in impeller investigations by Visser et al. [120] and Abramian and Howard [1]. Generally, however, the impeller flow is only likely to be controlled by inviscid forces in the inlet region, where viscous effects have not yet developed. Moving outwards in the passage viscous effects start to dominate and the real flow will deviate significantly from the above. The main reason is that the boundary layers developing in a long impeller passage induce a strong component of streamwise vorticity which in turn gives rise to secondary flow.

5.4.2 Secondary flow

Secondary flow refers to the velocity components that develop normal to the primary flow direction due to viscous effects. To appreciate the mechanisms behind the generation of secondary flow in a centrifugal impeller, the rate of increase of streamwise vorticity Ω_s is considered. The equation governing the development of Ω_s along a relative streamline in inviscid, incompressible flow in a rotor originates from Smith [108], but is given in a more convenient form by Hawthorne [45]:

$$\frac{\partial}{\partial s}\left[\frac{\Omega_s}{W}\right] = \frac{2}{\rho W^2}\left[\underbrace{\frac{1}{R_n}\frac{\partial p^*}{\partial b}}_{\text{Curvature}} + \underbrace{\frac{\omega}{W}\frac{\partial p^*}{\partial z}}_{\text{Rotation}}\right] \tag{5.16}$$

Eq. (5.16) expresses that streamwise vorticity will develop whenever gradients of rotary stagnation pressure p^* exists in the binormal (b) or axial directions (z). Such gradients

might result from a non-uniform inlet velocity profile or, more generally, from the reduction of p^* that occurs in the boundary layers due to viscous effects [56].

Two different mechanisms responsible for the generation of Ω_s in Eq. (5.16) are identified. Depending on the direction of the p^* gradient, vorticity is created due to either centrifugal forces caused by streamline curvature or due to Coriolis forces induced by system rotation. Thus secondary flow will develop whenever a moving fluid with a shear or boundary layer turns around a bend or is rotated about an axis. The Rossby number, $Ro = W/\omega R_n$, is a dimensionless measure of the relative strength of these two contributions. When $Ro < 1$, rotation effects dominate, and when $Ro > 1$, curvature effects dominate.

The secondary flows manifest themselves as passage vortices that may have significant influence on the flow characteristics, e.g. cause a redistribution of streamwise velocity. An important action of secondary flows is to convect low energy fluid (low p^*) from the boundary layers towards socalled stable regions, which Johnson [56] has shown to be regions of low reduced static pressure, $p_r = p - \frac{1}{2}\rho r^2\omega^2$.

It may be noted that the formation of streamwise vorticity is essentially an inviscid process once an initial boundary layer is present [13]. This allows theoretical studies of secondary flows with an inviscid model, as long as gradients of p^* are introduced on the inlet walls [14].

Secondary vortices in centrifugal impellers

The orientation and extent of the vortices set up in an impeller due to secondary flow highly depend on the mechanism that created them, which in turn depends on the impeller geometry. In a centrifugal pump impeller, typical secondary flows include the ones schematically shown in figure 5.4.

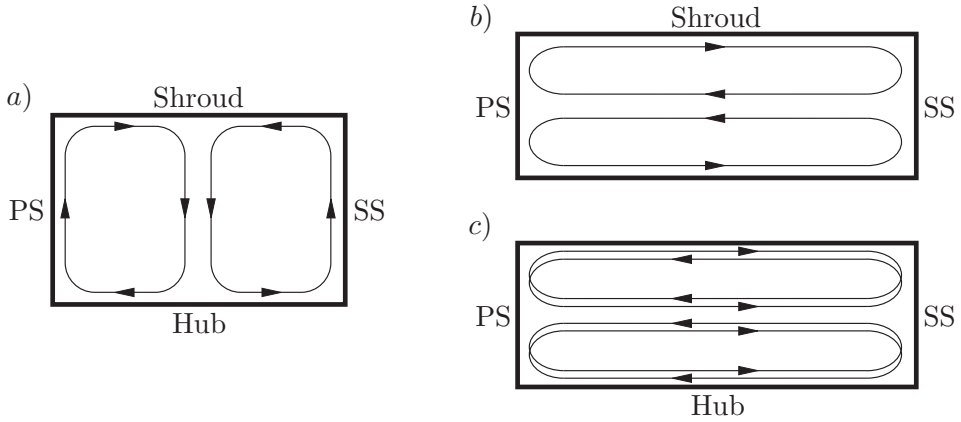

Figure 5.4: *Secondary flow generation in a centrifugal impeller. a) the axial-to-radial bend b)-c) the radial section near the impeller outlet. (After Farge and Johnson [33]).*

In the axial-to-radial bend in the inlet region, curvature effects are likely to dominate. The meridional curvature and the boundary layers developing along the blade surfaces will induce blade surface vortices that move low momentum fluid towards the shroud, figure 5.4a.

As the flow moves outwards in the radial part of the impeller, rotational effects will increase and induce passage vortices due to the axial p^* gradient in the boundary layers along the hub and shroud surfaces. This causes low energy fluid to be convected to the suction side of the passage, see figure 5.4b. Furthermore, if the centrifugal impeller has backswept blades, as in the present study, a further curvature-induced secondary flow will oppose the secondary flow due to rotation, figure 5.4c. This may cause the stable location of low momentum fluid, in the next section to be identified as a 'wake', to move towards the pressure side, depending on the Rossby number.

The similarity between the curvature-driven secondary flows in the impeller and the pair of counter-rotating vortices developing in a non-rotating curved channel should be noted. These flows have been extensively studied e.g. by Humphrey et al. [51, 52] and Taylor et al. [113] in both the laminar and turbulent flow regimes. Recently, LDV measurements in a curved channel and a curved diffuser have also been performed by Müeller [83].

5.4.3 The jet-wake model

A complex three-dimensional flow pattern develops in the impeller due to the interaction of the thickening boundary layers and the passage vortices which sweep low energy fluid towards the blade suction side. At the exit of the impeller, this motion may result in a highly distorted flow consisting of two regions, a viscous low-velocity wake region near the suction surface and a potential-flow jet region near the pressure side, see figure 5.5. This flow pattern has been reported by numerous experimental investigations (see below) and is referred to as the 'jet-wake' structure, a term introduced by Dean and Senoo [26].

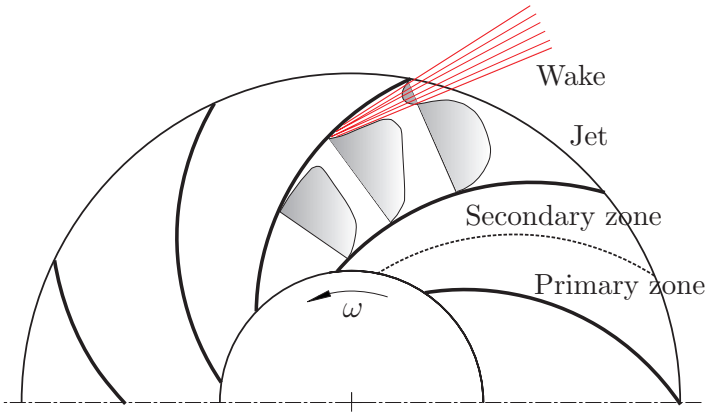

Figure 5.5: *Sketch of "jet-wake" discharge flow pattern from a rotor caused by secondary flows and boundary layer separation (after Brennen [15]).*

The non-uniformity of the discharge flow is associated with significant losses due to the mixing of the 'jet-wake' that must take place in the flow after leaving the impeller, and before entering a possible diffuser. The wake may contain up to 20% of the total passage flow [81] and is usually found near the shroud suction side corner. Its exact position is, however, influenced by a number of factors including geometry, mass flow rate, rotational speed and blade loading [57, 33]. Furthermore, the presence of inlet

distortions or boundary layer separation on the suction surface may also affect the generation and intensification of the wake [131]. At this point it is important to note that the wake region is not necessarily associated with separated flow, as the term 'wake' in some cases merely refers to slow moving fluid on the suction surface [81]. Therefore, Japikse and Baines [55] suggested to instead use the more general terms primary and secondary zones. In this frame, the distinction is made between a near-isentropic flow core and a high-loss low-momentum flow, and the regions need not correspond to any specific physical features or regions in the passage.

Most investigations observing the 'jet-wake' pattern have been concerned with centrifugal compressors. This is the case of the pioneering work by Fowler [36], Moore [81, 82] and Eckardt [31] and also later studies [56, 58, 57, 115]. Evidence of the phenomenon has, however, also been reported in pump impellers. Already the early visualization studies on a centrifugal pump carried out in 1932 by Fischer and Thoma [34], using dye injected into the passage, revealed suction side separation and wake formation under many operating conditions. Internal velocity measurements in a radial-pump impeller by Hamkins and Flack [43] showed suction side separation at low flow rates, and recent LDV investigations by Hajem et al. [41] and Akhras et al. [6] in a low-specific speed pump also revealed a clear 'jet-wake' structure.

In contrast, Abramian and Howard [1] did not detect any wake formation in their measurements in a very-low-specific-speed backswept pump impeller. This was thought to be due to the strong relative eddy associated with the high blade loading. The relative eddy (figure 5.3) forced high-energy fluid towards the suction side and suppressed separation. Visser et al. [120] also measured separation-free internal flow and demonstrated a very close comparison to potential flow. The indication that pump impellers are less inclined to develop the jet-wake structure compared to compressors may be attributed to geometrical differences. Pump impellers typically have shorter, wider passages with a smaller number of blades, and secondary flows and other viscous effects are therefore likely to be less severe than in compressor impellers.

5.5 Unsteady flow effects

The presence of time-varying, or unsteady, flow phenomena may significantly alter the flow pattern and characteristics of centrifugal impellers, especially at off-design conditions. The flow separation and wake formation mechanisms described above are often found to be unsteady. They may, however, commonly be associated with fixed locations in the impeller and for that reason Abramian and Howard [1] describe them as examples of *stationary* unsteadiness. In contrast, *periodic* unsteadiness refers to cyclic flow phenomena induced by the interaction with outside components such as a diffuser, volute or casing. Rotating stall is a predominant example of flow separation cells that change position in the impeller and thus are unsteady in both time and space. Because both stationary and rotating stall may dramatically deteriorate the performance of a pump, some of their generation mechanisms are discussed below.

It should be noted that the term stationary applies with respect to the relative frame of reference of the rotating impeller. While it is true that inherent unsteadiness of the absolute flow is required for any work transfer to the fluid to take place [25], the

relative flow in a well-designed impeller operating close to its best-efficiency point may often be considered steady.

5.5.1 Stationary stall

Stationary stall is nothing else but static flow separation zones. In addition to the curvature- and Coriolis-driven suction-side separation already discussed, a number of local stall cells may appear. At the leading edge of the impeller blade, flow entering at a high incidence angle may not be able to follow the blade and will separate equivalent to simple airfoil stall. This may result in a backflow cell extending a long distance upstream of the impeller eye. As the flow is decelerated in the diffusing impeller passage, the adverse pressure gradient may lead to local two-dimensional boundary layer separation. This type of stall should be distinguished from that associated with secondary flows and three-dimensional boundary layers [55].

5.5.2 Rotating stall

Rotating stall cells are typically found to move circumferentially from passage to passage at some fraction of the impeller speed. Figure 5.6 shows a schematic of the propagation of a stall cell in a blade cascade representing the rotor blades in an impeller [15].

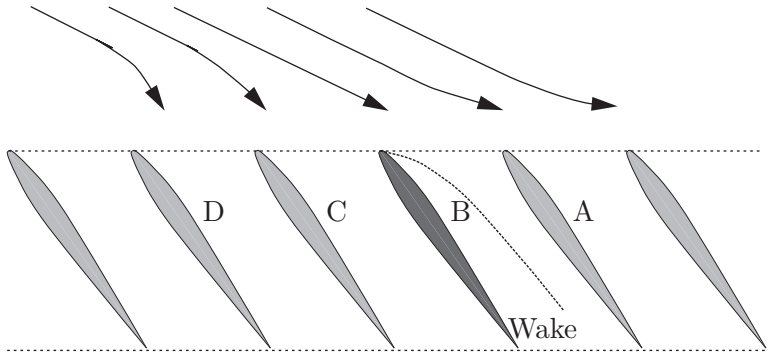

Figure 5.6: *The propagation of a stall cell in rotating stall (after Brennen [15]).*

Assume, as a starting point, that blade B is stalled due to high incidence. This generates a separated wake and thus an increased blockage to the passage between blades A and B. Therefore, the flow will tend to move towards the adjacent passages. As indicated in figure 5.6 this will lead to an increased angle of incidence on blade A, while blade C will experience a decrease and unstall. Consequently, the stall cell will move towards right in the figure, i.e. in the same direction as the rotor.

Early observations of rotating stall in a radial impeller were made by Fischer and Thoma [34]. Later, Lennemann [64] investigated the onset of rotating stall and concluded that it is closely related to the secondary flows and entry boundary layer conditions. In a detailed study, Yoshida et al. [129] detected stall cells in a 7-bladed centrifugal impeller operating with a variety of diffusers, with and without vanes.

Overall, evidence suggests that the inception of rotating stall occurs below a certain critical flow rate, is highly dependent on diffuser geometry, and propagates with a speed

of approximately 40–70% of the impeller speed. Still, much uncertainty exists on the nature of rotating stall in impellers, as most occurrences of the phenomenon have been reported in diffusers and volutes. As an example, it is still unclear whether stationary stall, or backflow, is a prerequisite step for the initiation of rotating stall [55].

5.6 Summary

In order to provide a basis for interpreting measured velocity distributions, this chapter gave a general introduction to pump flows and the theoretical analysis methods, at varying levels of complexity, used to describe them. The aim was to classify the different flow effects in an impeller according to the mechanisms that generate them.

The survey indicated that the flow field in a rotating impeller passage is influenced by both inviscid effects due to the rotation and viscous effects associated with the boundary layers developing at the passage walls. A potential-flow pattern known as the relative eddy, and observed by several investigators, was described. This was followed by a description of secondary flows and a generally accepted theory for their generation. According to this theory, also supported by experimental investigations, the flow pattern in an impeller passage may be determined by the relative strength between the effects of streamline curvature and rotation. It was, furthermore, described how the interaction of boundary layers and passage vortices may lead to the formation of a 'jet-wake' pattern at the impeller outlet or, more generally, a distinction between a primary near-isentropic zone and a secondary zone characterized by high losses. Finally, a brief overview of unsteady flow effects were given.

In conclusion, the following list summarizes the most important flow phenomena that have frequently been reported to occur in centrifugal pump impellers:

- inlet prerotation
- incidence losses
- potential relative eddy
- two- or three-dimensional boundary layers
- secondary flows
- separation of suction side boundary layers
- a division of the flow into a primary zone of near-potential flow and a low-momentum secondary zone with high losses
- 'jet-wake' structure, or other flow non-uniformity, at impeller discharge
- rotating or stationary stall inside impeller passage or in vaned diffuser

The list is not meant to be exhaustive but to serve as a tool in the analysis of measured impeller flow distributions. As suggested by the many contradicting observations found in the literature, the generation of these flow phenomena depends not only on geometry and operating conditions, but also on mutual interactions between individual flow effects. This may give rise to highly complex flow distributions, especially at off-design, as the experimental results presented in chapter 7 and 8 will indeed prove. First, however, the experimental setup will be presented.

Chapter 6

Experimental setup

This chapter describes the experimental setup of the optical flow measurements that have been performed in a centrifugal impeller in the present work. Following a brief survey of previous PIV studies in the field, the experimental objectives are stated and the characteristics of the test impeller and the flow system presented. Subsequently, the details of the PIV and LDV instrumentation are described along with the processing and analysis procedures. Finally the measurement accuracy is assessed.

6.1 Previous investigations

Ever since the visualization studies by Fischer and Thoma [34] in 1932, experimental investigations have made important contributions towards improved understanding of complex turbomachinery flows. A variety of measurement techniques have been applied to turbomachines in the strive for accurate quantitative flow descriptions. Much of the fundamental knowledge of the steady and unsteady flow phenomena reviewed in the previous chapter is based on experimental data obtained using one-point techniques such as pressure probes, hot-wire anemometry and LDV. With the emergence of the PIV technique, a powerful alternative or supplement to LDV has become available, which offers both more information and reduced acquisition times.

The last decade has shown various applications of PIV and perturbations to rotating machinery covering both pumps, fans and compressors. Wernet [121] provides an overview of the current state-of-the-art with the main emphasis on high-speed transonic compressor applications. A review of PIV investigations in compressor and pump impellers operating at low to moderate speeds is given below.

6.1.1 Stator measurements

Most reported PIV studies in compressors or pumps have focused on the flow in the stationary components of the stage, with the aim of identifying the unsteady flow structures arising from rotor-stator interactions.

The very first application of PIV to a turbomachine appears to be the work published in 1988 by Paone et al. [91]. They made velocity measurements in the blade-to-blade plane of a centrifugal compressor and described the nature of the wake from the rotating impeller blade exhausting into a vaneless diffuser. Akin and Rockwell [7] used

PIV to study the wake from a model impeller in a simulated rotating machine and its interaction with a stationary diffuser blade. They characterized flow separation and reattachment events using instantaneous streamline patterns and vorticity contours. Eisele et al. [32] used PTV (Particle Tracking Velocimetry) in a vaned diffuser and found several unsteady flow features, e.g. flow separation in the diffuser channel and a recirculating backflow from the diffuser into the impeller at part-load conditions.

Other studies measured the flow in volutes, e.g. Dong et al. [27, 28] who showed that the entire flow in the volute is pulsating, and that mean properties therefore cannot be used for estimating conditions near the exit from the impeller. They identified, among other features, a pulsating flow phenomena which depended on the location of the impeller blade relative to the tongue. Chu et al. [22, 23] later extended measurements in the same test rig to uncover the coherence between flow and noise generation events.

6.1.2 Rotor measurements

While the stator studies sketched above benefited greatly from the instantaneous PIV data as a tool to examine unsteady flow features, measurements of the instantaneous flow inside the rotating impeller passages themselves are very scarce, as only two PIV rotor investigations have been found in the open literature.

Oldenburg and Pap [89] performed PIV measurements in the impeller and in the volute of a purpose-made two dimensional centrifugal pump running at 600 rpm. Planar data were acquired in the mid-height plane at three different impeller positions relative to the tongue. The preliminary results reported in [89] showed that the relative velocity vectors did not follow the vanes at part-load and thus departed from a potential-flow pattern. Overall the measurements did, however, suffer from the commonly encountered problem in optical techniques of flare light prohibiting the evaluation of velocity vectors in large areas close to the impeller vanes.

Hayami et al. [46] and Aramaki and Hayami [8] applied PIV in a model impeller passage with the CCD camera rotating with the impeller at a rotational speed of 30 rpm. A slip-ring system was used to transfer output from the camera to a video recorder that digitized the image at a resolution of 720×480 pixels. The setup allowed the direct measurement of the relative velocity at a frame rate of 60 frames per second, corresponding to 60 cross-correlation velocity fields per revolution. This enabled Aramaki and Hayami [8] to perform a study of the spatio-temporal variation of the impeller flow and identify dominating frequencies. The sampling frequency was, however, reported somewhat too low to fully analyze the frequencies associated with rotor-stator interference between the impeller and a diffuser vane.

6.2 Experimental targets

As indicated above, the task of setting up an experiment that allows optical measurements inside the passages of an impeller poses several experimental challenges of much higher complexity than the ones encountered e.g. in the square cylinder measurements presented in Part B of this dissertation. When applying optical techniques to rotating machinery, special attention has to be paid to the development of suitable techniques for light sheet delivery, particle seeding, and image synchronization and recording. These

issues often impose design requirements that collide with the desire to undertake the measurements under true operating conditions in a realistic and flexible flow system. This dilemma is reflected in the fact that all investigations reviewed above have been undertaken either in model geometries in simulated flow systems or have been confined to the non-rotating components downstream of the impeller.

6.2.1 Objectives

In the light of the limited work done in the field of instantaneous flow descriptions in pump impellers, the main objectives of the present study were formulated as follows (as stated already in chapter 1):

- to provide detailed instantaneous data of the internal flow field in the rotating passages of a pump impeller of industrial design
- to investigate steady and unsteady flow phenomena occurring at severe off-design conditions
- to assess the accuracy of ensemble averaged PIV data by comparison with LDV data acquired under the same operating conditions
- to study the nature of the flow distortion induced by rotor-stator interaction between the impeller vanes and a stationary vaned diffuser
- to establish a detailed database that allows the evaluation of advanced numerical techniques such as Large Eddy Simulations

6.2.2 Design considerations

In order to keep the experimental setup relatively simple in this first attempt to apply the PIV technique in a rotating industrial impeller, certain demarcations have been opted for. One important choice was to perform the experiments in a dedicated compact closed-loop test rig, thereby avoiding building a full flow system comprising true rotor and stator stages, vacuum units etc, such as those typically used in industry for pump performance tests. This is a feasible choice, as the purpose of the present study is to reveal phenomenological flow structures inside the impeller passages, rather than to predict the performance of a true pump stage.

With the experimental objectives in mind, the test rig for the present experiments was designed to accommodate the following requirements:

- enable the study of phenomenological flow features inside impeller passages
- provide easy optical access
- give a stable impeller inlet velocity profile
- enable a variable flow rate at fixed operating speeds

A main concern was to keep the setup as simple as possible while still retaining the true main characteristics of the internal impeller flow.

6.3 Flow system

This section describes the characteristics of the impeller and the vaned diffuser, followed by a presentation of the test rig and the experimental operating conditions.

6.3.1 Centrifugal impeller

The impeller geometry selected for the present study was a shrouded centrifugal pump impeller of industrial design, the Grundfos CR4 [40]. It is a medium specific-speed impeller that represents the rotor part of a vertical multi-stage centrifugal pump as illustrated in Figure 6.1. Typical applications of pumps of this type, which run at a rotational speed of $n_1 = 2900$ rpm, are water transfer and circulation as well as pressure boosting in industrial process equipment. The number of stages each consisting of an impeller and a stationary return channel may be as large as 20 or more to accommodate the desired pressure rise.

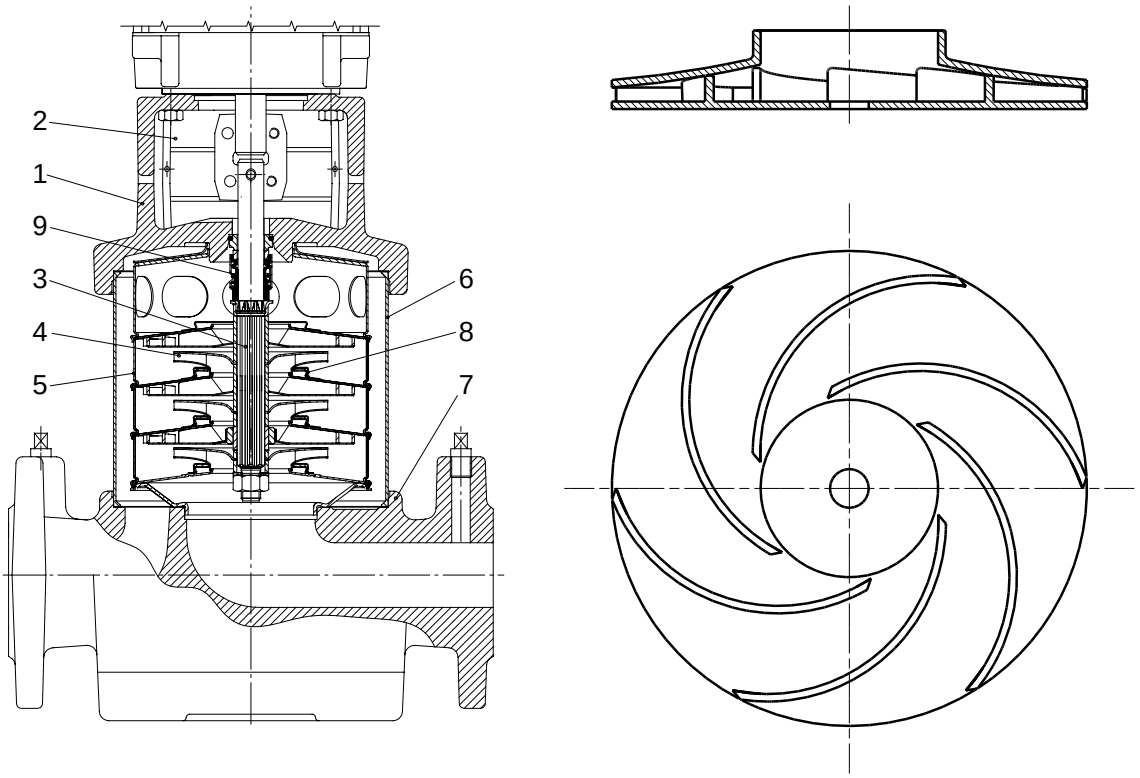

Figure 6.1: *Left: Multi-stage centrifugal pump illustrating a typical application of the CR4 impeller. Right: Meridional and plan view of the CR4 impeller. [40].*

Figure 6.1 shows the geometry of the CR4 impeller. To ease the experimental setup all dimensions were linearly scaled by a factor of 2.0 leading to an impeller diameter of $D_2 = 190$ mm but apart from this no alterations of the original CR4 geometry were made. Optical access to the impeller passages was accomplished by manufacturing the entire test impeller in perspex which was subsequently polished on all internal and external surfaces.

The main dimensions of the scaled impeller are given in Table 6.1. It consists of six simple curvature backward swept blades of constant thickness and blunt leading and trailing edges. The axial height of the impeller passages varies inversely with the radius, gradually tapering the height from 13.8 mm at the inlet to 5.8 mm at the outlet. This gives rise to a geometry which is actually three-dimensional, but nevertheless the flow is expected to be close to two-dimensional in the outer parts of the impeller.

Impeller			
Inlet diameter	D_1	77	mm
Outlet diameter	D_2	190	mm
Inlet height	b_1	13.8	mm
Outlet height	b_2	5.8	mm
Number of blades	Z_i	6	-
Blade thickness	t_i	3	mm
Inlet blade angle	β_1	19.7	°
Outlet blade angle	β_2	18.4	°

Table 6.1: *Impeller characteristics.*

6.3.2 Vaned diffuser

In order to enable a study of the major features of the flow distortion induced by rotor-stator interactions, a straight wall, constant height diffuser with 11 vanes was constructed, see figure 6.2. Vaned diffusers serve the purpose of converting dynamic pressure at the rotor exit into static pressure. Unlike the impeller, the vaned diffuser did not correspond to an actual existing geometry, but was designed according to the guidelines given by Pfleiderer and Petermann [92] to ensure a realistic flow pattern.

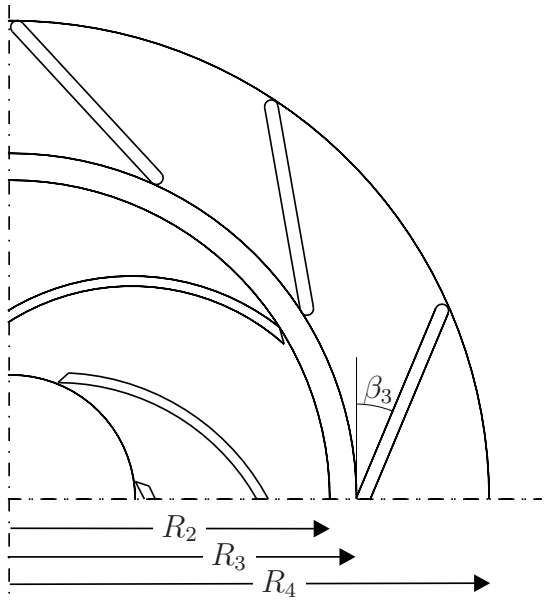

Figure 6.2: *Vaned diffuser geometry.*

Diffuser			
Inlet diameter	D_3	206	mm
Outlet diameter	D_4	285	mm
Height	b_3	7.8	mm
Number of vanes	Z_d	11	-
Blade thickness	t_d	4	mm
Inlet angle	β_3	20.0	°
R_3/R_2		1.08	-
R_4/R_2		1.50	-
R_4/R_3		1.38	-
2D diffuser angle	2θ	11.5	°
Channel length	l_d	69.8	mm
Inlet width	w_d	46.6	mm
l_d/w_d		1.50	
Area ratio	AR	1.61	-

Table 6.2: *Diffuser characteristics.*

The main characteristics of the diffuser are summarized in Table 6.2. One significant geometrical dimension is the size of the radial gap between the impeller and the stationary vane, as this greatly influences the diffuser inlet conditions and thus its performance. Several studies, e.g. Miner et al. [80], have shown that the impeller orientation may affect the velocity distribution up to about $r/R_2 = 1.20$. In practice, however, space is limited and ratios in the range 1.02–1.10 are typically used. As a compromise, R_3/R_2 was selected to 1.08. The diffuser vane inlet angle β_3 was chosen to 20° as this was the mean circumferentially averaged flow angle at the rotor exit. The axial diffuser height was set constant to the exit height of the impeller with an additional clearance of 2 mm. Like the impeller the entire diffuser was manufactured in perspex. Measurements with the diffuser installed are reported in section 7.4.

6.3.3 Test rig

Figure 6.3 shows the compact closed-loop test rig designed for the present study. It consisted of a 350 mm high, 400 mm diameter cylindrical tank with perspex casing and stainless steel top and bottom plates. The tank holds 40 liter of the working fluid which was demineralised water. The impeller was mounted on a 16 mm diameter shaft placed vertically in the tank. A 220 mm long, 84 mm diameter straight perspex pipe was used as inlet pipe to the impeller which discharged directly into the outer annulus of the cylindrical tank. Here the water rose and recirculated into the central inlet pipe.

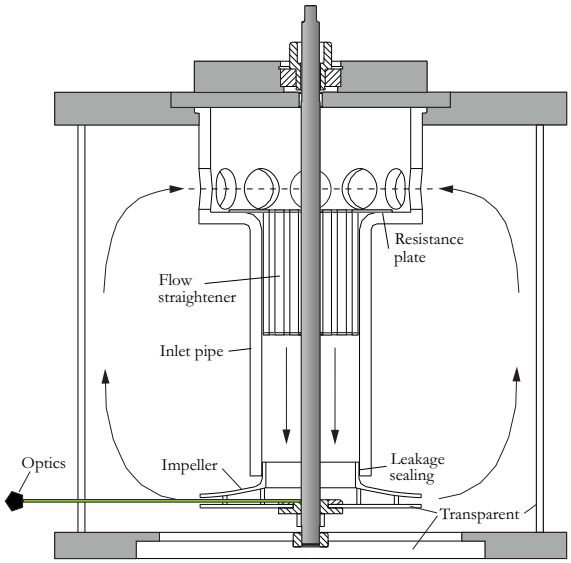

Figure 6.3: *Closed-loop test rig consisting of a 400 mm diameter cylindrical tank with the 190 mm diameter test impeller mounted in the vertical center plane. Optical access was provided from the sides as well as from beneath.*

The flow rate through the impeller was adjusted by letting the fluid pass through a resistance plate, with an array of small circular holes, which was mounted at the top of the inlet pipe. Varying the diameter of the holes from 1 to 5 mm allowed the intake area and thus the system pressure drop to be varied to achieve flow rates in

the range 15–100% of the nominal value Q_d. A flow straightener, 110 mm long and consisting of twelve 7 mm diameter pipes, was mounted in the inlet pipe in order to eliminate fluctuations from the flow and maintain stable inlet conditions to the impeller. Furthermore, a leakage sealing was installed to prevent fluid from entering the inlet pipe by flowing over the shroud plate. This effectively reduced the leakage flow, which was measured to attain a maximum value of 10% of nominal flow at shut-off conditions.

The cylindrical tank constituted a simple closed-loop test rig with optical access provided in all horizontal planes, as well as from beneath via a 260 mm diameter glass plate mounted in the bottom plate. The impeller was driven by a frequency-controlled 0.37 kW motor enabling continuously variable speed control in the range 250–900 rpm.

6.3.4 Operating conditions

To ensure flow similarity between the original CR4 and the scaled test impeller, the scaling laws and dimensionless parameters introduced in section 5.2 were used to determine the experimental operating conditions. Although Reynolds number effects are known not to dominate in turbomachines [112], it was chosen to duplicate the Reynolds number $Re = \omega D^2/\nu$ as this leads to a rotational speed that is conveniently accomplished by the motor. Since the test impeller is scaled to double size, a fixed Re means that the rotational speed should be a quarter of the original value, i.e. $n_2 = 725$ rpm.

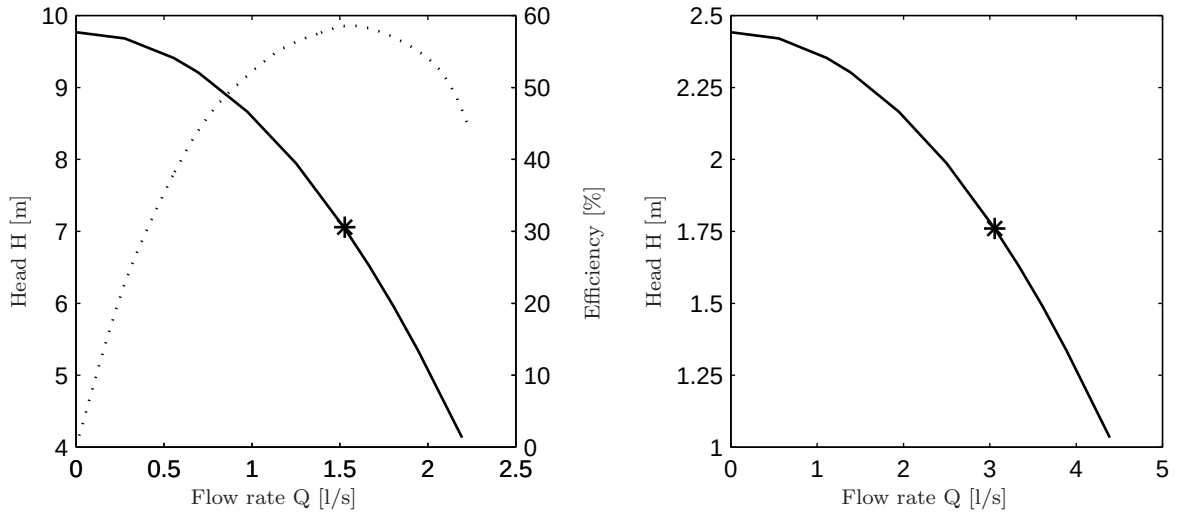

Figure 6.4: *Left: Performance (–) and efficiency (· · ·) curves for original CR4 impeller [40]. Right: Performance curve for scaled test impeller as predicted by similarity laws. Design points are marked by stars.*

The performance and efficiency curves for the original CR4 impeller as measured by Grundfos are given in figure 6.4 (left). The design point for the original CR4 impeller is the best-efficiency point given by a flow rate $Q_{d,1} = 1.5$ l/s and a head of $H_{d,1} = 7.0$ m. Defining geometric and kinematic scale factors as $k_D = 2$ and $k_n = 1/4$, respectively, equations (5.7) and (5.8) yield the volume flow rate $Q_2 = k_n k_D^3 Q_1$ and the head $H_2 = k_n^2 k_D^2 H_1$ that should be reproduced in the experiment to ensure dynamic similarity. The results are shown in figure 6.4 (right), and in table 6.3 that compares

the present design operating conditions with other impeller investigations found in the literature. Scale effects that are known to cause some deviations in the scaling of e.g. blade thicknesses, fillet radii and operating clearances were considered negligible in the present investigation.

Investigation	n	R_2	b_2	Q_d	H_d	ϕ_I	ϕ_{II}	ψ_I	Re_I	N_s
	$[rpm]$	$[mm]$	$[mm]$	$[l/s]$	$[m]$	$[-]$	$[-]$	$[-]$	$[-]$	$[-]$
Present	725	95	5.8	3.06	1.75	0.122	0.015	0.33	$1.4 \cdot 10^6$	26.3
Original CR4	2900	47.5	2.9	1.5	7.0	0.122	0.015	0.33	$1.4 \cdot 10^6$	26.3
Ubaldi et al. [116]	2000	210	40	292	57	0.126	0.048	0.29	$6.5 \cdot 10^5$	52.0
Liu et al. [68]	2910	62.7	6.2	2.72	8.9	0.058	0.012	0.48	$1.4 \cdot 10^6$	29.3
Visser et al. [120]	32	400	25	9.3	0.11	0.11	0.014	0.60	$1.1 \cdot 10^6$	16.6
Hajem et al. [41]	1200	177.3	26.7	78.2	-	0.118	0.036	0.48	$7.9 \cdot 10^6$	30.6

Table 6.3: *Comparison of impeller design parameters of the present study with those of investigations in the literature. The dimensionless parameters were defined in section 5.2.1.*

Flow in test rig container

In order to assess the flow conditions in the test rig container, preliminary LDV measurements were undertaken in the outer annulus of the tank. The curvature of the outer cylindrical wall in the test rig only allowed determination of the axial velocity component U_z.

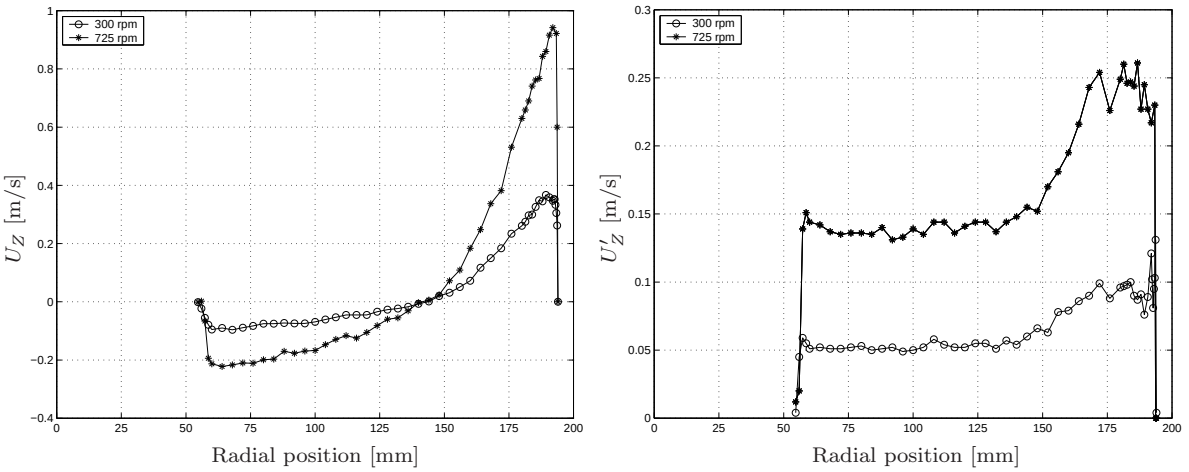

Figure 6.5: *Axial velocity profiles measured with LDV across the outer annulus of the test rig container at rotational speeds of 300 rpm and 750 rpm, respectively. Left: Mean velocity U_z. Right: RMS-velocity U'_z.*

Figure 6.5 compares axial velocity profiles obtained by traversing along a radius in the horizontal mid-plane of the test rig cylinder, at rotational speeds of 300 and 725 rpm, respectively. The number of samples were 750 at large radii, but falling off to

around 200 at small radii due to signal attenuation and imposed time limitations. In figure 6.5, both the mean velocity (left) and the RMS-velocity profiles (right) confirm the visual impression of a complex, highly fluctuating flow. U_z was non-uniform not only along a radius but also in the circumferential direction. This latter non-uniformity was due to two baffles which were installed vertically in the tank in order to reduce the swirling component of the return flow. The baffles are visible in the photograph in figure 6.3.

Because of strong optical reflections and distortions stemming from the laser beams passage of two cylindrical perspex walls, it was not possible to obtain a satisfactory Doppler-signal in the inner inlet pipe. Knowledge of the inlet flow was desirable as a means of checking the volume flow rate and to allow a detailed prescription of inlet conditions in numerical simulations of the impeller flow, but could not be obtained by this approach.

6.4 PIV setup

Figure 6.6 shows a schematic of the experimental setup used in the present study. The core components of the PIV system, i.e. the Continuum Surelite I-10 double-cavity Nd:YAG laser, the Dantec light sheet delivery system, the Kodak Megaplus ES1.0 CCD camera, and the Dantec Flowmap PIV processor, were identical to the hardware used in the square cylinder measurements, and already described in section 3.2. As PIV acquisition in rotating machinery requires the use of an accurate time base for precise laser firing and camera exposure, the timing and synchronization electronics were designed for this particular purpose. A description of the individual components in the PIV setup is given below.

6.4.1 Illumination

Particle Image Velocimetry measurements were performed inside the impeller in a horizontal (x, y)-plane positioned 2.9 mm above the plane hub, i.e. at mid passage-height at the exit, $z/b_2 = 0.5$. Furthermore, to reveal possible three-dimensional effects, a limited amount of data were acquired in two additional horizontal planes displaced 2.4 mm towards the hub and shroud, i.e. at $z/b_2 = 0.08$ and $z/b_2 = 0.92$, respectively.

Figure 6.7 shows the positions of the two 93×94 mm^2 field-of-views which were recorded at a magnification factor of $M = 0.098$. This relatively large field-of-view was chosen in order to reveal large-scale structures in the flow. The field-of-view denoted I was used at design conditions, whereas field-of-view II was used at off-design conditions where it was found advantageous to horizontally displace the camera so the image covered one and the same full passage at the impeller outlet.

The light source, the double-cavity 532 nm Nd:YAG laser, ran at 10 Hz with a pulse duration of 4–6 ns. The Q-switch delay was varied to accomplish reduced laser beam intensities between 30–60 mJ per pulse. An articulated light-guiding arm was used to direct the pulsing laser beams to the test rig where dedicated cylindrical optics produced a light sheet with a thickness of approximately 1.5 mm and a divergence angle of 15°. To enable positioning of the light sheet in the vertical direction, the sheet-forming optics were mounted on a PC-controlled 1-axis traverse unit.

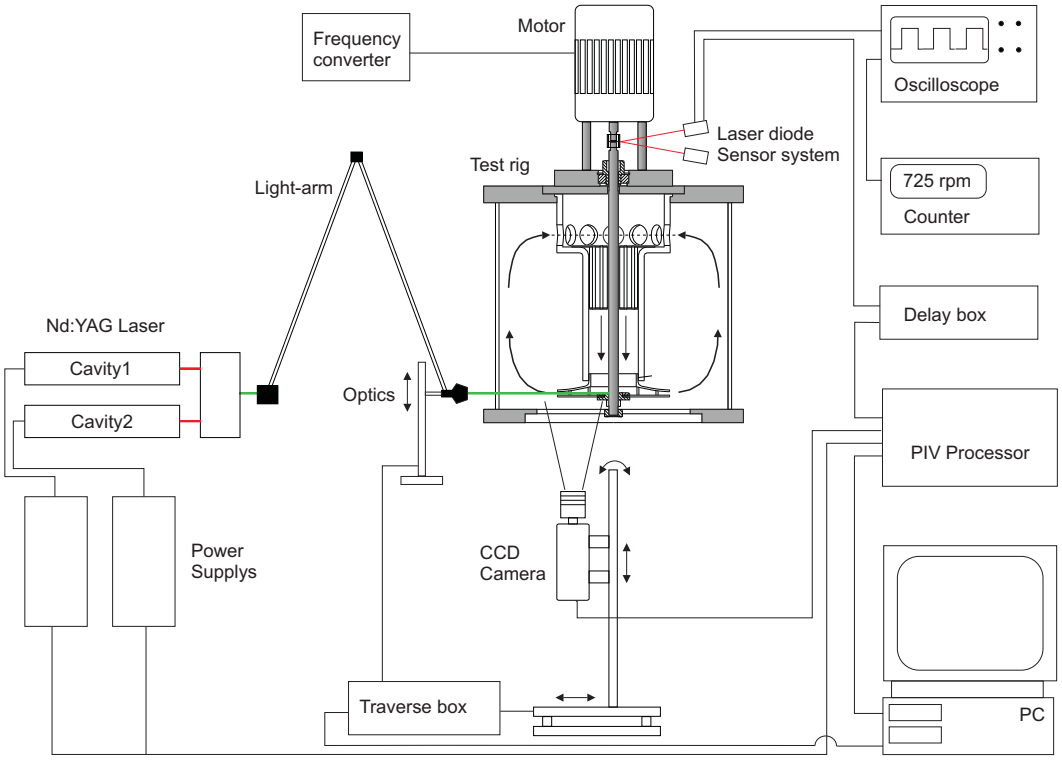

Figure 6.6: *Schematic of the experimental setup.*

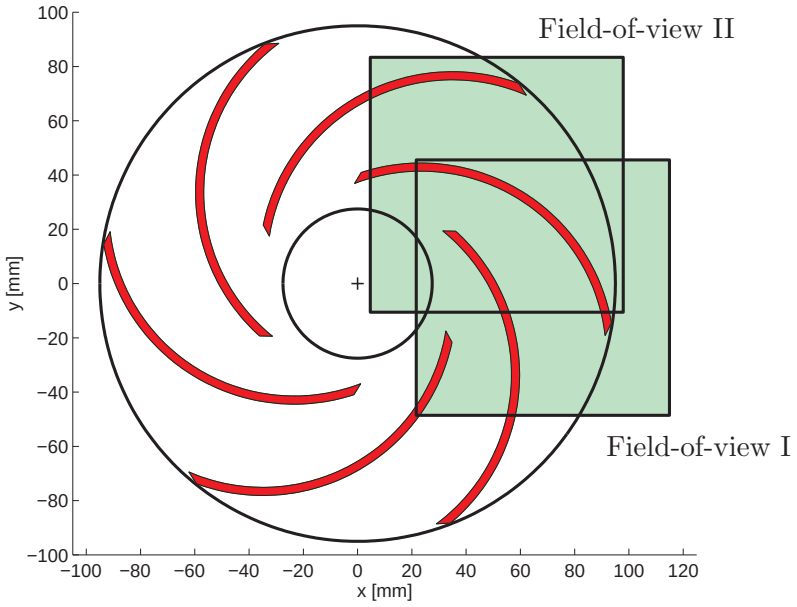

Figure 6.7: *The locations of the two 93×94 mm^2 field-of-views measured with PIV.*

6.4.2 Seeding

One major advantage of the compact closed-loop test rig is that it holds a total volume of only 40 liter and therefore easily may be flooded with seeding particles to give a homogeneous and dense seeding distribution ensuring a minimum of 5–10 particles in each interrogation region. Different seeding particles were tested. Preliminary measurements with polyamide particles were associated with the inevitable problem of flare light from the passing impeller blades obstructing the image. Therefore it was decided to use fluorescent seeding which allowed to filter out the unwanted scattered light and thus circumvented this problem entirely.

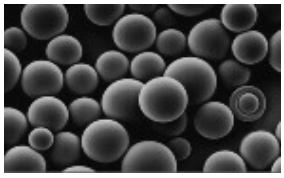

Figure 6.8: *Fluorescent polymer seeding particles containing Rhodamin B as fluorescent dye (Courtesy of Dantec).*

Figure 6.8 is a close-up of the selected Dantec fluorescent polymer particles based on melamine resin and containing Rhodamin B as fluorescent dye. The particles were of spherical shape and had a size range of 20–40 μm with a mean diameter of $d_p = 30$ μm. The green laser light excited the dye which subsequently emitted light in the orange spectrum centered around a wavelength of 590 nm. A drawback of the particles is their relatively high specific gravity of 1.5 g/cm^3. According to Eq. (2.8) of section 2.2.1, this implies that a velocity slip of 3–4% between the particles and the flow may be present. However, as the focus of the present study is on the detection of large-scale structures rather than on a study of the high-frequency turbulent fluctuations in the flow, this deficiency is found not significant.

6.4.3 Recording

Particle images were captured by the Kodak Megaplus ES1.0 1K×1K pixel cross-correlation CCD camera. The camera was mounted on a PC controlled three-axis traverse bench located below the test rig. The optical axis was carefully aligned at right angles to the laser-sheet with the camera looking at the illuminated seeding particles inside the impeller passages through the transparent hub plate. The camera was equipped with a 60 mm Nikon Micro Nikkor lens and a 550 nm optical high-pass filter which only transmitted the fluorescent light and thus prevented scattered green light from reaching the CCD sensor. In order to minimize displacement estimation errors, the numerical aperture of the recording lens was chosen so diffracted particle images covered at least 1–2 pixels on the CCD sensor. Based on M and the particle diameter d_p, this requirement imposed an f-number of $f^{\#} = 8$, as shown in figure 2.3b.

The image acquisition was synchronized with the rotational orientation of the impeller by means of a once-per-revolution pulse which was obtained by detecting the passage of a reflective target placed on the rotor shaft via a laser/photo diode sensor system, see figure 6.6. The analog output from the sensor system was converted

into a TTL logic signal that after passage of an adjustable delay circuit triggered the processor-controlled timing electronics. Whenever the trigger signal and the free running 10 Hz laser pulsing coincided within a time window of 5 ms, a double-frame image set was acquired. This allowed a large number of instantaneous samples to be obtained at fixed circumferential positions of the impeller in order to calculate ensemble averages. The once-per-revolution signal was also fed to an electronic counter to enable a direct display of the rotational speed.

The laser pulse delay Δt was carefully optimized according to the 1/4 displacement rule (Keane and Adrian [60]) and set to 150 and 110 μs for series I and II, respectively. The adjustment of Δt was a delicate trade-off between the strive for high accuracy and the strict upper bound imposed by the fact that the measuring object was moving rapidly in time. The selected inter-pulse intervals allowed the impeller to move 0.6 degrees, at the most, corresponding to 1 mm of its perimeter.

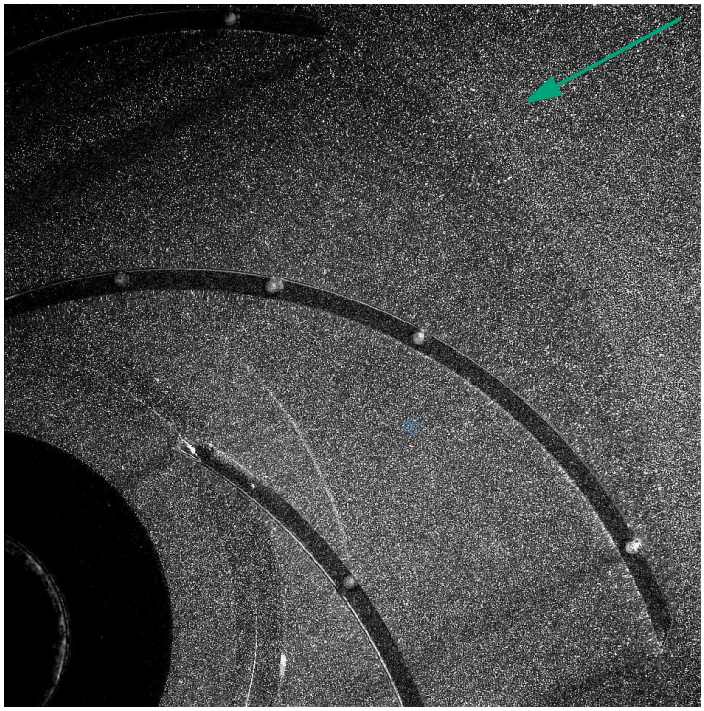

Figure 6.9: *Sample particle image of the impeller. The rotation sense is counter-clockwise. The laser sheet direction is indicated by the arrow.*

Figure 6.9 shows a sample of the particle images acquired in the impeller in field-of-view II (see figure 6.7). The rotation sense is counter-clockwise and the laser-sheet direction is from upper right to lower left as indicated by the arrow. The image shows a homogeneous and dense particle distribution and also indicates the effectiveness of the optical filter. The extent of the impeller vanes stands out very distinct with no scattered light obstructing the signal.

Efficient data acquisition was achieved by saving the raw images directly to a hard disk without an on-line evaluation of the velocity vectors. This minimized the rig run time and offered maximum flexibility in the selection of appropriate post processing parameters. The total recording time of a series of 1000 conditionally sampled images

was in the order of 20 minutes, corresponding to a mean acquisition rate of 0.8 Hz or one snapshot for every 15 impeller revolutions.

6.4.4 Image processing

The PIV images were processed into vector maps using the cross-correlation method. Due to the large dynamic range of velocity levels present in the measured field-of-view, it was found beneficial to apply the multiple pass interrogation algorithm discussed in section 2.3.4 to enhance the spatial resolution while retaining the accuracy of the velocity vectors. To accomplish this, all final image processing was performed off-line on a Pentium PC running an in-house FFT-based PIV processing code developed by Ullum [117]. However, the on-line vector processing capabilities of the commercial PIV processor were used intensively at the recording stage to optimize the quality of the acquired images.

Illumination			
light sheet source		Nd:YAG laser	
sheet thickness	Δz	1.5	mm
pulse energy		60	mJ
pulse duration		4–6	ns
pulse separation	Δt	110–150	μs
Recording			
resolution		1016×1008	px
field-of-view		93×94	mm^2
lens focal length		60	mm
numerical aperture	$f\#$	8	-
image magnification	M	0.098	-
Interrogation			
interrogation area		32×32	px
overlap		50	%
subpixel interpolator		Gaussian	-
multi-grid levels		3	-
Data set			
vectors per image	N_x x N_y	62×62	-
number of vector maps	N	1000–2000	-
storage size (images)		2–4	GB

Table 6.4: *PIV acquisition and processing parameters.*

Tests showed that applying a triple-pass $D_I = 64 \rightarrow 32 \rightarrow 32$ pixels interrogation scheme dramatically lowered the number of outliers compared to a single pass with $D_I = 32$ pixels. The Gaussian subpixel peak estimator was used as this has been shown by numerous studies, e.g. Ullum [117], to be less prone to pixel-locking effects than the parabolic interpolation scheme applied in the square cylinder measurements. Remedies to avoid pixel-locking are influential in this case because the choice of a small magnification factor M in effect limits the size of the imaged particles to a diameter below 2 pixels, equivalent to a slight under-sampling of the particle images.

The final pass interrogation regions of 32×32 pixels were overlapped 50% to yield 62×62 vectors per vector map with a distance of 1.5 mm between each vector. As indicated above, a good signal-to-noise ratio was obtained even in the close proximity of the impeller blades. Therefore, the number of spurious vectors (outliers) did not exceed 3%. This fraction was significantly lower than what was attainable with non-fluorescent seeding. Subsequently, the only validation procedure applied was a removal of the few vectors with a correlation peak signal-to-noise ratio below 1.20. These mainly corresponded to attempted velocity evaluations inside the vanes. No interpolation or data filling was applied. Table 6.4 summarizes the essential PIV parameters.

6.4.5 Data post-processing procedures

Figure 6.10 (left) shows the instantaneous velocity vector field that results from multiple pass processing of the sample image shown in figure 6.9. Because the camera frame is fixed in space, this readily obtained velocity field is the absolute velocity $\vec{C}$. The flare of the assembly screws visible in figure 6.9 was used for referencing. Although only two fix points are required, up to five points were used to determine the size and location of the recorded image relative to the impeller geometry with high accuracy. No significant image distortion effects stemming from the optical paths passage of the air-to-water interface were discerned in this calibration process.

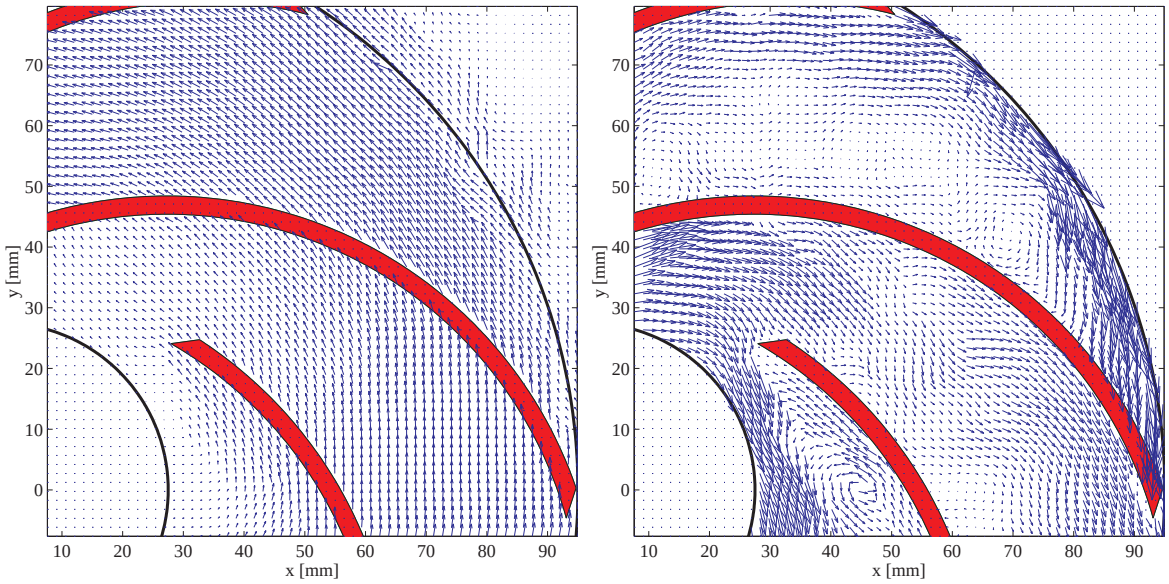

Figure 6.10: *Sample instantaneous velocity vector maps. Left: Absolute velocity $\vec{C}$. Right: Corresponding relative velocity vector map $\vec{C}$. Off-design conditions, $Q/Q_d = 0.25$.*

To allow a direct interpretation of the flow field inside the impeller passages, the relative velocity $\vec{W}$ as experienced by an observer rotating with the impeller was calculated. This is given by $\vec{W} = \vec{C} - \vec{U}$, i.e. by vectorial subtraction of the local circumferential impeller speed from the measured data. Figure 6.10 (right) shows the

instantaneous relative velocity corresponding to the absolute vector map in the left part of the figure. Apart from this transformation to the relative frame, a number of flow quantities were derived from the measured velocity field. As shown in the next chapter, these flow quantities included fluctuations, turbulent kinetic energy, out-of-plane vorticity as well as special turbomachinery quantities such as absolute and relative flow angles.

Pixel-locking effects

A report on a PIV experiment is not complete without a histogram of the displacements expressed in pixels, as this gives valuable information on the possible presence of pixel-locking in the measurements. Figure 6.11 compares the probability density distributions of evaluated displacements in the horizontal direction of the CCD chip, i.e. the C_x velocity component, resulting from a parabolic (left) and a Gaussian (right) subpixel interpolation scheme. Both histograms are based on 1000 instantaneous vector maps.

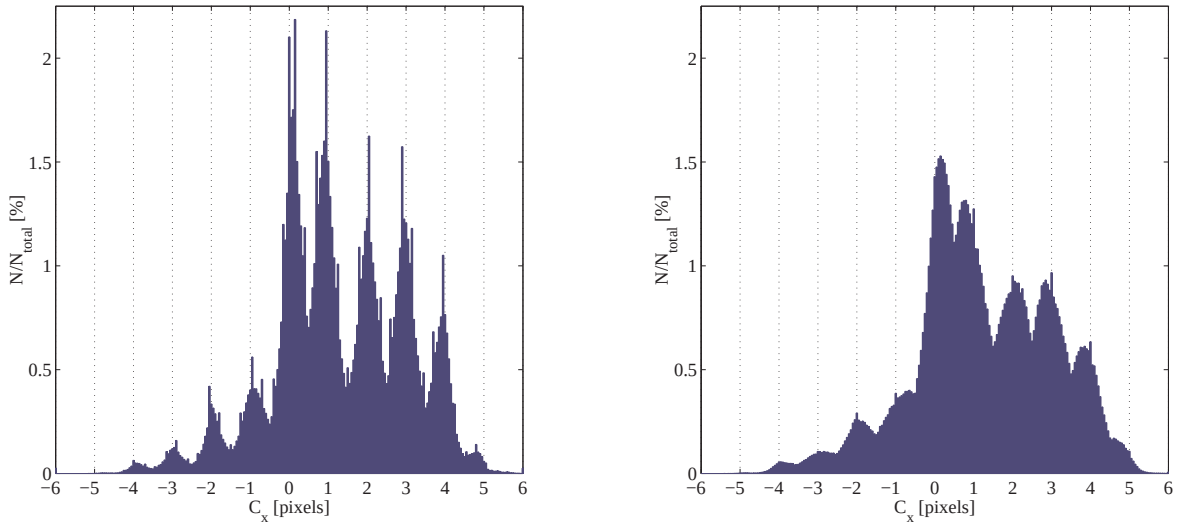

Figure 6.11: *Histograms of pixel displacements for the C_x velocity component obtained using different sub-pixel interpolations schemes. Left: Parabolic estimator. Right: Gaussian estimator. Based on $N_{total} = 3.8 \cdot 10^6$ vectors present in 1000 vector maps.*

It is evident from figure 6.11 that pronounced pixel-locking is associated with the parabolic estimator which clearly bias the displacements towards integer pixel values. The Gaussian estimator chosen for the present measurements performs considerably better but pixel-locking is not totally eliminated. This is an indispensable result of the small magnification factor chosen to cover an entire impeller passage. As discussed by Ullum [117], one impact of pixel-locking is that vortical structures in the PIV vector maps appear more polygon shaped or non-smooth than the true flow structures. The latter are, however, usually deducible from a visual inspection. Ullum [117] also showed that pixel-locking effects do not influence the flow statistics when the standard deviation of the velocity field exceeds 0.5 px.

6.5 LDV setup

As a supplement to the PIV data, a series of LDV measurements was performed in the impeller with a two-fold purpose; to provide mean data using a well-established technique to allow assessment of the PIV data accuracy, and to complement the planar PIV data with hub-to-shroud velocity profiles for the study of possible departures from two-dimensional flow behavior perpendicular to the PIV light-sheet.

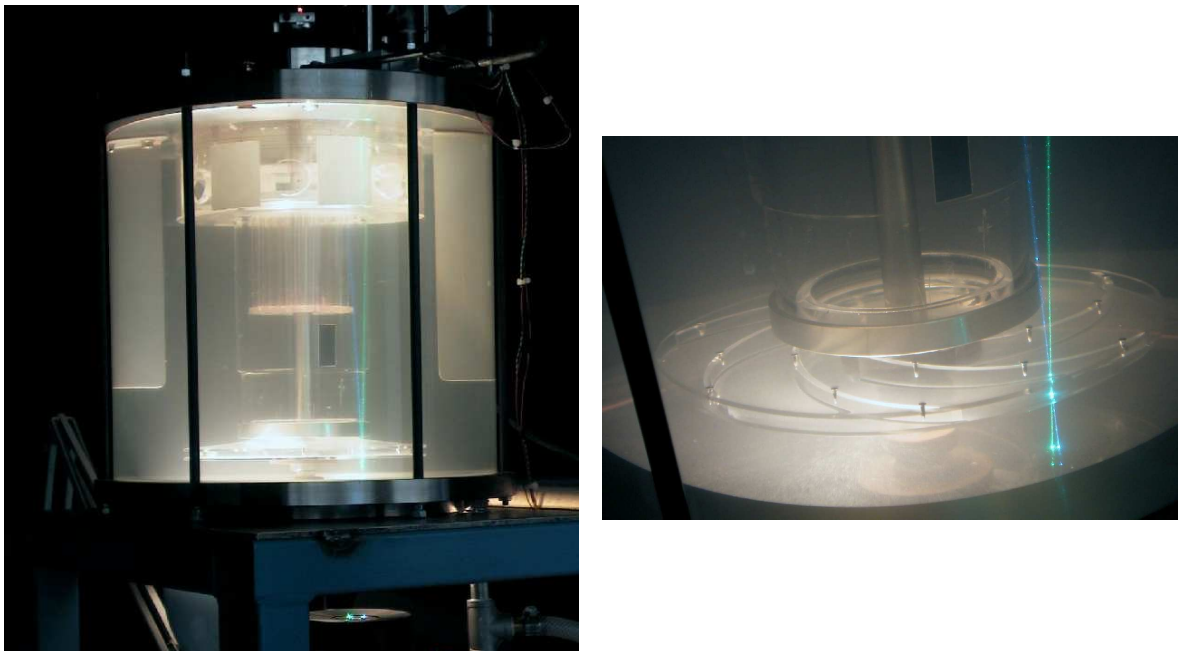

Figure 6.12: *Details of the LDV setup.*

The LDV system used in the present investigation was a two-component four-beam fiber optic system with back scatter collection optics and two Burst Spectrum Analyzers (Dantec BSA). The light source was a Coherent Innova 90 Argon-ion laser operating at wavelengths of 488 nm (blue) and 514.5 nm (green). The probe consisted of an optical transducer head of 120 mm diameter connected to the emitting optics and photo multipliers by means of optical fibers. The probe head was mounted on a three-axis PC controlled traverse bench and positioned below the test rig with the optical axis oriented in the vertical direction parallel to the impeller shaft, see figure 6.12. A 160 mm focal length front lens focused the beams at a beam separation of 20.3 mm to provide a measurement volume of 0.08 mm diameter and 1.2 mm length. The blue and green sets of fringes had a spacing of 3.8 and 4.0 μm, respectively, and allowed the simultaneous measurement of the absolute radial and tangential velocity components C_r and C_t. Directional ambiguity was eliminated by means of a Bragg cell that applied a 40 MHz frequency shift to one of each pair of beams.

The flow was seeded with neutrally buoyant polyamide seeding particles with a mean diameter of 20 μm. Signal processing was performed by two Burst Spectrum Analyzers operating in encoder enabled mode. In this mode, incoming velocity samples were sorted into 360 angular bins based on their arrival time relative to the once-per-revolution pulse from the rotor shaft. This ensured the proper assignment of phase

angle with respect to the impeller to each velocity sample. This acquisition procedure allowed free running of the LDV system and therefore was conceptually different from the conditional sampling applied in the PIV measurements.

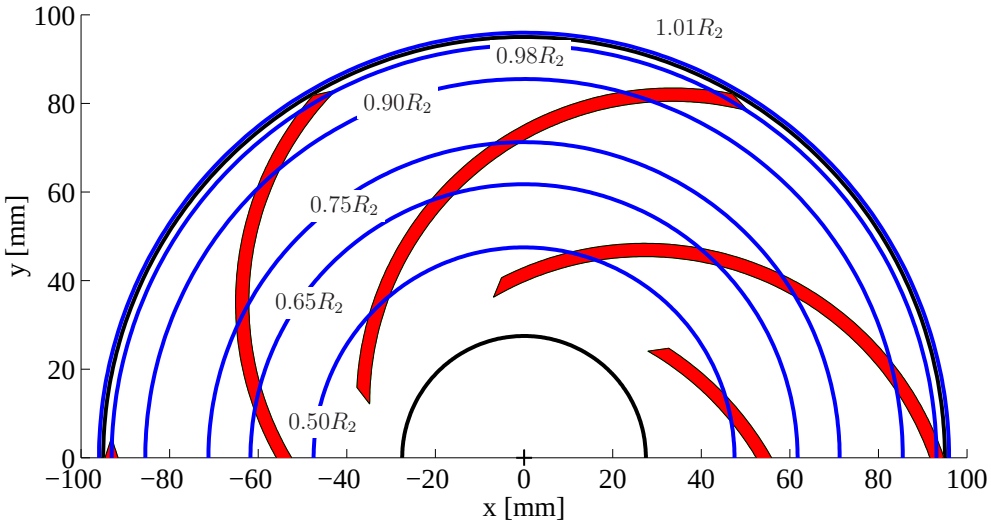

z [mm]	0.5	1.7	2.9	4.1	5.3	6.5	7.7	8.9	10.1	11.3
z/b_2	0.08	0.30	0.50	0.70	0.92	1.12	1.33	1.53	1.74	1.91
Radial station	all	all	all	all	all	1–3	1–2	1	1	1

Table 6.5: *LDV measurement stations. Radial (top) and axial positions (bottom).*

Figure 6.5 shows the LDV measurement stations. The impeller flow was surveyed at radii of $r/R_2 = \{0.50, 0.65, 0.75, 0.90, 0.98, 1.01\}$, respectively. At each radial station data were collected in 5–10 axial positions between hub and shroud depending on the local impeller height. In each measurement point, 200.000 samples of each velocity component were collected without coincidence filtering, yielding an average of 550 samples in each bin with an angular extent of 1 degree. However, on the grounds of flow congruence between the six impeller passages, the statistical sample size was raised to give an average of 3333 samples per bin. As consecutive velocity realizations were placed in different phase bins, a dead time of only 1–5 ms was imposed. Effectively, though, the sampling rate was controlled by the nature of the LDV signal and the inevitably signal loss associated with flare light and the beam passage through the hub plate. Therefore typical data rates did not exceed 100 Hz, yielding total measurement times of the order of 10 hours per series with 38 grid points. Table 6.6 summarizes the essential LDV parameters.

The position of the probe volume with respect to the measurement coordinate system was determined by first displacing the traverse bench until the intersection point of the beams coincided with the center of the lower end of the impeller shaft (which was visible through the bottom glass plate of the test rig). This unambiguously defined origo and subsequent horizontal traverses were automatically confined to the radial direction. The axial calibration was performed by placing the measurement volume at the lower surface of the hub plate. When traversing in the axial direction,

Optics	**Green (C_r)**	**Blue (C_t)**	
wavelength	514.5	488	nm
beam diameter	1.35	1.35	mm
beam expansion ratio	1.0	1.0	-
beam spacing	20.3	20.3	mm
lens focal length	160	160	mm
Measurement volume			
Diameter	0.078	0.074	mm
Length	1.22	1.16	mm
Fringe spacing	3.8	4.0	μm
Number of fringes	19	19	-
BSA setup			
filter center	0	3.84	m/s
filter span	8.11	7.69	m/s
record length	10.7	10.7	μs
PM high voltage	1200	1104	V
signal gain	30	30	dB
Data collection			
velocity samples	200.000	200.000	per point
angular bins	360	360	-
velocity samples	550	550	per bin
dead time	1–5	1–5	ms

Table 6.6: *LDV parameters.*

one had to compensate for the fact that the actual displacement of the beams in the test rig was a factor of 1.33 larger than specified due to the change in refractive index at the air-water interface.

6.6 Measurement accuracy

General experimental uncertainties included variations in the impeller speed, estimated to 1.5%, and an uncertainty in the flow rate specification of about 5% due to the lack of a dedicated flow meter in the test rig. The reproducibility of Q between measurement series was, however, much better. Due to friction losses, temperature rises were observed in the small volume of water in the test rig after long run times. This did not affect the 20 minutes PIV series, but led to slight Reynolds number changes in the LDV measurements.

6.6.1 PIV measurements

In ensemble averaged PIV data based on a large number of instantaneous samples, the measurement error is composed of both statistical and systematic errors [121]:

$$s^2 = \underbrace{\sigma_{TI}^2 + \sigma_D^2}_{\text{statistical}} + \underbrace{\sigma_{Syn}^2 + \sigma_{Lag}^2}_{\text{systematic}} \tag{6.1}$$

The standard deviation s contains the effects of flow turbulence σ_{TI}, the measurement errors of the PIV technique σ_D, synchronization errors associated with the once-per-revolution signal σ_{Syn}, and any particle lag effects σ_{Lag}. As discussed in section 2.3.3, the errors inherent in the instantaneous digital PIV velocity estimates themselves were estimated by Westerweel [124] to be of the order of 1% of full scale. Despite a slight variation in the impeller speed read on the counter, the image synchronization worked very well with no noticeable fluctuations in the observed impeller position in a sequence of conditionally sampled images. Because of the large density difference between the fluorescent particles and the fluid, some particle lag effects may be present, as already discussed.

A typical value of the standard deviation computed from the ensemble average of 1000 instantaneous PIV measurements was $C_{x,rms} = 0.3\ m/s$. According to Eq. (2.27), this leads to an accuracy of 1.8% and 1.3% on the mean and fluctuating components of velocity, respectively, stated at a confidence level of 95%.

6.6.2 LDV measurements

To avoid velocity bias effects, bin averages were computed using the residence time as weighting factor [16]. The uncertainty in probe volume positioning in the radial and axial directions was estimated to ±0.2 mm. Since velocity gradients are present in the flow, a misplaced probe volume will measure the incorrect velocity. This gives rise to a spatial uncertainty on top of the uncertainty associated with the LDV technique itself. Furthermore, with the present optical setup, each velocity realization is associated with a spatial averaging over the measurement volume length of 1.2 mm. As this occupies a

significant proportion of the impeller height, velocity bias effects are likely to occur. A shorter probe volume would require a larger beam spacing, a front lens with a shorter focal length or the addition of a beam expander. However, a dramatic reduction of the measurement volume length would result only from radical changes of the optical setup.

6.7 Summary

The experimental setup used for PIV and LDV measurements inside the rotating passages of an industrial medium specific-speed centrifugal pump impeller was presented. The PIV and LDV instrumentation were described along with the synchronization, acquisition and processing procedures applied. Finally, the experimental uncertainties were assessed. The next chapter presents the PIV results, whereas a quantitative comparison with LDV and LES results is performed in chapter 8.

Chapter 7

Results

In this and the next chapter the results from PIV and LDV measurements in the internal passages of a centrifugal pump impeller are presented. Instantaneous whole-field PIV data and ensemble averages based on large sample numbers are analyzed for the purpose of identifying steady and unsteady flow structures. A qualitative study of the cyclic flow features associated with rotor-stator interaction between the rotating impeller blades and a stationary vaned diffuser blade is also performed.

7.1 Measurement program

In order to comprehend the effects on the flow characteristics of varying the flow rate and thus the load on the impeller, an extensive PIV measurement program was undertaken. As shown in Table 7.1, PIV data were recorded at four different flow rates in the range $Q/Q_d = 0.15$–1.0 for the impeller setup without vaned diffuser. To investigate rotor-stator interaction flow distortions, the cases denoted I and II were also studied with the setup of installed vaned diffuser. All data were acquired at a constant rotational speed of $n = 725$ rpm, or $\sim$12 revolutions per second.

Series	Q/Q_d	Axial position	$z\,[mm]$	z/b_2	Passage	$\Delta t\,[\mu s]$	Data set	LDV	LES [18]
I	1.0	Mid-height	2.9	0.5	A	150	1000	×	×
	0.5	Mid-height	2.9	0.5	A/B	135	$2 \cdot 1000$		
II	0.25	Mid-height	2.9	0.5	A/B	110	$2 \cdot 1000$	×	×
	0.25	Near hub	0.5	0.08	A/B	110	$2 \cdot 1000$	×	×
	0.25	Near shroud	5.3	0.92	A/B	110	$2 \cdot 1000$	×	×
	0.15	Mid-height	2.9	0.5	A/B	125	$2 \cdot 1000$		

Table 7.1: *PIV measurement program for impeller setup without vaned diffuser. The presentation focuses on series I and II obtained at design and quarter-load conditions, respectively. These two cases were also measured with the setup of installed vaned diffuser. All data were obtained at $n = 725$ rpm.*

Table 7.1 states the axial height z of the illumination plane relative to the inner side of the hub plate, the laser inter-pulse delay Δt and the size of the conditionally sampled PIV data sets. The column denoted 'Passage' shows whether data have been

acquired in one (A) or two (A/B) passages, respectively, the latter due to an observed loss of flow congruence between adjacent passages at off-design conditions. This feature will be explained in detail later.

Although the PIV data base comprises vector maps acquired at 4 different flow rates, the presentation will focus on the design flow condition ($Q/Q_d = 1.0$) and the quarter-load condition ($Q/Q_d = 0.25$), as the observations at these two operating points have been found to represent well the qualitative flow features associated with design and severe off-design conditions, respectively. For the same reason, the LDV measurements and the LES performed by Byskov [18] were confined to these two operating points, as indicated in Table 7.1.

The presentation is organized as follows. In order to reveal the global characteristics of the flow, this chapter first presents PIV whole-field data acquired in the impeller mid-height plane, $z/b_2 = 0.5$. Both instantaneous samples and ensemble averages based on 1000 PIV vector maps are used in this analysis, which also includes a brief study of rotor-stator interaction mechanisms. Following this qualitative investigation, a detailed quantitative analysis of the impeller flow is presented in the next chapter. Blade-to-blade distributions of selected flow quantities are extracted from the PIV data and compared with LDV data at different radial and axial stations. If not explicitly stated otherwise, the presented plots are based on ensemble averaged PIV data.

7.2 Design load conditions

Figure 7.1a shows a sample instantaneous PIV velocity vector map acquired at the design flow rate Q_d in field-of-view I (see figure 6.7). The vector map shows the relative velocity $\vec{W} = \vec{C} - \vec{U}$ inside the rotating impeller passages and the absolute velocity $\vec{C}$ outside the impeller. The impeller rotation sense is counter-clockwise. A corresponding ensemble average of 1000 instantaneous realizations, color-coded with the local speed, is shown in figure 7.1b.

It is seen from both vector maps in figure 7.1 that the field of relative velocity follows the curvature of the blades in the predominant parts of the impeller passage, and that the flow increases along both suction and pressure sides with no significant separation. Only a careful investigation of the vector maps reveals that the blunt leading edge of the blade slightly perturbs the flow and creates a narrow recirculation zone extending a few millimeters downstream on the suction side. More important, a low-velocity zone on the blade pressure side develops, extending about two-thirds downstream the blade.

This low-velocity zone is also evident from the contour plot of the relative speed $|\langle\vec{W}\rangle|$ shown in figure 7.2. The fact that high-momentum fluid is displaced towards the suction side in the inlet section is in accordance with potential theory. It also indicates that the meridional curvature associated with the axial-to-radial entry bend dominates over rotational effects in the inlet. However, as the fluid moves towards larger radii, the Coriolis force gains strength and pushes the fluid in the opposite direction towards the pressure side. As a result, $|\langle\vec{W}\rangle|$ on the pressure side increases in the outer parts of the passage where the blade pressure surface is no more covered by the suction surface of the adjacent blade. The result is a uniform outlet velocity distribution free from distortions or wake effects.

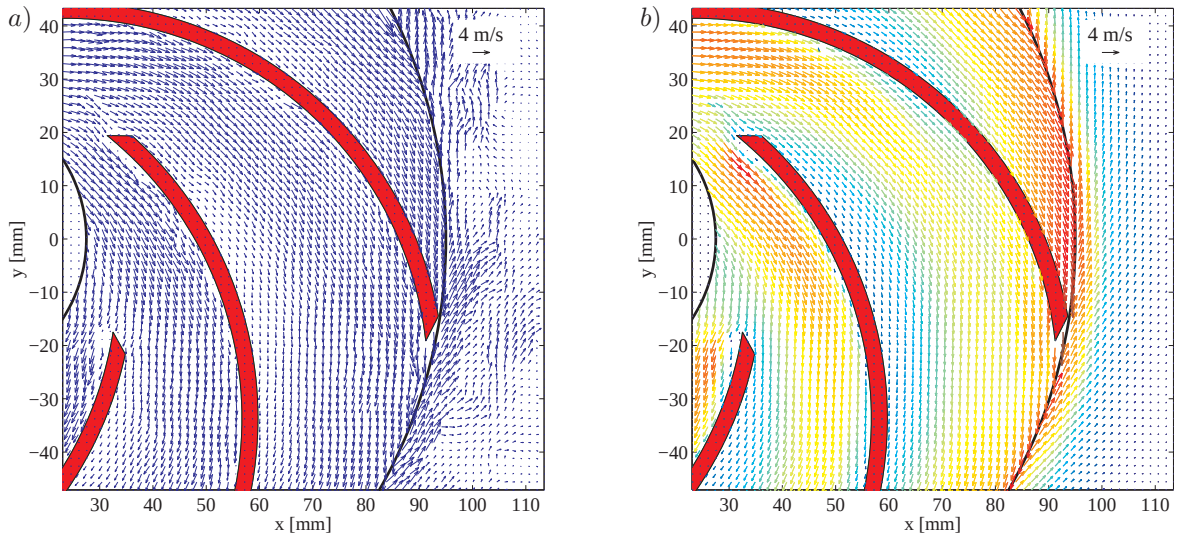

Figure 7.1: *Vector maps showing the relative velocity $\vec{W}$ inside the impeller passages and the absolute velocity $\vec{C}$ outside the impeller. a) Sample instantaneous snapshot b) Ensemble average of 1000 instantaneous samples color-coded with the local speed. ($Q/Q_d = 1.0$).*

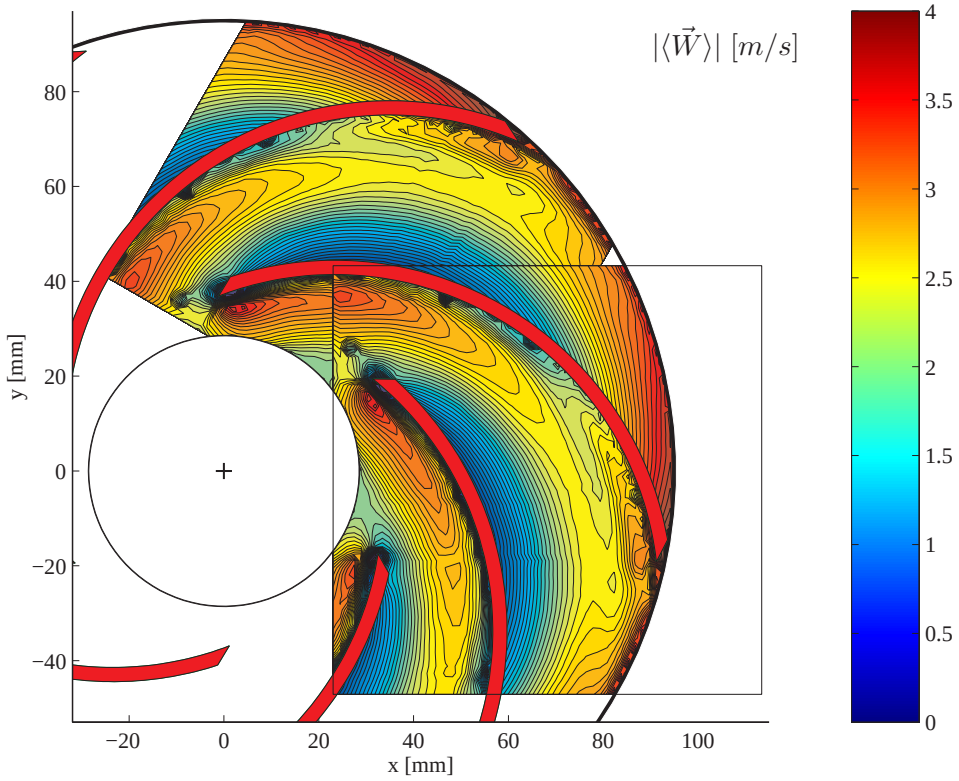

Figure 7.2: *Ensemble averaged relative speed $|\langle\vec{W}\rangle|$. A copy of the measured data has been rotated 60 degrees with respect to the rotation axis to demonstrate the flow congruence between adjacent passages. ($Q/Q_d = 1.0$).*

As discussed in section 5.4.2, a measure of the relative strength between rotational and curvature effects is the Rossby number Ro. In the blade-to-blade plane, this is given by $Ro = \langle\vec{W}\rangle/\omega R_b$ where $R_b = 70\ mm$ is the constant curvature radius of the blades. The highest Ro occurs at the inlet and attains a value of about 0.8, falling to $Ro \approx 0.6$ in the central parts of the passage. This indicates that even when curvature effects are largest, the flow in the blade-to-blade plane is mostly dominated by rotational effects, as was also the case in the impeller studied by Abramian and Howard [1].

In figure 7.2, a replicate of the measured data has been rotated 60 degrees with respect to the rotation axis to illustrate the flow congruence that clearly exists between adjacent passages at design operating conditions. This supports the expectation that data acquired in one passage represent the flow in all six passages. A definitive confirmation of this is given by the vector plot of the bin-resolved LDV mean velocity field shown in figure 7.3 after transformation into the relative frame. The LDV velocity vectors at the inner radial station of $r/R_2 = 0.50$ should be disregarded, since excessive reflections obscured the determination of the radial velocity component C_r at this station. The mean fields at the other radii, however, underline the picture of a well-behaved relative flow exhibiting circumferential uniformity at the outlet.

The angle between the relative velocity vector and the circumferential direction is defined as the relative flow angle $\beta = atan(W_r/W_t)$. Based on this, a quantitative measure of the extent to which the flow follows the blade curvature is the deviation angle $\langle\Delta\beta\rangle = \langle\beta\rangle - \beta_2$ between the relative velocity vector and the exit blade angle $\beta_2 = 18.4°$. Figure 7.4 shows a contour plot of $\langle\Delta\beta\rangle$, with a value of zero signifying a perfect flow guidance. Several local flow features are highlighted in figure 7.4. The relatively high positive values of $\langle\Delta\beta\rangle$ concentrated near the blade suction side at the inlet indicate a somewhat prerotated inlet flow, i.e. the existence of a swirl component in the inlet pipe flow generated by the rotation of the impeller. Furthermore, the distortion created by the impingement of the flow on the blunt leading edge is visible. A zero contour line is seen to extend from the blade trailing edge across the passage to the preceding blade pressure surface. This zero contour line defines the boundary between the inner part of the passage, which may be characterized as a true 'channel', and the outer part where velocity slip effects become effective due to the unloading of the blade. Overall, however, only modest deviation angles are present at design load.

7.2.1 Turbulent fluctuations

To highlight the turbulent fluctuations present in the flow, a sample instantaneous deviation $\vec{C} - \langle\vec{C}\rangle$ from the ensemble average is given in figure 7.5a. It should be noted that these fluctuating velocities also represent those of the relative field, i.e. $\vec{W} - \langle\vec{W}\rangle$. A quantitative measure of these random unsteady velocity fluctuations is the measured portion k_{2D} of the turbulent kinetic energy k, defined as the mean deviation of instantaneous data from the ensemble-averaged results

$$k_{2D} = \frac{1}{2}\left[\langle C_x'^2\rangle + \langle C_y'^2\rangle\right] \tag{7.1}$$

where the primes denote the RMS of the velocity fluctuations, and C_x and C_y the measured planar velocity components. However, this quantity does not account for the span-wise velocity fluctuations, not measured.

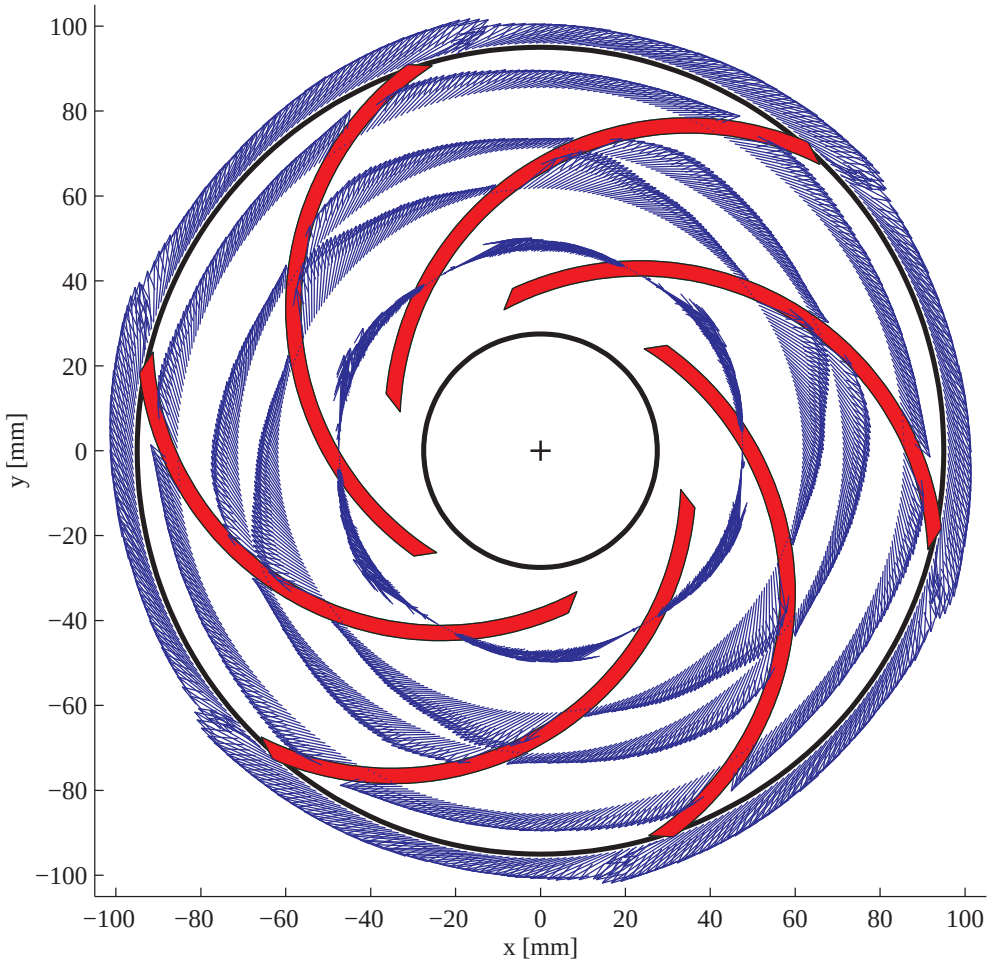

Figure 7.3: *Vector plot of the relative velocity $\langle \vec{W} \rangle$ measured with LDV at radial stations of $r/R_2 = \{0.50, 0.65, 0.75, 0.90, 1.01\}$. $(Q/Q_d = 1.0)$.*

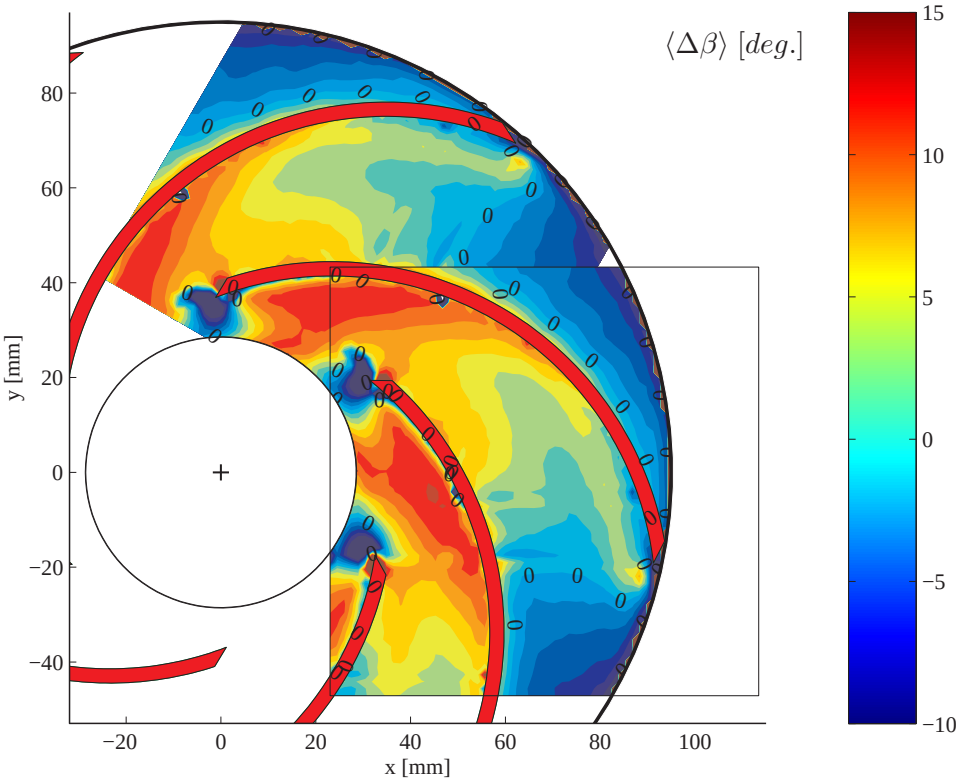

Figure 7.4: *Contour plot of the ensemble averaged deviation angle* $\langle \Delta\beta \rangle = \langle \beta \rangle - \beta_2$ *between the relative flow angle and the outlet blade angle* $\beta_2 = 18.4°$. *A copy of the measured data has been rotated 60 degrees with respect to the rotation axis to demonstrate the flow congruence between adjacent passages.* $(Q/Q_d = 1.0)$.

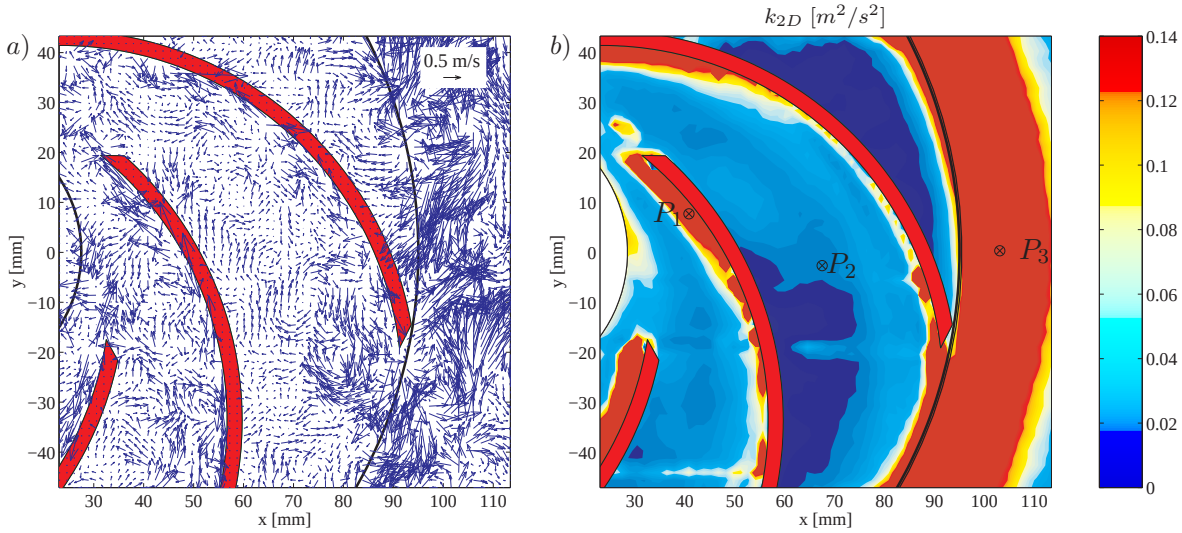

Figure 7.5: *a) Sample instantaneous deviation* $\vec{C} - \langle \vec{C} \rangle$ *from ensemble average b) Contour plot of the measured portion* k_{2D} *of the turbulent kinetic energy.* $(Q/Q_d = 1.0)$.

A contour plot of k_{2D} is given in figure 7.5 and demonstrates an even distribution of turbulent kinetic energy inside the passage. Local high levels of turbulence are confined to near-wall areas along the blade suction side, coinciding with positions of high relative velocity. Outside the impeller, elevated levels exist due to the mixing-out of the impeller discharge flow, but the large fluctuations may also be partly attributed to three-dimensional effects causing the seeding particles to move in the direction perpendicular to the laser light-sheet.

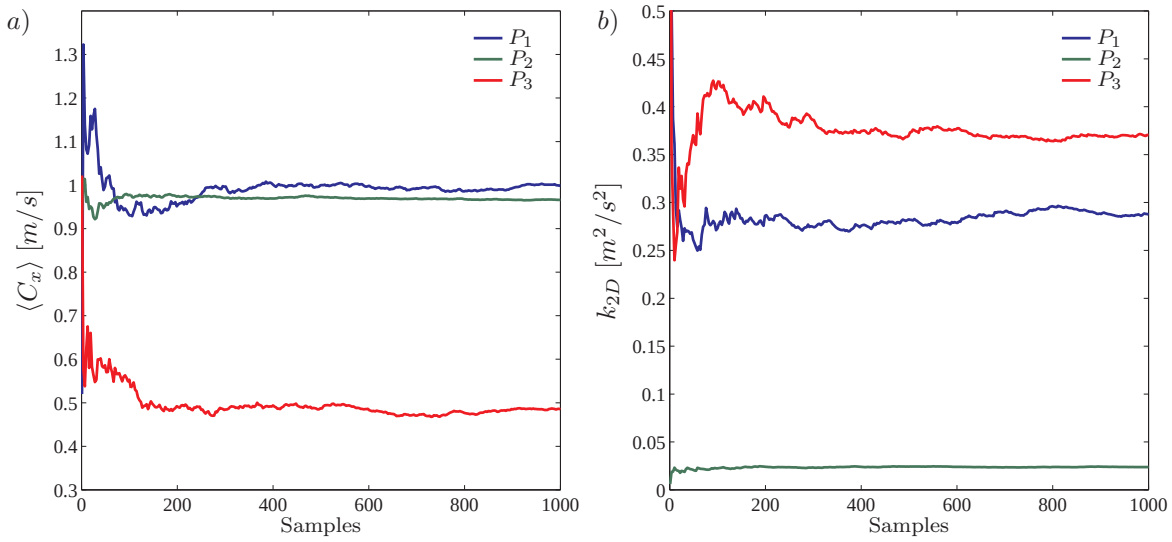

Figure 7.6: *Convergence history of the first and second order moments in the three sample grid points P_1, P_2 and P_3 marked in figure 7.5b. a) Horizontal velocity component $\langle C_x \rangle$ b) Turbulent kinetic energy k_{2D}. ($Q/Q_d = 1.0$).*

To demonstrate the level of convergence obtained by basing the ensemble averages on a total of 1000 instantaneous samples, figure 7.6 shows the convergence history of the first and second order moments of the measured data in three different grid points in the field-of-view. These points are marked in figure 7.5b. The first point, P_1, is situated in the high-turbulent zone behind the leading edge on the blade suction side, the second, P_2, in the low-turbulent passage center, and the third, P_3, in the mixing-region downstream of the impeller. Figure 7.6 shows the effect of including more samples in the calculation of $\langle C_x \rangle$ and k_{2D}, respectively. The graphs clearly demonstrate that the first and second order moments, at a sample size of $N = 1000$, are well-converged even in the extreme cases of high-turbulent regions.

Based on k_{2D}, a turbulence intensity Tu may be calculated from $Tu = \sqrt{k_{2D}}/U_2$ where U_2 is the impeller speed at the outlet. Values of Tu reach a maximum of 6% near the suction side, but are otherwise much lower, 2–3%. As noted by Ubaldi et al. [116] from similar observations in an unshrouded impeller, this low level of turbulence indicates the persistence of an inviscid potential flow core through the impeller passage at design conditions. An alternative definition of the turbulence intensity is $Tu_{local} = \sqrt{k_{2D}}/|\langle \vec{W} \rangle|$, which has been frequently used in the literature, see e.g. [11, 1, 47]. As this definition is normalized by the local mean speed, it may lead to excessively large values in low-speed regions. Hence, caution should be taken when comparing the present observations with results from the literature.

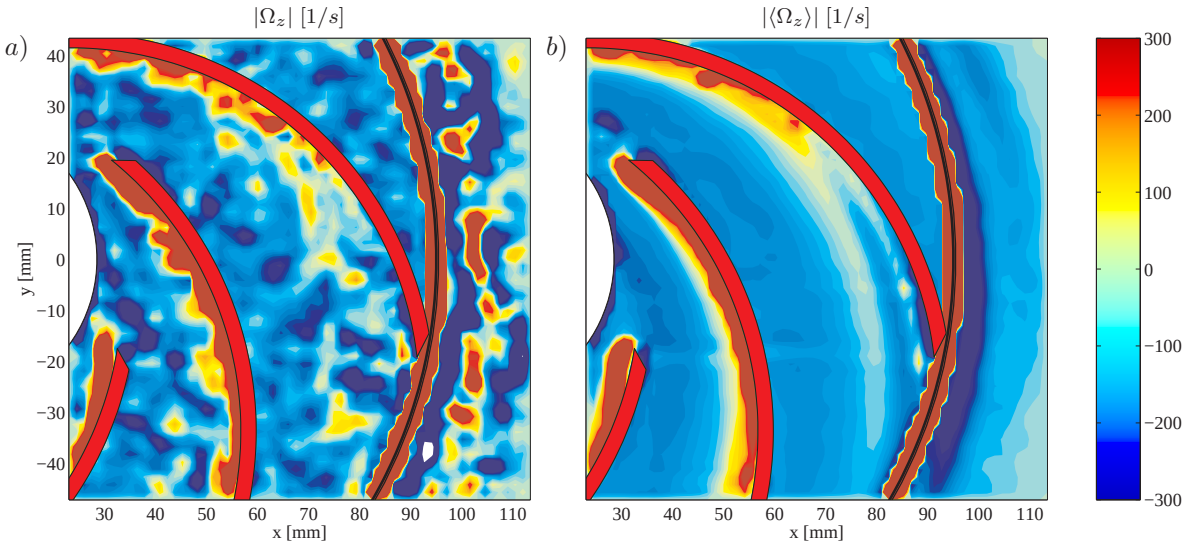

Figure 7.7: *Contour plots of the magnitude $|\Omega_z|$ of the out-of-plane vorticity component. a) Instantaneous sample b) Ensemble average. ($Q/Q_d = 1.0$).*

Contour plots of the magnitude of the out-of-plane vorticity component Ω_z are shown in figure 7.7. The vorticity was calculated by differentiating the relative velocity field using the circulation method described in section 2.4.1. A comparison of the sample instantaneous $|\Omega_z|$ distribution in figure 7.7a and the ensemble average in figure 7.7b illustrates the type of valuable flow information that may be deduced from instantaneous PIV data. Although the ensemble average looks very smooth, the instantaneous sample suggests the existence of cells of vorticity migrating through the impeller, predominantly in the vicinity of the blade suction surface. It should, however, also be noted that instantaneous vorticity fields are very sensitive to distortions due to the differentiation involved.

In summary, the measurements at design load show a well-behaved, predominantly vane congruent flow with no separation occurring and no significant distortions of the outlet velocity profile. A distinct flow congruence between all six passages was observed.

7.3 Quarter-load conditions

A main objective of the present work was to investigate the characteristics of the complex flow pattern that develops when operating a centrifugal impeller far from its design point. Reducing the flow rate to only a quarter of the nominal value represents an example of severe off-design conditions. Even though it may be argued that a pump should only quite exceptionally operate under such extreme conditions, an investigation at $0.25Q_d$ is valuable as it accentuates the dramatic flow changes that occur below a critical flow rate. A better understanding of the physics governing the internal flow at reduced flow rates is a requisite step towards a broadening of the efficient operating range.

Figure 7.8a shows a snapshot of the flow measured in field-of-view II at a flow rate of $0.25Q_d$. The ensemble average based on 1000 vector maps is presented in

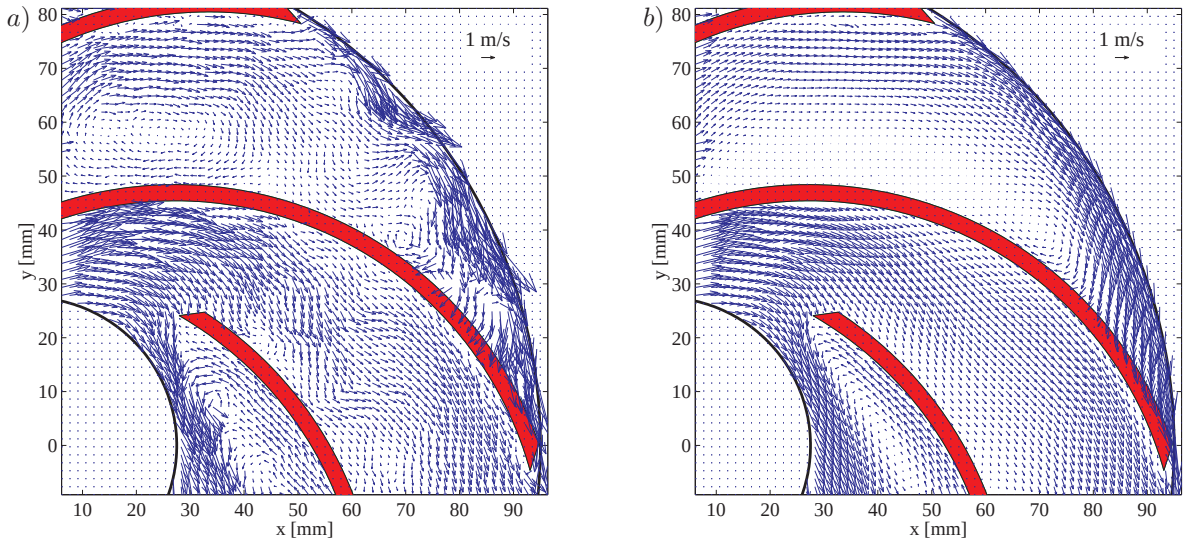

Figure 7.8: *Vector maps of the relative velocity $\vec{W}$. a) Sample instantaneous snapshot b) Ensemble average of 1000 instantaneous samples. ($Q/Q_d = 0.25$).*

figure 7.8b. As expected, both vector maps show a clear departure from the well-behaved, non-separated flow field observed at design load. A much more complex flow pattern has evolved and, most notable, the flow congruence between adjacent passages has apparently been lost. In the lower passage, a large recirculation bubble has been created due to the change in incidence angle at partial load. This bubble covers the visible part of the suction side surface, as shown in the close-up in figure 7.9a. On the contrary, the center passage shows no evidence of separated flow, but is fairly well-behaved although exhibiting large variations in the relative flow angle through the passage. In the upper passage, a low-velocity zone with strong instantaneous vortical structures has emerged, extending over half the passage-width on almost the entire pressure side. Furthermore, at the outlet, a strong vortex with a rotation sense opposite to that of the impeller reverses the flow direction and hence reduces the through-flow in this passage, see figure 7.9b.

The fact that adjacent impeller passages exhibit such distinct flow characteristics at off-design implies the need to extend the sample area to fully grasp the flow physics. Therefore, a supplementary series of 1000 PIV velocity fields was acquired. The camera remained in the same location, but an additional delay of $T/6 = 13.8$ ms, corresponding to the passage time of one impeller blade, was added to the trigger signal from the rotor shaft. In combination, this procedure allowed the collection of data in a region that effectively covered two complete adjacent passages. The result is seen in figure 7.10 where the additional data are shown in red. This last series, although acquired at the same position in the fixed camera reference frame, has been rotated 60 degrees to reflect the effective field-of-view.

A remarkable 'two-channel' flow pattern alternately consisting of stalled and unstalled passages is recognized in figure 7.10, with an apparent flow congruence existing between every second passage. The fact that the two ensemble averages fit perfectly together and therefore fully correspond with the result obtained if the two series had been acquired simultaneously with two cameras, underlines the stationary nature of

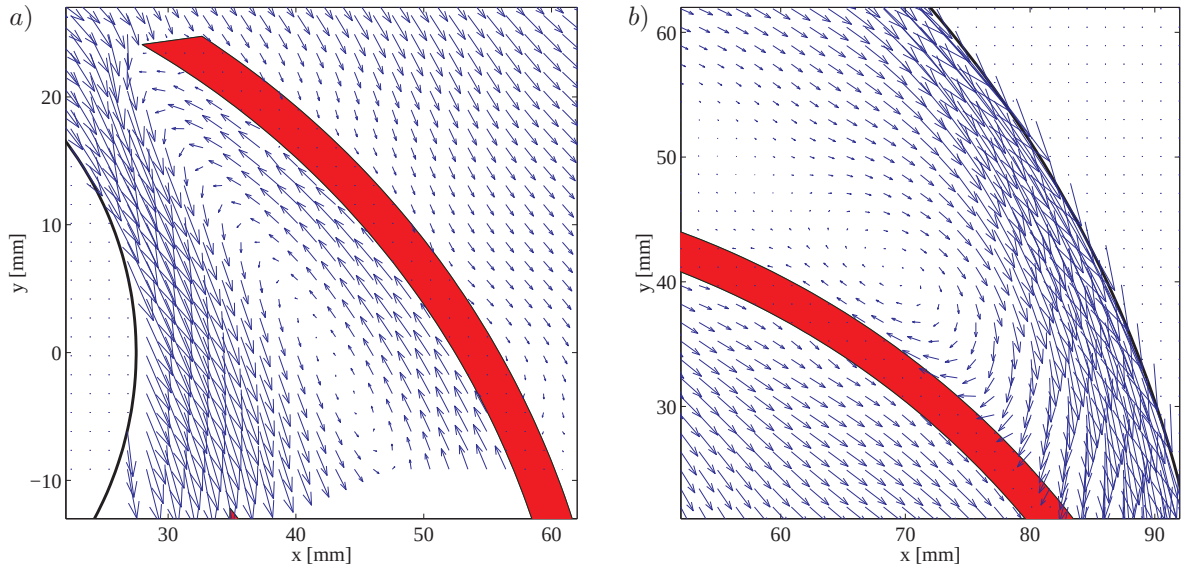

Figure 7.9: *Details of the ensemble averaged relative velocity field $\langle\vec{W}\rangle$ a) Inlet stall cell b) Reversed flow at outlet. $(Q/Q_d = 0.25)$.*

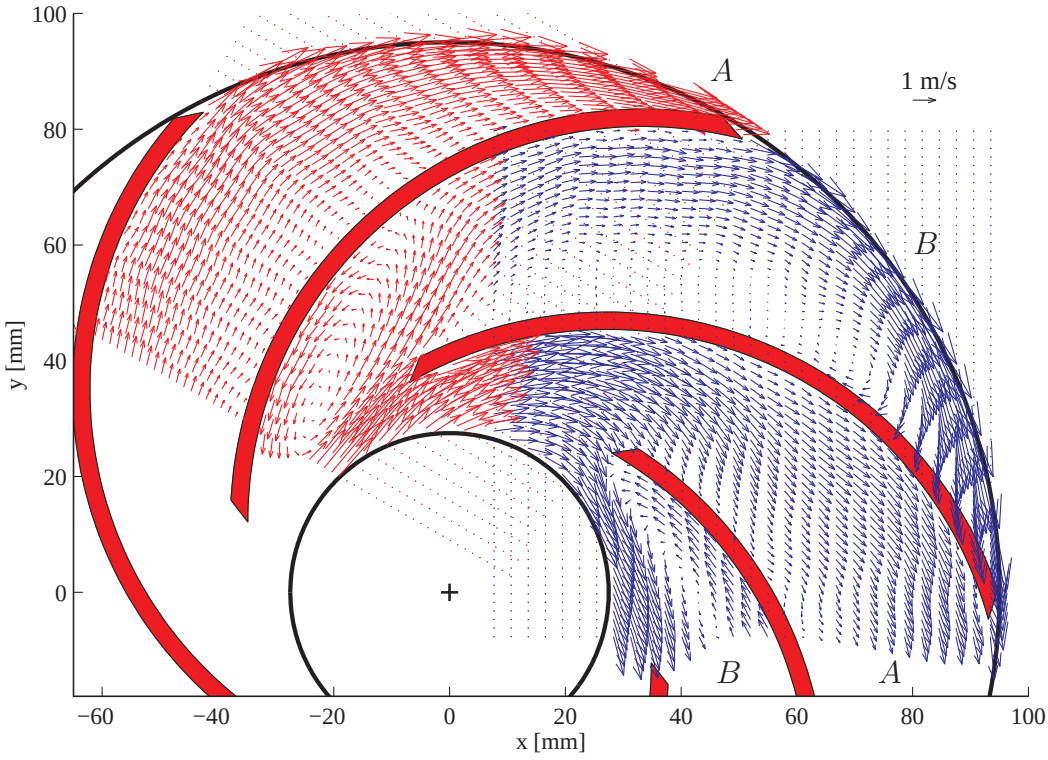

Figure 7.10: *Vector maps of the ensemble averaged relative velocity $\langle\vec{W}\rangle$. The vectors shown in red were acquired separately. The well-behaved passage is denoted A and the stalled passage is denoted B. Only every second vector is shown to avoid crowding. $(Q/Q_d = 0.25)$.*

the detected stall phenomenon. To facilitate discussion, the impeller passage without flow separation is denoted A and the stalled passage B.

In passage B, the large extent of the suction side recirculation zone is notable, with flow re-attaching not taking place until half-way down the blade. The recirculation bubble effectively blocks three-quarters of the entrance to passage B. This in return unstalls passage A in analogy with the mechanisms leading to the propagation of a rotating stall cell, schematically shown in figure 5.6. The present stall phenomenon is, however, non-rotating and also differing from observations in the literature, e.g. [65, 129], in the respect that it is not initiated via the interaction with a stationary component such as a diffuser vane or a volute tongue.

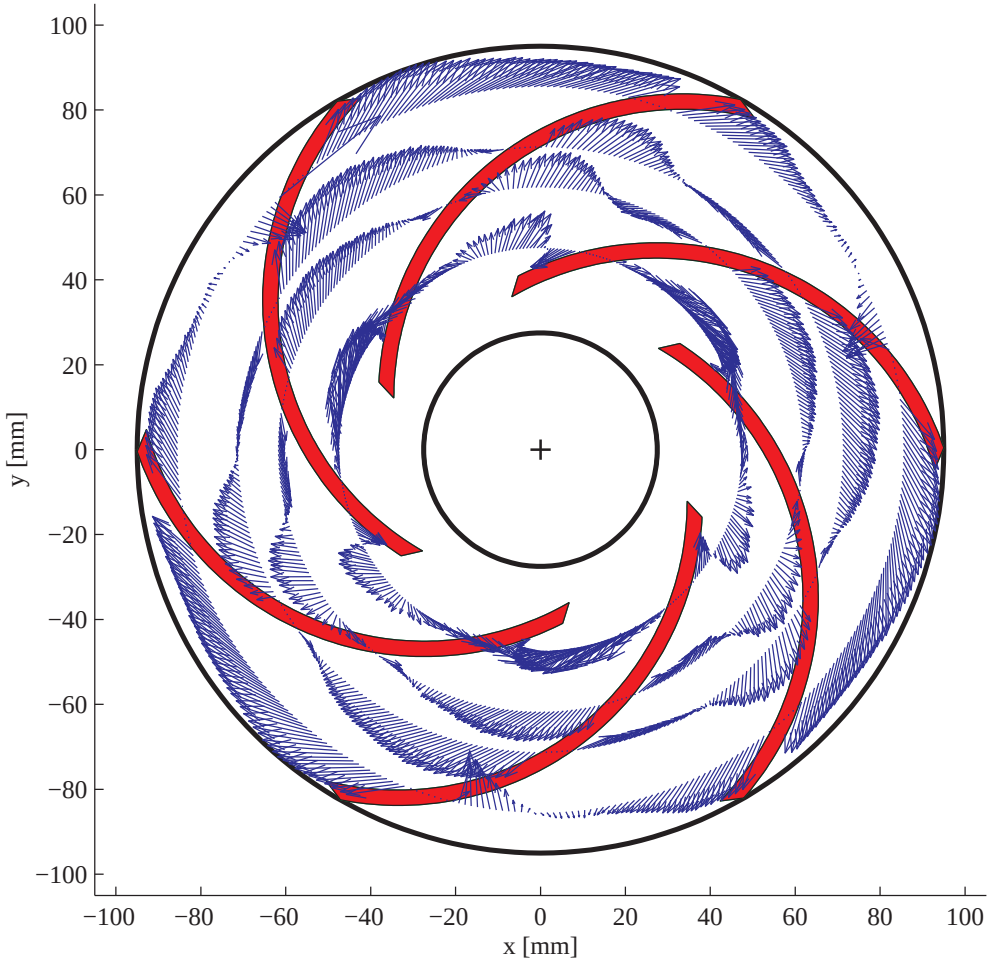

Figure 7.11: *Vector plot of the relative velocity $\langle\vec{W}\rangle$ measured with LDV at radial stations of $r/R_2 = \{0.50, 0.65, 0.75, 0.90\}$. $(Q/Q_d = 0.25)$.*

The hypothesis of every second passage being stalled is fully confirmed by the LDV measurements given in figure 7.11. The vector plot shows the mean relative velocity field measured by sorting the velocity samples into 360 angular bins. A few outliers are visible, but in contrast to the design data in figure 7.3, the inner data at $r/R_2 = 0.50$ do not appear obscured by reflections. A detailed quantitative comparison between PIV and LDV mean data will be given later, but it is readily evident, that the LDV

velocity field corresponds well to the ensemble averaged PIV flow picture in figure 7.10. However, the reversed flow along the pressure side of passage B seems more pronounced, compared to the PIV ensemble average in figure 7.8 which merely gives evidence of a low-velocity dead-water zone.

Nevertheless, both data sets reveal the presence of a strong relative eddy that dominates the flow structure in the central and outer parts of passage B. It gains significant strength towards the outlet, where fluid is swept from suction to pressure side in accordance with the schematic motion shown in figure 5.3a. The clockwise rotation of the eddy brings fluid backwards along the pressure surface where it is later diverted towards the suction side, with the apparent effect of suppressing separation there. A potential vortex with very similar characteristics was observed by Abramian and Howard [1] in a low-specific speed impeller operating at a flow rate of $0.50Q_d$. Visser et al. [120] also reported high passage velocities at the suction side and near-stagnation flow on the pressure, evidencing the presence of a strong relative eddy. The unusual confinement of flow separation to the blade pressure side may also, to a lesser extent, be influenced by the curvature-induced secondary flows shown in figure 5.4c that tend to move the stable location of low-momentum fluid towards the pressure side in impellers with backward swept blades, such as the present.

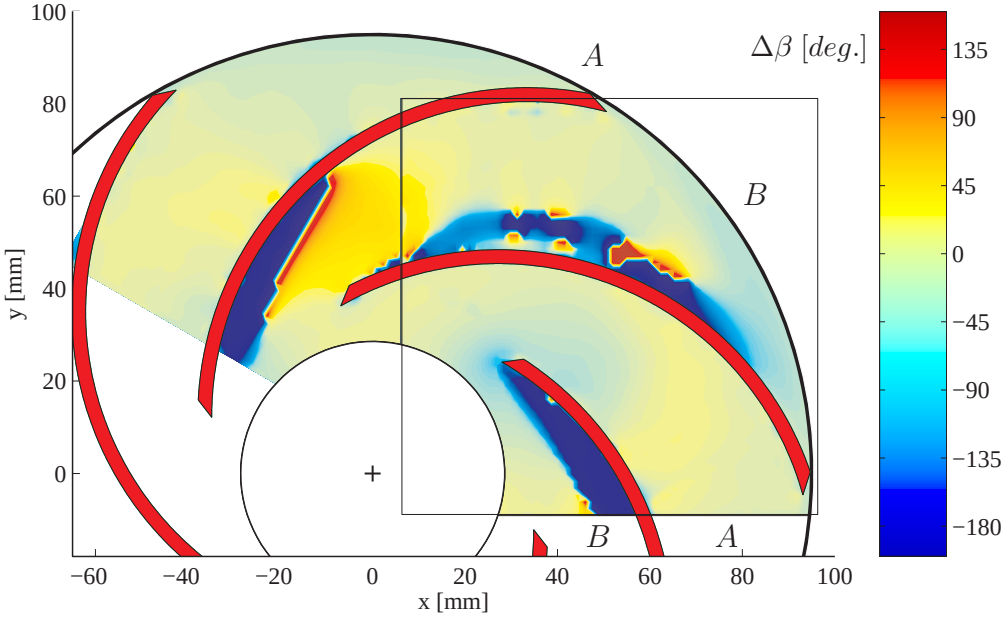

Figure 7.12: *Ensemble averaged deviation angle $\langle\Delta\beta\rangle = \langle\beta\rangle - \beta_2$ between the relative flow angle and the outlet blade angle $\beta_2 = 18.4°$. $(Q/Q_d = 0.25)$.*

The contour plot of $\langle\Delta\beta\rangle$ shown in figure 7.12 reveals that values numerically larger than 90°, i.e. backflow, exist along almost the entire pressure surface in passage B. Overall, figure 7.12 supports the impression of a flow in passage B governed by the interaction between the inlet stall cell effectively blocking the passage, and the potential passage vortex formed because of this flow blockage. Turning to passage A, the deviation angles attain values only slightly larger than those observed at design conditions. At the outlet, however, significant flow deviations seem present in both passages.

The significant strength of the inlet stall cell in passage B is quantified in figure 7.13 which reveals a pronounced magnitude of out-of-plane vorticity $|\langle\Omega_z\rangle|$ across the inlet. A small clockwise rotating vortex is also seen to be shed from the pressure leading edge. The pattern in passage A, on the other hand, resembles that observed at design conditions with vortical structures shed from the leading edge and migrating downstream along the blade suction surface.

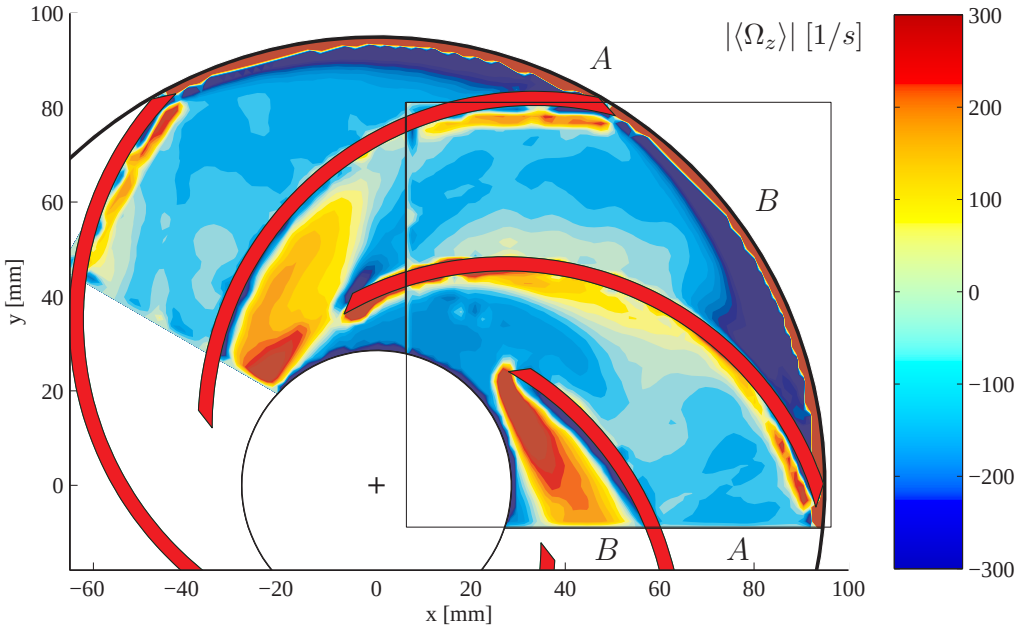

Figure 7.13: *Contour plot of the magnitude $|\langle\Omega_z\rangle|$ of the out-of-plane vorticity based on ensemble averaged data acquired separately in passages A and B. $(Q/Q_d = 0.25)$.*

7.3.1 Turbulent fluctuations

The deviation of a sample instantaneous velocity from the ensemble average is shown in figure 7.14a, and the corresponding out-of-plane vorticity component in figure 7.14b, suggesting a highly turbulent flow. The fluctuating velocity vectors show large spatial structures in passage B covering most of the passage width.

Figure 7.15 shows highly elevated levels of k_{2D} along the core of the suction side separation bubble, extending from the leading edge towards, and past, the leading edge of the next arriving impeller vane. Significant turbulent activity is also associated with the flow reversal near the outlet of passage B, although parts of this high level may be attributed to movement of the relative eddy itself, rather than to the effect of turbulence. Generally, k_{2D} attains values more than twice the level measured at full-load conditions. Expressed in terms of Tu, typical values of 8–10% are found in the regions described, with a peak of 15% just before the outlet.

Summarizing the observations done at quarter-load, a highly distorted flow with a remarkable 'two-channel' pattern characterized with flow congruence between every second passage has emerged. The flow in the passage denoted A is dominated by

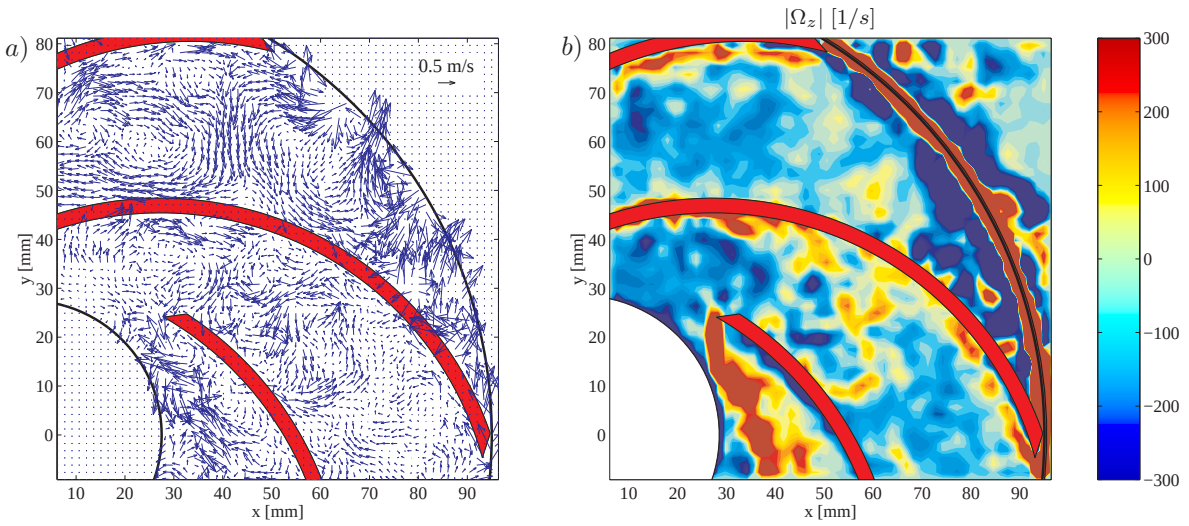

Figure 7.14: *a) Sample instantaneous deviation $\vec{C} - \langle\vec{C}\rangle$ from ensemble average. b) Corresponding instantaneous out-of-plane vorticity component $|\Omega_z|$. $(Q/Q_d = 0.25)$.*

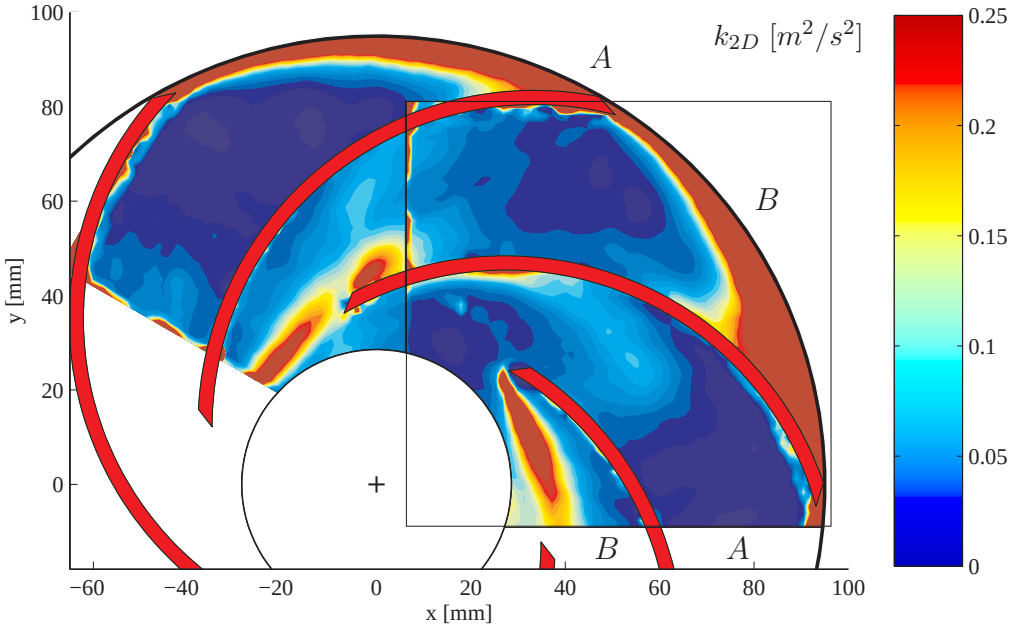

Figure 7.15: *Contour plot of the measured portion k_{2D} of the turbulent kinetic energy. $(Q/Q_d = 0.25)$.*

rotational effects and resembles the well-behaved design flow, although with higher turbulent activity. In passage B a stationary inlet stall cell blocks the inlet section and gives rise to a relative eddy dominating the remaining parts of the passage. As a result, the effective flow rate passing through passage B is minimal, dramatically deteriorating the performance of the impeller at this off-design operating point.

Compared to observations in the literature, the detected off-design stall phenomenon is unique in the sense that it is stationary, non-rotating and only appears in every second passage. No reports of a similar 'two-channel' phenomenon have been found in the literature. It may be speculated that the stationary stall appearance is dictated by the even number of passages that enables a stable equilibrium mode between the forces acting on the stall cells, and subsequently locks their circumferential positions within the impeller. Any influence of geometrical asymmetries may be ruled out as consecutive runs with the impeller could cause the two-channel phenomenon to lock in different passages.

7.4 Rotor-stator interaction

It is well-known from numerous studies, e.g. [29, 9, 7, 32, 84, 106], that rotor-stator interaction between a rotating impeller blade and a stationary diffuser vane (or volute tongue) may significantly alter the flow characteristics in both components. As thoroughly discussed by Dring et al. [29] and Arndt et al. [9], the rotor-stator interaction between two blade rows moving relative to each other can be divided into two different mechanisms: potential flow effects and wake interaction. The potential flow effects are due to the circulation and blockage of the blades and the wake interaction refers to the unsteadiness induced by wakes shed by upstream blades and convected downstream. Both effects result in unsteady fluid forces acting on both rotor and stator. This is evidenced e.g. by Arndt et al. [9] who measured downstream pressure fluctuations on diffuser vanes that were of the same magnitude as the total pressure rise across the pump investigated. Significant upstream distortions of the internal impeller flow may also result as observed by e.g. Eisele et al. [32] and Muggli et al. [84], and ultimately lead to rotating stall.

To demonstrate the potential of PIV as a tool for the identification of unsteady and cyclic flow events generated by rotor-stator interaction, a series of measurements were performed with a constant-height diffuser installed, see section 6.3.2. A main objective was also to investigate whether the stationary 'two-channel' phenomenon observed at quarter-load in the isolated impeller is altered by rotor-stator interaction.

7.4.1 Vaned diffuser

The geometrical layout of the vaned diffuser was shown in figure 6.2 on page 67. It consisted of 11 straight vanes and the interblade spacing was 8% of the impeller radius, i.e. the leading edge of the diffuser vanes was located at $R_3 = 1.08R_2$. This radial gap represents an intermediate value compared to common practice and investigations in the literature that range between 1.5% [9] and 20% [106] of the impeller radius. The inlet angle β_3 of the diffuser vanes with respect to the circumferential direction was chosen to 20° as this roughly corresponds to the mean absolute flow angle measured

at the rotor exit at Q_d, see figure 7.16. The number of diffuser vanes was chosen to $Z_d = 11$ to avoid low common denominators between Z_d and $Z_i = 6$. This is common praxis in turbomachinery design in order to eliminate subharmonic excitations that may cause structural vibration problems [15]. Although the simple diffuser geometry depicted in figure 6.2 does not resemble that of the real CR4 return-channel, it mimics the flow distortions induced by rotor-stator interaction with an industrial diffuser.

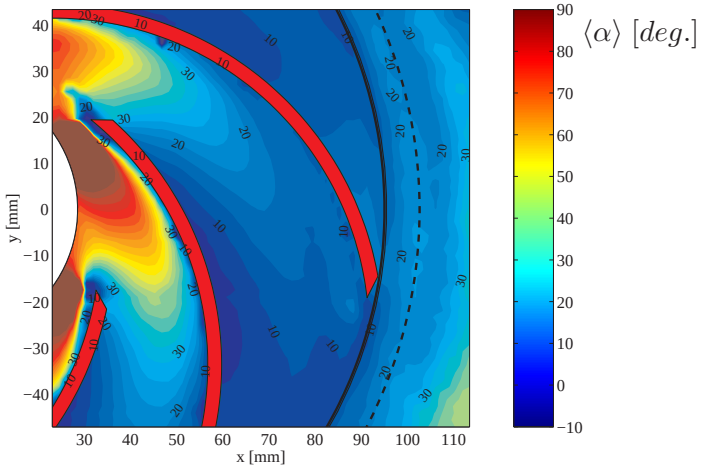

Figure 7.16: *Ensemble averaged absolute flow angle $\langle\alpha\rangle$ measured in the impeller setup without vaned diffuser. The dashed line indicates the inlet radius of the vaned diffuser. ($Q/Q_d = 1.0$).*

7.4.2 Phase-resolved results

Figure 7.17 shows six samples of instantaneous vector maps acquired at quarter-load at different phases of the blade-passing cycle, i.e. different orientations of the impeller blade with respect to the diffuser. The increment between two impeller blade positions is approximately 8 degrees in the circumferential direction. Due to the maximum sampling frequency of 10 Hz that was imposed by the Nd:YAG laser, the instantaneous velocity distributions a to f do not stem from consecutive recordings, i.e. they are not acquired within one single revolution of the impeller. Nevertheless, they demonstrate the evolution of the cyclic flow perturbations that are caused by interaction between the two blade rows, including the convection of the impeller blade wakes.

The latter mechanism is visualized by the instantaneous distributions of $|\Omega_z|$ given in figure 7.18. Note that the vorticity inside the impeller passages is predominantly positive due to the impeller rotation. Vortices are seen to be shed from the trailing edge of the impeller blade and convected into the vaned diffuser where they interact with vortices shed from upstream blades. The wake produces regions of positive and negative vorticity which are equal in strength in accordance with the observations of Eisele et al. [32] in a highly loaded diffuser. The vortex pattern thus resembles that of a classical von Kármán vortex street which was investigated in Part B of this thesis. In contrast, Akin and Rockwell [7] reported an impeller wake with pronounced concentrations of vortices rotating in one direction, typical of those occurring in mixing-layers.

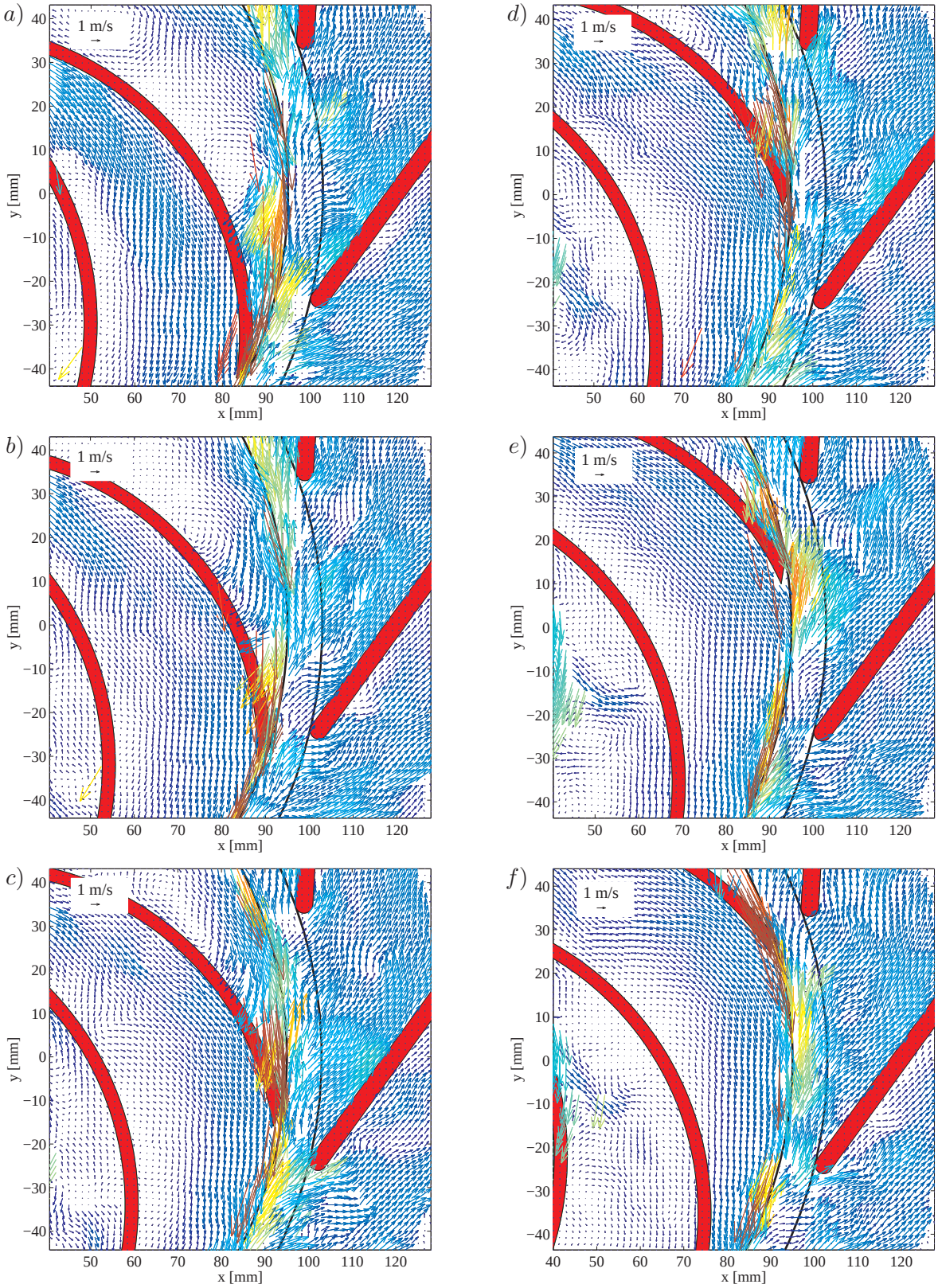

Figure 7.17: *Sample instantaneous vector maps measured at phases a–f of the blade-passing cycle. The vectors show the relative velocity $\vec{W}$ inside the rotating passages and the absolute velocity $\vec{C}$ outside the impeller. The vectors are color-coded with the local speed. ($Q/Q_d = 0.25$).*

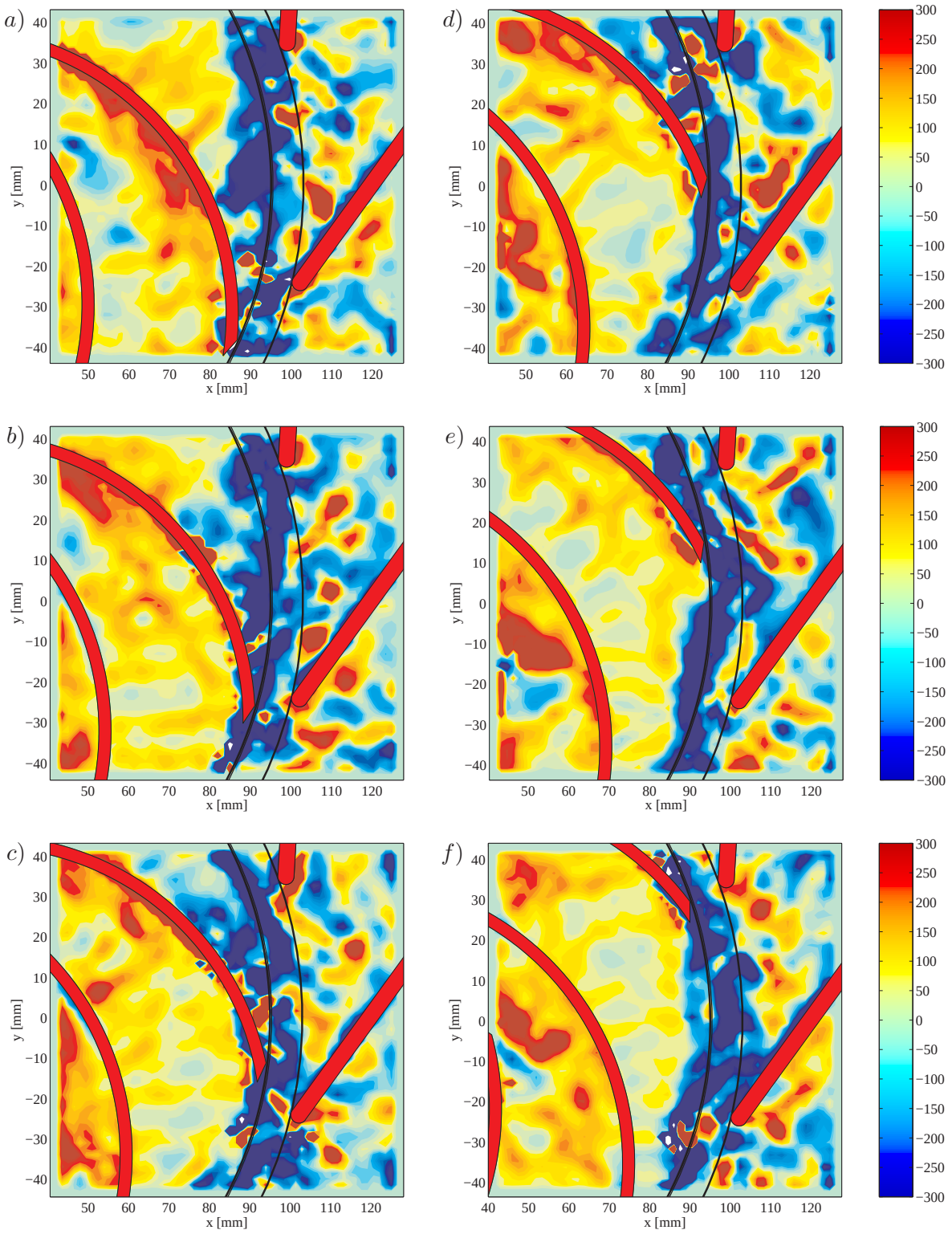

Figure 7.18: *Sample instantaneous distributions of out-of-plane vorticity, $|\Omega_z|$, based on the velocity vector maps shown in figure 7.17. $(Q/Q_d = 0.25)$.*

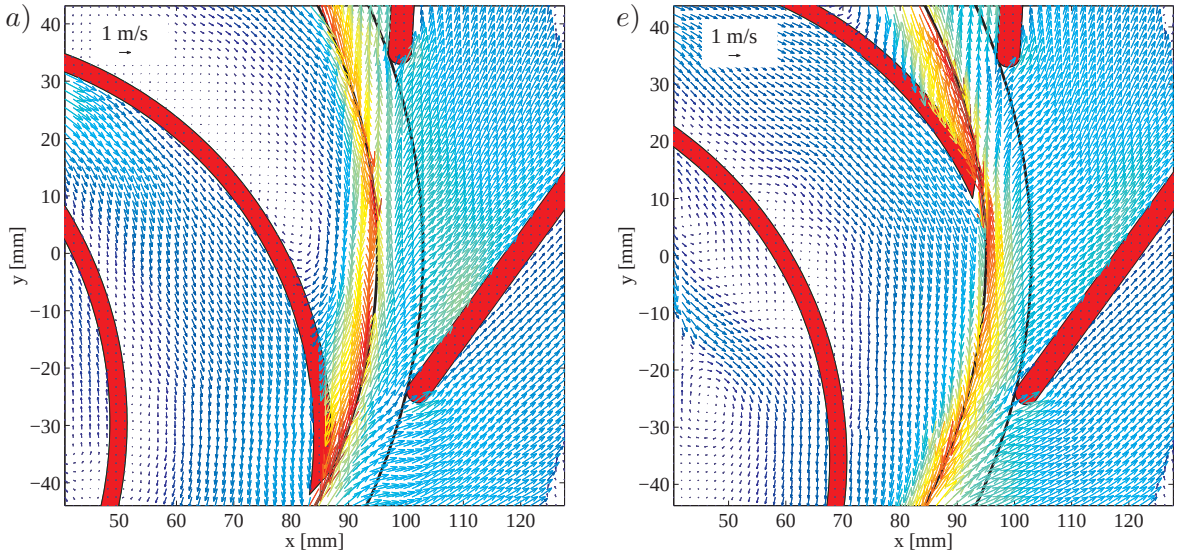

Figure 7.19: *Ensemble averaged vector maps based on 1000 realizations acquired at phases a and e, respectively, of the blade-passing cycle (compare figure 7.17). The vectors show the relative velocity $\langle\vec{W}\rangle$ inside the rotating passages and the absolute velocity $\langle\vec{C}\rangle$ outside the impeller. ($Q/Q_d = 0.25$).*

Ensemble averages of 1000 instantaneous realizations are presented in figure 7.19. For the sake of brevity, only ensemble averages for the impeller positions corresponding to subplots a and e in figure 7.17 are shown. The upper impeller passage in figure 7.19a shows a clockwise rotating vortex at the blade pressure side, indicating that this passage is stalled. In figure 7.19e this stalled passage has moved out of the sample area and has been replaced by a non-separated passage. However, the strong inlet recirculation cell present in the lower passage of figure 7.19e shows that a new stalled passage is approaching. These observations suggest that the 'two-channel' stall phenomenon observed in the isolated impeller persists even with the vaned diffuser in place.

Comparison of the two ensemble averages in figure 7.19 reveals no significant effect of the impeller blade orientation on the mean flow inside the diffuser, at least not to a level that is evident solely from examinations of the vectors. To elaborate further on this, distributions of turbulent kinetic energy k_{2D} is given in figure 7.20. These demonstrate that cyclic flow distortions actually are present in the inlet section of the vaned diffuser, but also that the level of turbulence rapidly falls off as the flow moves downstream the diffuser and decelerates.

As suggested by Sinha et al. [106], the effect of the blade orientation may be highlighted by calculating the cyclic velocity distribution $\Delta\vec{C}$. This quantity is obtained by first calculating the total average of all phase-averages, taking into account all measured impeller blade positions within the blade-passing cycle. The difference between this total average and each individual phase-average then yields the cyclic velocity $\Delta\vec{C}$ for each phase. Figure 7.21 shows $\Delta\vec{C}$ for phases a, c, e and f, respectively, of figure 7.17. The velocity vectors indicate the direction of the cyclic velocity and the color its magnitude.

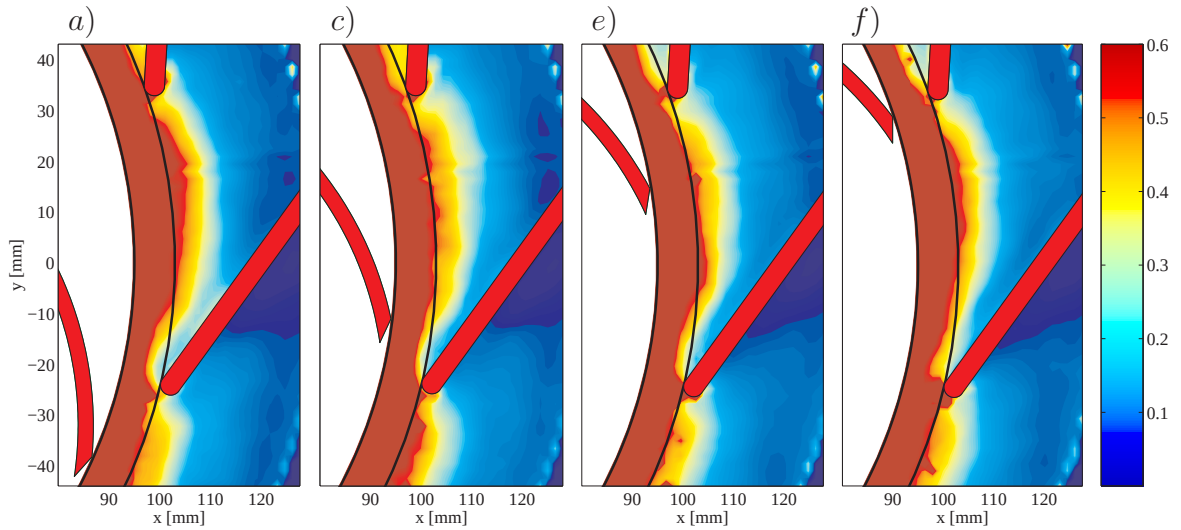

Figure 7.20: *Turbulent kinetic energy k_{2D} $[m^2/s^2]$ in the vaned diffuser at phases a, c, e and f of the blade-passing cycle, see figure 7.17. ($Q/Q_d = 0.25$).*

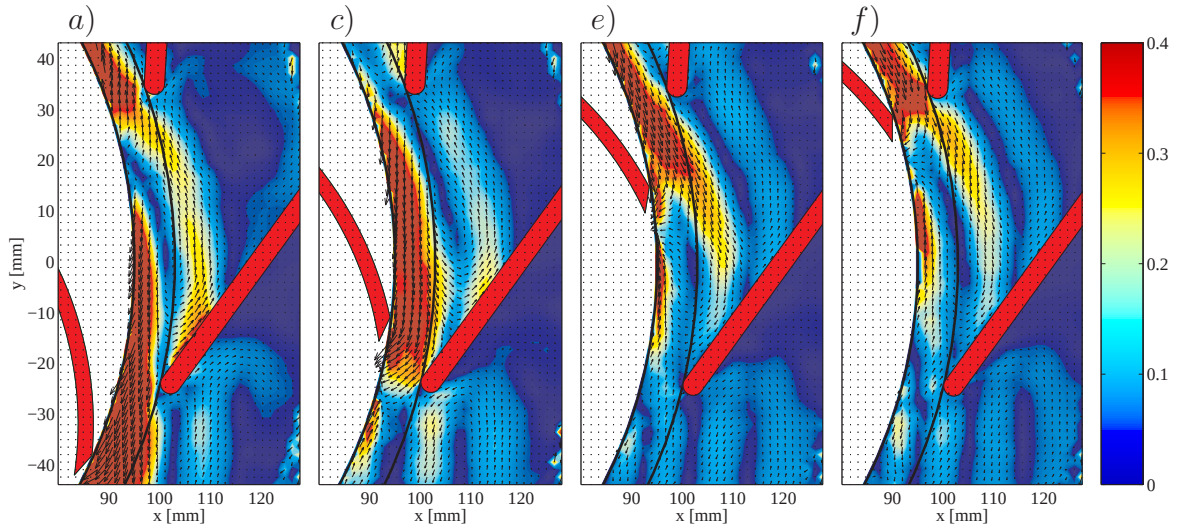

Figure 7.21: *Cyclic velocity $\Delta\vec{C}$ $[m/s]$ in the vaned diffuser at phases a, c, e and f of the blade-passing cycle, see figure 7.17. ($Q/Q_d = 0.25$).*

Figure 7.21 reveals a much more pronounced influence of the impeller blade orientation compared to the turbulence levels in figure 7.20. It is seen that large cyclic velocities exist in the gap between impeller and diffuser vane. An interesting feature is the presence of a U-shaped pattern of cyclic velocities that is convected downstream in the diffuser as the impeller blade passes by. Comparing the magnitudes of the turbulent fluctuations k_{2D} with the square of the cyclic variation $(\Delta\vec{C})^2$ suggests that the turbulent fluctuations are generally larger than the cyclic variations. However, the opposite trend exists in between rotor and stator. Therefore, a firm conclusion on the relative effects of turbulence and cyclic flow structures would require a more detailed analysis, as recently done by Sinha et al. [106]. They observed peaks of $(\Delta\vec{C})^2$ that were generally twice as large as the peaks of k_{2D} within the diffuser.

The present data base may be explored further to quantify such relationships. However, it is not the intention of the present study to perform a close analysis of the complex rotor-stator interaction mechanisms, but merely to highlight the instantaneous and periodic spatial flow structures that can be readily deduced from the PIV data.

7.5 Summary

Digital particle image velocimetry measurements inside the passages of a perspex centrifugal impeller of industrial design were presented. The main focus of the investigation was to identify steady and unsteady flow features at severe off-design conditions. The experimental setup and technique have proved to be efficient in providing reliable and detailed data over a full blade passage, also in the close vicinity of walls due to the use of fluorescent seeding.

Measurements performed at the design operating point, $Q = Q_d$, show a well-behaved vane congruent flow with no separation occurring, and reveal a distinct flow congruence between all six passages. The flow is dominated by rotational effects apart from local curvature effects in the inlet section.

At severe off-design conditions at a flow rate of $Q = 0.25Q_d$, a previously unreported 'two-channel' phenomenon consisting of alternate stalled and unstalled passages, i.e. flow congruence between every second passage, was observed. A large high-turbulent recirculation cell blocked the inlet to the stalled passage and a strong relative eddy dominated the remaining parts of the passage causing backflow along the blade pressure side at large radii. This can be viewed as a quasi-inviscid behavior due to the apparent dominating effect of the potential flow characteristics over viscous effects.

The detected stall phenomenon is steady and non-rotating. This may be due to the even number of vanes and the fact that the stall is not initiated via the interaction with any stationary components. In these respects, the present stall phenomenon differs from the periodic unsteadiness of the relative flow known as rotating stall, which typically moves in the direction of rotation at a lower speed than that of the impeller.

A qualitative study of the spatial flow structures associated with rotor-stator interaction was performed by installing a vaned diffuser with 11 straight vanes in the test rig. This highlighted the influence of impeller blade orientation on the flow and revealed considerable cyclic variations. The 'two-channel' stall phenomenon detected at part-load was not significantly influenced by the presence of the diffuser.

Chapter 8

Comparison with LDV and LES

As demonstrated in the previous chapter, much knowledge of the global flow features in the centrifugal impeller may be gained from a direct study of the planar PIV velocity fields and the quantities deduced thereof. Nevertheless, in order to substantiate the observations and to assess the accuracy of the ensemble averaged PIV data, a comparative study with LDV mean data is presented in this chapter. The comparisons are based on blade-to-blade distributions of selected quantities that have been extracted from the PIV data. Furthermore, possible departures from a two-dimensional flow field are investigated based on LDV data acquired at different axial stations in the impeller. Finally, the potential use of the PIV database as a valuable tool for the evaluation of advanced numerical methods is demonstrated through comparisons with recent Large Eddy Simulations (LES) [18] of the present impeller flow.

8.1 Data extraction and reduction

Figure 8.1 shows the 6 radii at which LDV data were acquired, as described in section 6.5. These radial stations therefore form the basis of the comparisons between PIV and LDV. However, since the PIV and LDV data sets are conceptionally very different, a number of data extraction and reduction procedures are needed to facilitate this comparison. These procedures are briefly explained below.

8.1.1 PIV data

Figure 8.2 shows a sample blade-to-blade distribution of the radial velocity $\langle C_r \rangle / U_2$ obtained by bi-linear interpolation of the planar PIV data obtained at part-load onto a line of constant radius, $r/R_2 = 0.75$. The abscissa spans two pressure-to-suction side intervals in order to represent the unstalled (A) and stalled passages (B) observed at quarter-load. The pressure and suction sides are denoted PS and SS, respectively, and their angular positions marked by triangles. The profile in figure 8.2 is divided into segments to indicate that the data originate from two different measurement series. As becomes evident by consulting figure 8.1, the blue segment stems from the original field-of-view II, whereas the green segments were extracted from the additional measurements in the 'tilted' field-of-view (corresponding to the red vectors in figure 7.10).

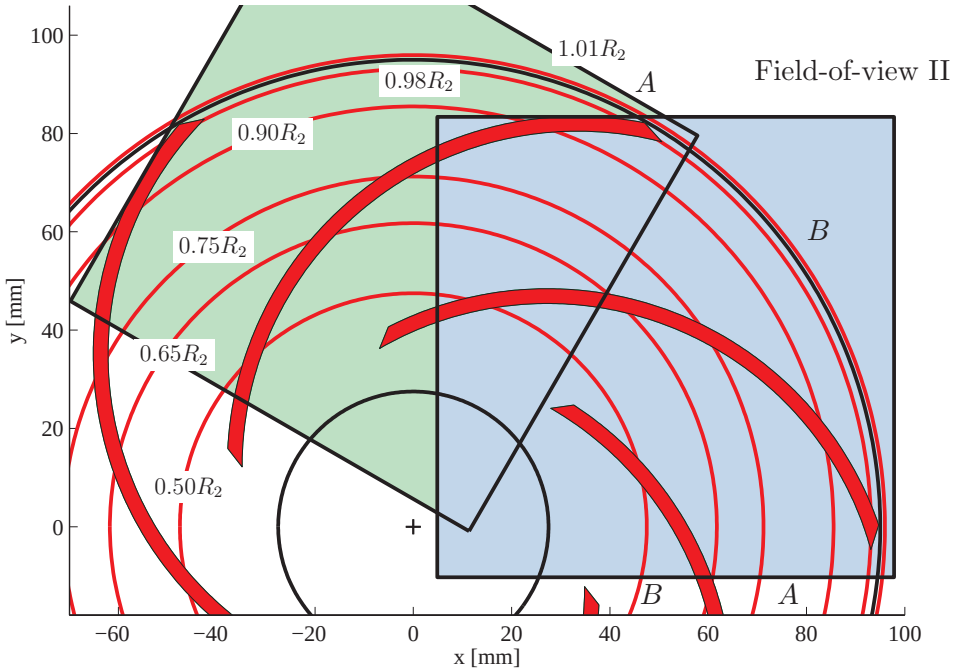

Figure 8.1: *Blade-to-blade distributions of PIV data were extracted at the 6 radial stations,* $r/R_2 = \{0.50, 0.65, 0.75, 0.90, 0.98, 1.01\}$*, where LDV data were acquired.*

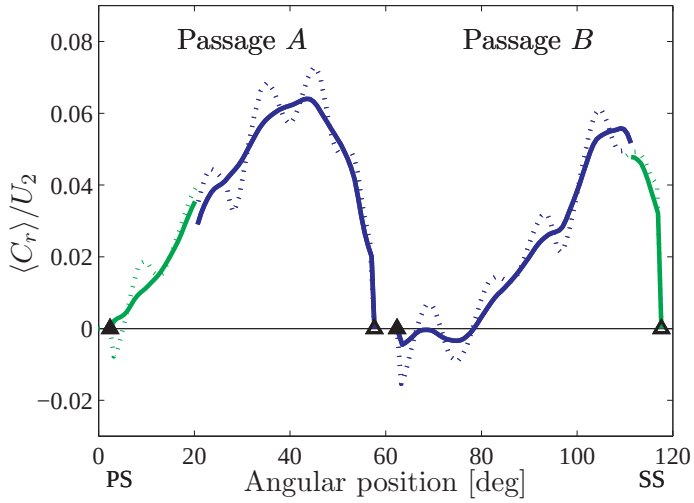

Figure 8.2: *Sample blade-to-blade distribution of the radial velocity* $\langle C_r \rangle / U_2$ *extracted from the PIV data at a constant radius of* $r/R_2 = 0.75$*. The unbroken line segments stem from PIV data processed using the Gaussian sub-pixel interpolation scheme, whereas the dotted lines show the impact of pixel-locking associated with the parabolic estimator.* $(Q/Q_d = 0.25)$*.*

The continuous appearance of the joint segments demonstrates the high degree of reproducibility inherent in the measurements, and the color-coding will therefore be omitted hence-forward.

Figure 8.2 also illustrates the impact that an incautious choice of sub-pixel interpolation scheme at the PIV image processing stage may have on extracted velocity profiles. As discussed in section 6.4.5, the parabolic estimator is more prone to pixel-locking effects, i.e. the bias of measured displacements towards integer pixel values. The dotted lines in figure 8.2 demonstrate how pixel-locking associated with the parabolic estimator manifests itself as non-physical wiggles in the bi-linearly interpolated profile. This supports the advantageous use of the Gaussian scheme in setups where a slight under-sampling of the particle images cannot be avoided at the recording stage. However, even the Gaussian estimator (unbroken lines) leaves some wiggle effects in the blade-to-blade distributions. In cases where these were considered unlikely to be a true feature of the flow, a pre-filtering using a 3×3 smoothing kernel was applied to the 2D data fields before any interpolation was performed.

8.1.2 LDV data

Samples of the LDV data in the form of vector plots of the relative velocity vector $\vec{W}$ have already been shown in figures 7.3 and 7.11. Below, a closer look at the raw LDV data is given. Figure 8.3 shows the bin-resolved absolute velocity components $\langle C_r \rangle$ and $\langle C_t \rangle$ acquired at $r/R_2 = 0.90$ at design flow, together with the RMS-velocity C'_r and the number of velocity samples collected in each angular bin. The similarity between all six passages is apparent. The few local outliers result from a registration of the movement of the blade surface through the measurement volume, evidenced by the fact that the observed peak tangential velocity corresponds exactly to the circumferential impeller speed at $r/R_2 = 0.90$.

Parallel conclusions of well-converged data may be drawn from the LDV velocity field acquired at quarter-load, see figure 8.4, but now with flow congruence between every second passage. Therefore, representative mean passage profiles have been calculated from the LDV data by averaging all passages at Q_d and every second of the six passages at $0.25Q_d$, respectively. To ensure the same statistical sample size at both flow rates, the number of velocity samples in each angular bin was doubled at $0.25Q_d$. This resulted in a uniform number of, in average, 3333 samples in each angular bin, comparable to the 1000 instantaneous realizations in the PIV ensemble averages. No smoothing of the LDV data was applied.

8.2 Blade-to-blade distributions

8.2.1 Radial velocity

Figure 8.5 compares the blade-to-blade distributions of the radial velocity component $\langle C_r \rangle$ measured with PIV and LDV and assigned to representative passages as just described. It should be noted that the radial components $\langle C_r \rangle$ and $\langle W_r \rangle$ are equivalent. The left column of figure 8.5 shows the design load observations and the right column shows the passages A and B observed at quarter-load. The velocity profiles are made

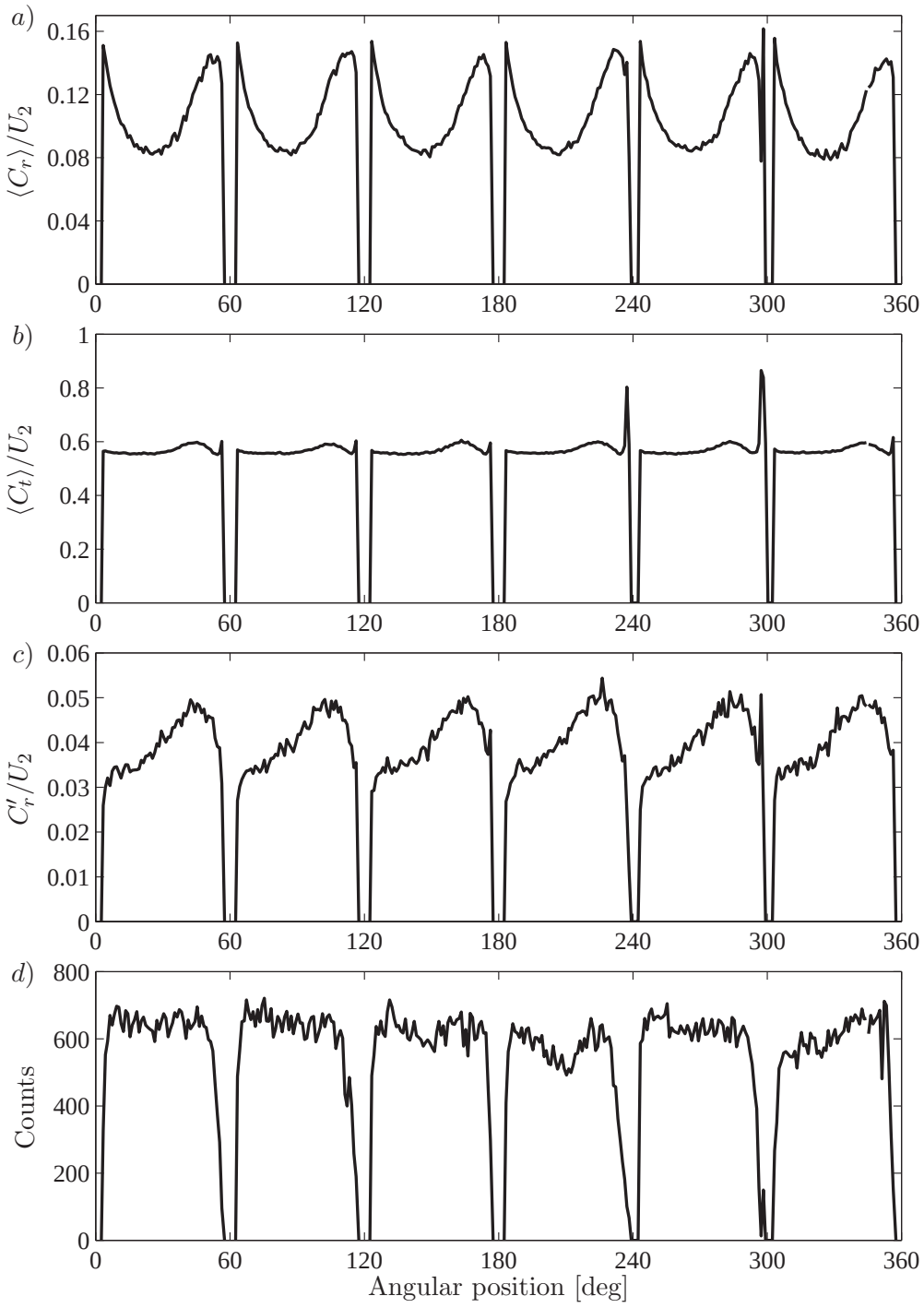

Figure 8.3: *Bin resolved LDV data obtained at* $r/R_2 = 0.90$. *a) Radial velocity* $\langle C_r \rangle$ *b) Tangential velocity* $\langle C_t \rangle$ *c) RMS-velocity* C_r' *d) Number of radial velocity samples.* $(Q/Q_d = 1.0)$.

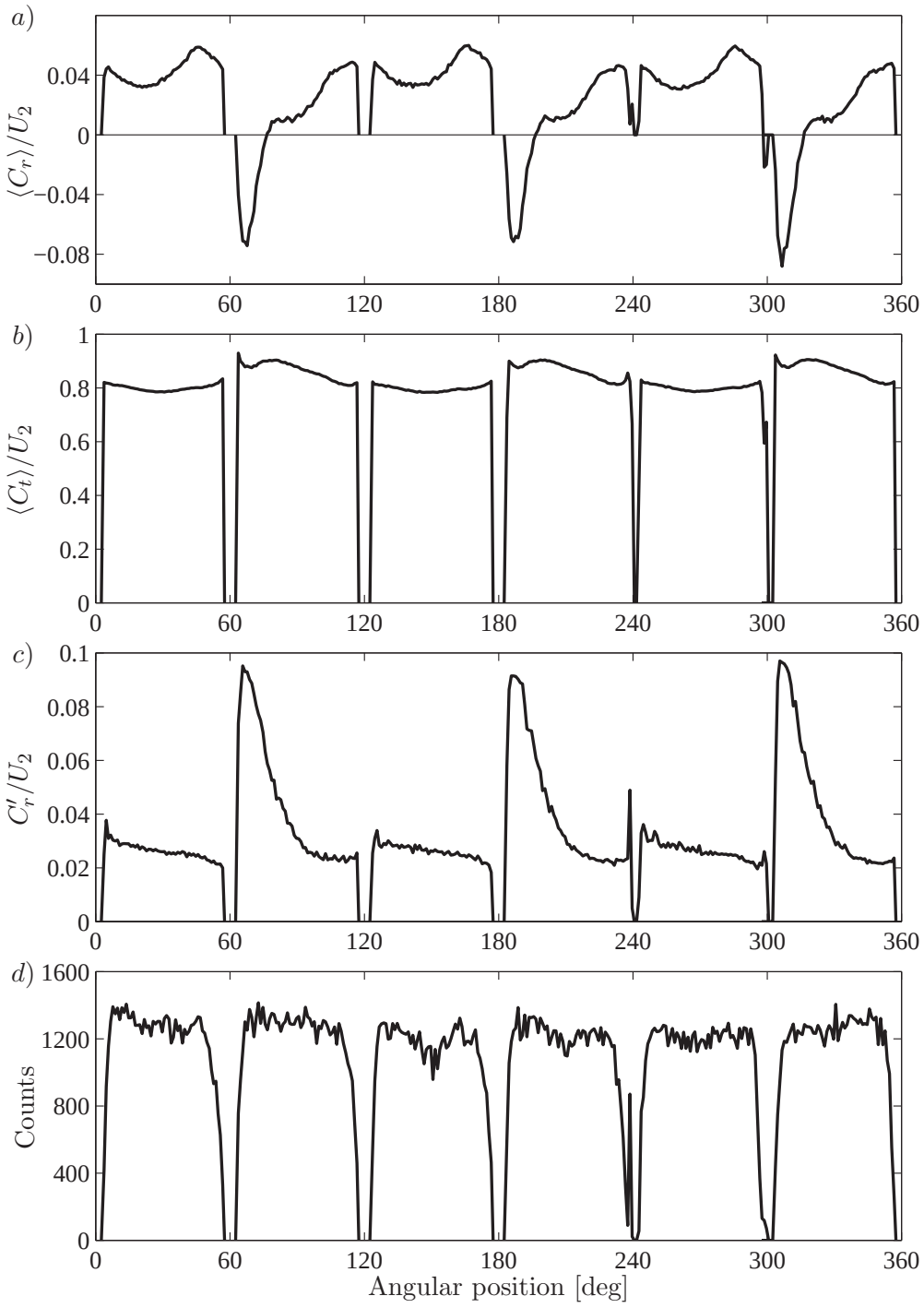

Figure 8.4: *Bin resolved LDV data obtained at* $r/R_2 = 0.90$. *a) Radial velocity* $\langle C_r \rangle$ *b) Tangential velocity* $\langle C_t \rangle$ *c) RMS-velocity* C'_r *d) Number of radial velocity samples.* $(Q/Q_d = 0.25)$.

dimensionless with the impeller speed at the outlet U_2, and are given for radii of $r/R_2 = 0.50$, 0.75 and 0.98 (impeller outlet), respectively. As previously discussed, no valid LDV data were available at the inner radial station.

In general, figure 8.5 reveals a good agreement between the two data sets. At design load, the flow starts off as potential flow with a radial velocity profile that is skewed markedly towards the suction side at $r/R_2 = 0.50$. This displacement of the flow core suggests that viscous effects have not yet developed at this radial station, leaving a flow governed by curvature and the possible presence of a swirl component in the inlet flow. Both effects work to raise the radial velocities near the suction side.

Traveling outwards through the impeller passage, the radial velocity profile evens out under the influence of the Coriolis force that moves the core flow towards the pressure side at large radii. Although some discrepancy may be observed between the PIV and LDV profiles at $r/R_2 = 0.75$, they agree well at the outlet, where the largest radial velocities now exist near the pressure side due to the unloading of the blade. Overall, the design flow pattern is in accordance with classical streamline theory.

Moving on to the quarter-load data, passage A exhibits the same main characteristics as seen at design flow, with the addition of local flow features such as reversed flow near the pressure side at the inner radial station. The flow in passage B, however, is dictated by the suction side inlet stall cell. This is seen to cover a third of the passage at $r/R_2 = 0.50$ with backflow velocities reaching a magnitude of 55% of the maximum outward component. Large positive velocities exist in the passage center, feeding the recirculation bubble. At $r/R_2 = 0.75$, PIV and LDV agree on the location and height of the positive peak in passage B which has now moved to the suction side due to the strengthening of the relative eddy. Near the pressure side of passage B, PIV detects a dead-water zone whereas LDV shows distinct recirculation, as previously mentioned.

At the outer radial station of $r/R_2 = 0.98$ the two profiles virtually collapse and uncover the significance of the flow reversal that covers two-thirds of the outlet of passage B. Hence, the outer radial station of channel B gives evidence of a stalled passage with almost no, if any, through-flow. Comparing this to the apparent net positive through-flow at $r/R_2 = 0.50$, suggests that three-dimensional effects are present in this industrial-type impeller. To elaborate further on this, LDV data obtained at other axial positions than in the mid-height plane, $z/b_2 = 0.50$, will be presented later.

Considering the strict conditions associated with a quantitative comparison of LDV and PIV data acquired in different measurements grids, and with different seeding particles in a flow with large spatial gradients, a satisfactory agreement has been obtained.

8.2.2 Turbulence intensity

A more demanding test than the comparative study of mean velocities just presented, is a comparison of statistical moments. For that purpose, figure 8.6 shows the turbulence intensities $Tu = \sqrt{k_{2D}}/U_2$ calculated from the PIV and LDV ensemble averages.

The LDV data at design load show a distribution of Tu that varies almost linearly from about 3% in the pressure side region to 5–6% close to the blade suction surface. This distribution of low Tu persists throughout the impeller and is indicative of a stable flow at this operating condition. Interestingly, the turbulence intensities measured by PIV at the two inner radial stations are about 40% smaller than the values attained

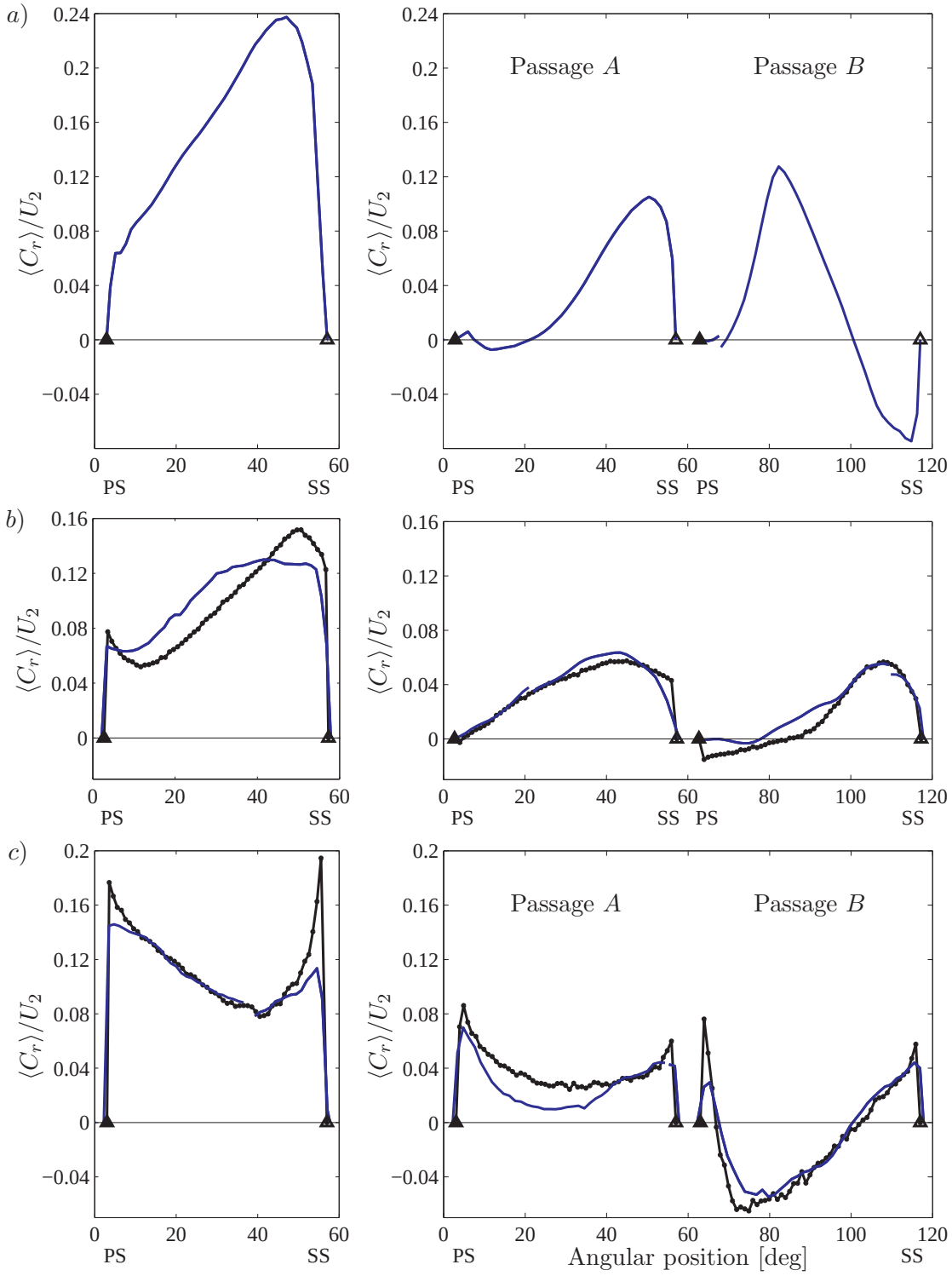

Figure 8.5: *Blade-to-blade distributions of the mean radial velocity $\langle C_r \rangle / U_2$ measured with PIV (—) and LDV (—) at flow rates of Q_d (left) and $0.25Q_d$ (right). a) $r/R_2 = 0.50$, b) $r/R_2 = 0.75$, c) $r/R_2 = 0.98$.*

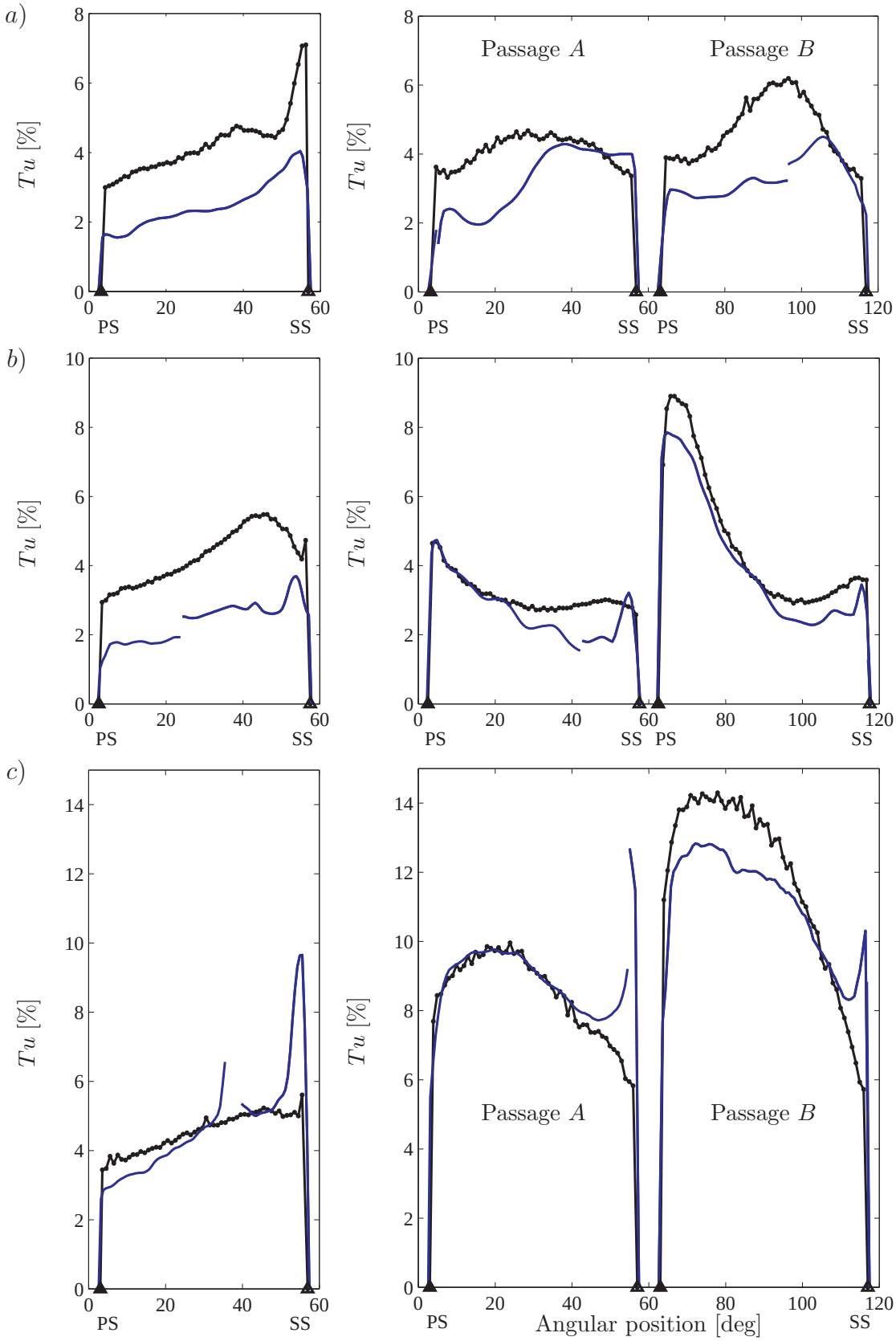

Figure 8.6: *Blade-to-blade distributions of the turbulence intensity* $Tu = \sqrt{k_{2D}}/U_2$ *measured with PIV (—) and LDV (—) at flow rates of* Q_d *(left) and* $0.25Q_d$ *(right). a)* $r/R_2 = 0.65$*, b)* $r/R_2 = 0.90$*, c)* $r/R_2 = 0.98$*.*

with LDV. The reason for this discrepancy is not clear. A possible explanation is the fact that Tu, apart from a turbulent contribution, may include contributions of fluctuating velocity components arising from relative motion between the control volume and velocity gradients present in the flow. As noted by Hesse and Howard [47], this will result in a broadening of the probability density function of the velocity, which is falsely interpreted as turbulence. Due to different control volumes, the impact of this effect may differ between LDV and PIV, and thus lead to different turbulence intensities. However, since moving velocity gradients is a local phenomenon most likely to occur in regions with unsteady flow effects, it cannot fully explain the measured discrepancy in Tu in stable low-turbulent regions.

Unlike the design load observations at the two inner radial stations, the agreement between the two data sets at the outlet, $r/R_2 = 0.98$, is generally good. The large peaks in the PIV profile in the passage center and at the suction side surface may be attributed to image edge effects and slight variations in the position of the blade trailing edge in consecutive PIV images, respectively.

The level of agreement between the two data sets is maintained, or even improved, at the off-design condition, $0.25Q_d$. Ignoring the edge effects just mentioned, PIV predicts the same peak positions and magnitudes of turbulent intensity as LDV. In passage B, the values of Tu reach maxima of 9% and 14% at $r/R_2 = 0.90$ and $r/R_2 = 0.98$, respectively, indicating the presence of moving velocity gradients or unsteady flow effects associated with the motion of the relative eddy that pushes fluid backwards along the pressure side.

In conclusion, the comparative study of blade-to-blade distributions acquired by PIV and LDV shows that flow statistics calculated by ensemble averaging a large number of instantaneous PIV samples may, in effect, lead to results with an accuracy comparable to LDV, but at much reduced run times.

8.2.3 Mean line data

Based on the blade-to-blade distributions just presented, it is instructive to integrate the flow properties over circumferential planes of constant radii. This integration results in one-dimensional mean line data enabling the construction of velocity triangles which in a simple manner illustrate the flow development through the impeller passage. Using PIV data obtained at $z/b_2 = 0.5$, i.e. ignoring 3D effects, such velocity triangles are constructed below.

Integral averaging technique

When computing averages of a variable over a plane of interest, i.e. over the impeller exit area, caution has to be taken when selecting the averaging technique in order not to violate fundamental conservation laws. Japikse and Baines [55] provide an overview of the different approaches commonly used in turbomachinery. These approaches include the mass, momentum, energy and continuity-averages, which may be used in order to enforce the conservation of one or more of these properties. In the present study only the mass averaging technique has been employed. In this procedure the mean value of

a flow property, say P, is taken as the mass-weighted average

$$\bar{P} = \frac{\int P d\dot{m}}{\int d\dot{m}} = \frac{\int P C_r \, dS}{\int C_r \, dS} \tag{8.1}$$

where $d\dot{m} = \rho \vec{W} \cdot d\vec{S} = \rho C_r dS$ is the mass flow rate through the incremental stream tube in which the local property P is measured, S is the passage area, and it has been assumed that $\rho = const$. Following Eq. (8.1), mass-averaged radial and tangential velocities at radial stations ($r = const$) in the impeller have been calculated from

$$\bar{C}_r = \frac{1}{2\pi} \int_0^{2\pi} C_r \, d\theta \;\text{ and }\; \bar{C}_t = \frac{\int_0^{2\pi} C_t C_r \, d\theta}{\int_0^{2\pi} C_r \, d\theta}. \tag{8.2}$$

While the mass-averaged radial velocity $\bar{C}_r$ is identical to its area-averaged counterpart, this may certainly not be the case for $\bar{C}_t$. It can be formally shown that the mean velocities $\bar{C}_r$ and $\bar{C}_t$ in Eq. (8.2) ensure the conservation of mass and angular momentum at the plane of averaging. For example, integrating the angular momentum J over the passage area S gives

$$J = \int_S r C_t \, d\dot{m} = \int_S r C_t \rho C_r \, dS = \overline{rC_t} \dot{m} \tag{8.3}$$

or

$$\bar{C}_t = \frac{\int_S r C_t C_r \, dS}{\bar{r} \int_S C_r dS} \tag{8.4}$$

For $r = const$ this is seen to be identical to the expression given in Eq. (8.2).

Velocity triangles

Figure 8.7 shows the velocity triangles that result from mass-averaging the measured mid-height PIV velocity field in the circumferential direction across the passage. The velocity triangles are given at 5 radial stations between inlet and outlet and describe the mean line flow development at design load. At the inner radial station $r/R_2 = 0.39$, which corresponds to the leading edge of the impeller blade, the anticipated swirl component in the entry flow is evidenced, although the local magnitude of $\bar{C}_t$ is modest at design flow. Moving outwards through the passage, the dominating effect is the increase in the circumferential velocity $\vec{U}$ of the impeller which signifies the contribution of the centrifugal force to the static pressure rise. The magnitude of the relative velocity $\vec{W}$ decreases in the inner and central parts of the passage due to the diffuser effect of the passage but it then gains strength towards the outlet. Finally, the absolute velocity $\vec{C}$ grows steadily throughout the impeller and provides for a dynamic pressure rise.

Figure 8.8 shows two sets of velocity triangles and describes the mean line flow measured at quarter-load in passage A (left) and passage B (right), respectively. The collapsed appearance of the triangles compared to their equivalents at Q_d demonstrate the significant flow distortion present at off-design. As expected, the absolute velocity vector $\vec{C}$ deviates considerably from the radial direction at $r/R_2 = 0.39$ as a result of prerotation, i.e. upstream vorticity induced by the rotation of the impeller. Interestingly, the velocity triangles at $r/R_2 = 0.75$ are almost identical in spite of the

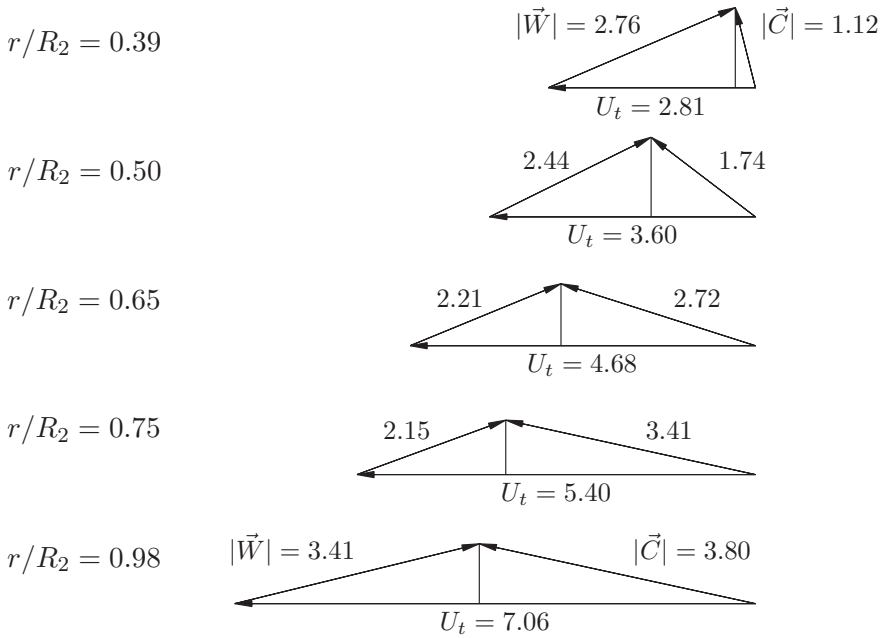

Figure 8.7: *Velocity triangles describing the mean line flow at five radial stations. Extracted from the mid-plane PIV data by mass-averaging mean velocities in the circumferential direction across the passage. ($Q/Q_d = 1.0$).*

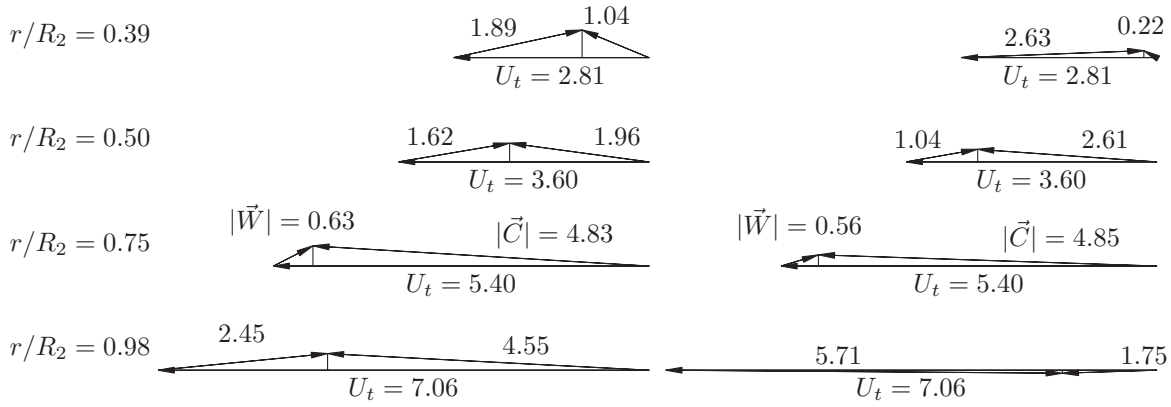

Figure 8.8: *Velocity triangles describing the mean line flow at four radial stations in passage A (left) and passage B (right). Extracted from the mid-plane PIV data by mass-averaging mean velocities across the passages. ($Q/Q_d = 0.25$).*

qualitatively different flow features observed in the two passages. At the outlet, however, the stall in passage B leads to a fully collapsed velocity triangle that even indicates a negative through-flow at the mid-plane, $z/b_2 = 0.50$, analyzed here.

Angular momentum parameter

As the experimental setup did not allow the direct measurement of the head produced by the test impeller, an angular momentum parameter $\psi = r\bar{C}_t/R_2U_2$ may be calculated from the mass-averaged tangential velocities [43]. The distribution of ψ between inlet and outlet is given in figure 8.9. A steady increase in angular momentum with radius is seen at design-load. At quarter-load, the stall in passage B manifests itself as a reversal in the angular momentum development, that first rises to a peak within the impeller, and then falls dramatically towards the outlet. A similar behavior was observed by Hamkins and Flack [43] in both shrouded and unshrouded impellers operating at reduced flow rates. They noted that for this trend to occur, the vanes must have reverse loading near the exit, as is indeed the case in passage B at $0.25Q_d$.

An estimate of the pressure rise expressed as meter head may be given by insertion of measured mean velocities in the Euler turbomachine equation, Eq. (5.10). This obviously entails profiles similar to the ones in figure 8.9, and predicts a total head rise of 2.6 m at design load, and 1.2 and 3.0 m in the quarter-load passages A and B, respectively. These values agree reasonably well with the head rise predicted from the affinity laws in section 6.3.4.

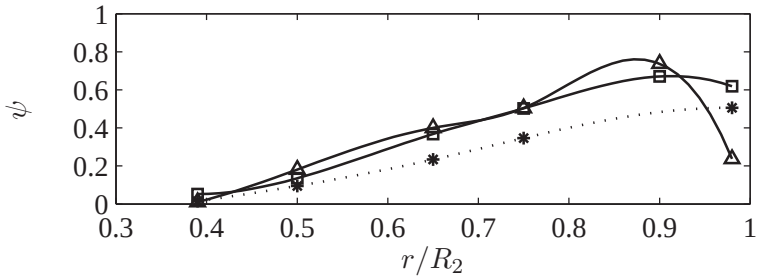

Figure 8.9: *Distribution of the angular momentum parameter $\psi = r\bar{C}_t/R_2U_2$ between impeller inlet and outlet. The dotted line indicates design flow Q_d and the unbroken lines passage A (square symbols) and passage B (triangular symbols) at quarter-load $0.25Q_d$, respectively.*

8.3 Three-dimensional effects

The previous analysis has concentrated solely on experimental observations in the mid-height plane, $z/b_2 = 0.50$. Although the geometry and the low specific speed of the impeller imply a flow not far from being two-dimensional, the data has suggested the presence of some three-dimensional effects, especially in the inlet region. This is also the indication of the contour plot of the divergence $\eta = \frac{\partial C_x}{\partial x} + \frac{\partial C_y}{\partial y}$ of the planar PIV data which is shown in figure 8.10.

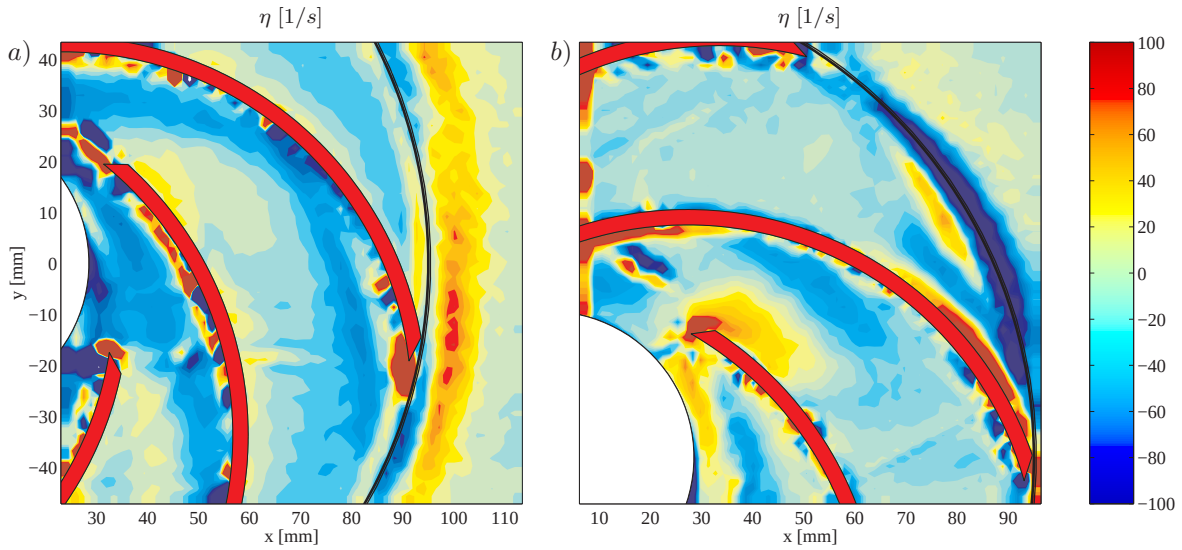

Figure 8.10: *Contour plot of the divergence* $\eta = \frac{\partial C_x}{\partial x} + \frac{\partial C_y}{\partial y}$ *of the planar PIV velocity field. a) Design load* $Q/Q_d = 1.0$ *b) Quarter-load* $Q/Q_d = 0.25$.

Figure 8.10 reveals values of η departing considerably from zero in the inner parts of the impeller at both design and off-design conditions, suggesting fluid movement in the spanwise direction perpendicular to the measurement plane. To elaborate, contour plots of the flow quantities at circumferential surfaces of constant radius are investigated in the following. The plots are based on LDV data taken at 5 to 10 axial positions, depending on the local passage height.

Figure 8.11 shows the mean radial and tangential velocities measured at design flow. It confirms the three-dimensionality of the flow at the inner radial stations due to the meridional curvature of the axial-to-radial bend in the entry section. At $r/R_2 = 0.65$, high-momentum fluid is concentrated in the hub-suction side corner, but further downstream it moves to the vicinity of the curved shroud wall. In figure 8.11, apparent discontinuities exist near the hub plate at most radial stations. This illustrates the experimental difficulties associated with measurements very close to the hub and shroud surfaces. Apart from these near-wall effects, the spanwise variations reduces towards the impeller exit.

Figure 8.12 gives the distributions of $\langle C_r \rangle / U_2$ measured at $0.25Q_d$. At the inlet of the unstalled passage A, large gradients of the radial velocity are directed towards the shroud-suction side corner. For passage B, the nearly vertical contour lines at the two inner radial stations indicate that the relative eddy is essentially a two-dimensional flow phenomenon. At $r/R_2 = 0.90$, the reversed flow along the pressure side is seen to cover the entire pressure surface, whereas the exit stations $r/R_2 = \{0.98, 1.01\}$, figures 8.12c and d, reveal the creation of a pressure-surface passage vortex, that sits close to the shroud and grows rapidly after leaving the impeller. The strength of this outward component was only indicated in the mid-height blade-to-blade distributions shown earlier in figure 8.5.

Contour plots of $\langle W_t \rangle$ at $0.25Q_d$ are not shown, as they reveal no significant three-dimensional effects. In general it is concluded from a close analysis of hub-to-shroud distributions of various flow quantities that although significant spanwise variations

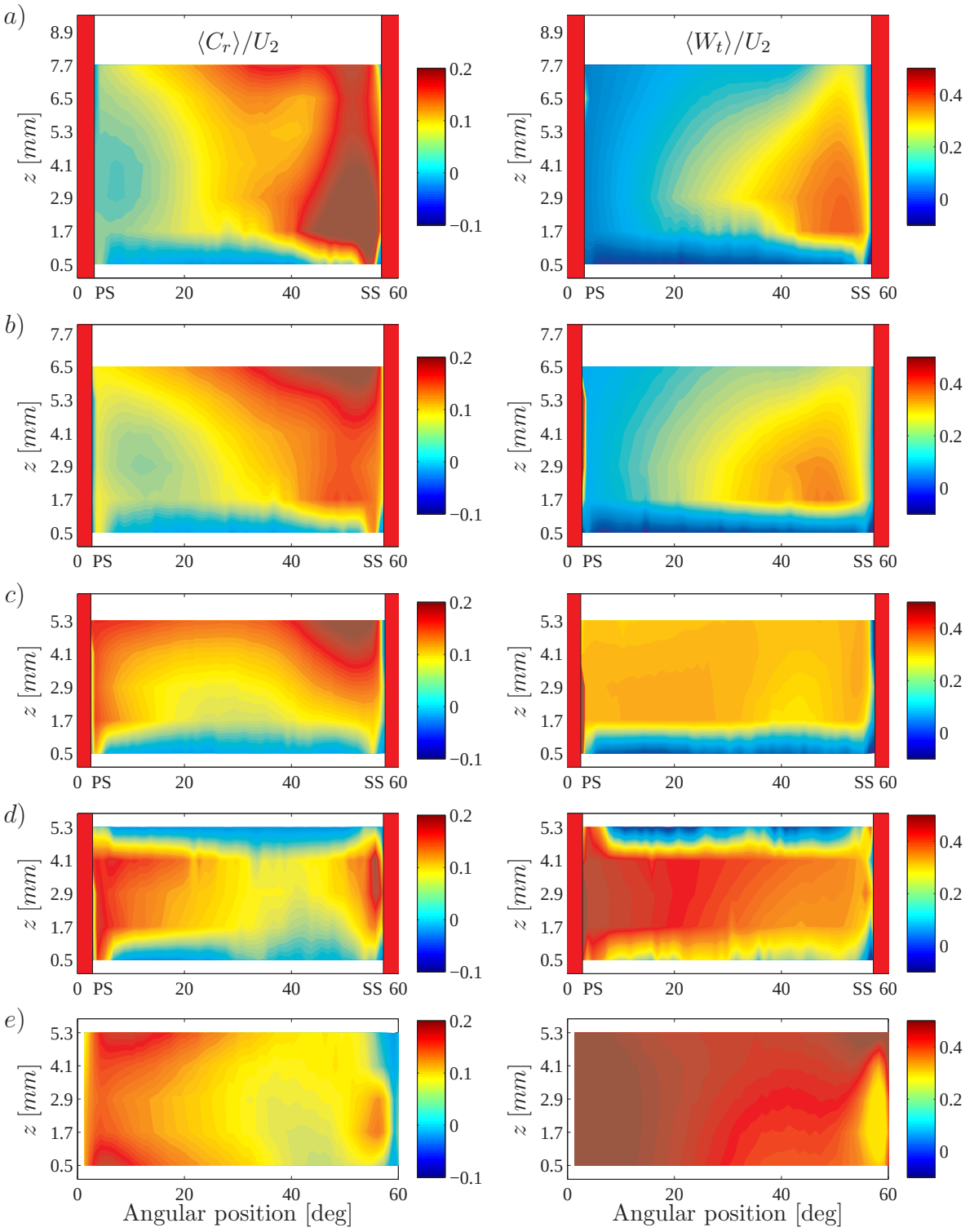

Figure 8.11: *Mean radial velocity $\langle C_r \rangle / U_2$ (left) and tangential velocity $\langle W_t \rangle / U_2$ (right) measured with LDV at circumferential surfaces of constant radii. a) $r/R_2 = 0.65$, b) $r/R_2 = 0.75$, c) $r/R_2 = 0.90$, d) $r/R_2 = 0.98$, e) $r/R_2 = 1.01$. ($Q/Q_d = 1.0$).*

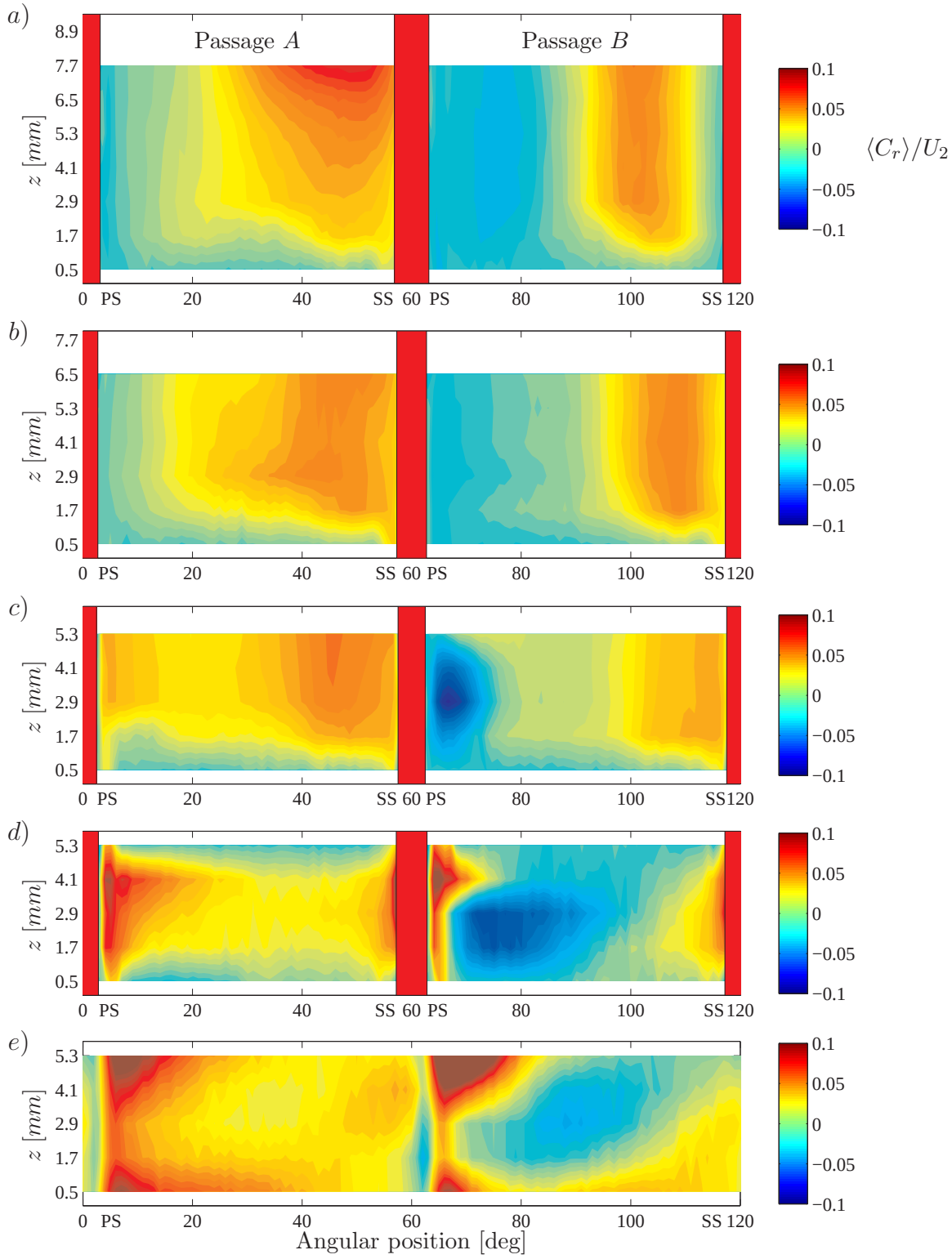

Figure 8.12: *Mean radial velocity $\langle C_r \rangle / U_2$ measured with LDV at circumferential surfaces of constant radii. a) $r/R_2 = 0.65$, b) $r/R_2 = 0.75$, c) $r/R_2 = 0.90$, d) $r/R_2 = 0.98$, e) $r/R_2 = 1.01$. $(Q/Q_d = 0.25)$.*

exist in the inlet section, the remaining parts of the impeller flow are well described by a two-dimensional approach. This is reflected in the fact that the figures 8.11 and 8.12 overall confirm the quantitative flow characteristics deduced from the mid-plane data in the previous sections. It may be remarked that the local three-dimensional effects that were indeed observed were not confined to part-load conditions, but existed in equal extent at design-load.

8.4 Comparison with LES

The present experimental data have demonstrated that improved insight into complex time-varying flow fields may be gained from advancing from a one-point mean technique to a multi-point instantaneous technique. In the field of computational fluid dynamics, a parallel or even larger potential may be associated with the shift from steady-state simulations based on RANS turbulence modeling to three-dimensional time-dependent Large Eddy Simulations (LES). Traditionally, LES has been confined to building-block type flows such as channel flows, boundary layers and transition scenario, and the technique has only recently started to find use in industrial applications. In the field of turbomachinery, Revstedt [100] as well as Song and Chen [110] and Chen et al. [21] predicted the flow around Francis turbines by LES, and Kato et al. [59] reported a LES in a mixed-flow pump. With these rare exceptions, the experience with LES in complex geometries is still limited, and some scepticism therefore exists on the maturity of present methods.

In an effort to investigate the applicability of the LES technique to centrifugal impellers, Byskov [18, 17] recently performed LES predictions of the present impeller flow. The purpose was to assess the accuracy and contributions obtainable from LES, relative to traditional RANS turbulence models, by comparing the numerical results with the present LDV and PIV data base. Since the LES data may be regarded as the numerical counterpart of PIV, a brief extract of the results obtained by Byskov [18] is presented below.

8.4.1 LES setup

The Large Eddy Simulations were performed in the commercial CFD code FINE/Turbo which is a time-marching finite volume Navier-Stokes solver [63] based on solving the three-dimensional compressible continuity, Navier-Stokes and energy equations. A pseudo-compressibility method and a second-order dual-time stepping procedure [42] allowing for simulating incompressible unsteady flows were applied. For details on the numerical solution procedures, the reader is referred to Byskov [18, 17].

The effect of the subgrid-scales were modeled through a localized dynamic Smagorinsky model [95]. In this model the SGS-viscosity ν_{sgs} is given by $\nu_{sgs} = C\Delta^2 \left|\bar{S}_{ij}\right|$ where C is the dynamically computed model parameter, Δ the filter length related to the local cell volume $\Delta = V^{1/3}$ and S_{ij} is the strain rate tensor. The model is referred to as localized as it does not require averaging of the model parameter in directions of homogeneity. For reasons of stability the SGS-viscosity was constrained to be non-negative and the model parameter was not allowed to exceed a value of 1. In the finite

volume approach applied, the numerical discretization was interpreted as an implicit filter.

Based on the experimentally observed correlation between at least every second passage, only two of the six impeller passages were included in the numerical model. A mesh of totally 385.000 cells with roughly 150.000 cells in each impeller passage was utilized, see figure 8.13. The first cell point was located 1–5 μm off the surface, corresponding to y^+ values less than 5.0 on the average.

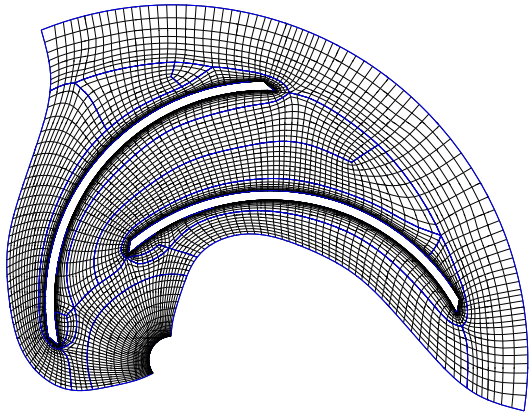

Figure 8.13: *Cross-sectional view of the mesh structure used in the LES [18] of the CR4 impeller.*

The specification of physically correct turbulent inflow conditions is of general importance in LES. Due to the experimental difficulties associated with the measurement of impeller inflow conditions, a data base consisting of time-dependent velocity profiles from a turbulent channel flow simulation was utilized, and the influence of prerotation thus disregarded. The boundary conditions imposed were uniform pressure at the outlet, no-slip at the solid walls and periodicity in the circumferential direction. The time step was $5 \cdot 10^{-3}$s, equivalent to 160 time steps per impeller revolution, which ensured an average *CFL* number less than one. The flow field was allowed to develop for 2000 time steps before time averaged quantities were collected during 2000 additional time steps, sufficient to stabilize lower order statistics. The simulations were carried out on a single Alpha EV6 500 MHz processor of a COMPAQ AlphaServer DS20 and the total CPU time was about 960 hours for one operating condition [18].

8.4.2 LES results

Figure 8.14 shows the time averaged relative velocity field $\langle \vec{W} \rangle$ predicted by LES. In agreement with the PIV and LDV vector plots given in figures 7.1 and 7.3, the simulations show a well-behaved flow with a low-velocity zone present on the blade pressure side. This non-separated design flow was, however, also well predicted by steady state Baldwin-Lomax and Chien $k-\varepsilon$ simulations, and the slightly better accuracy obtained by LES might not justify the substantial additional computational effort.

The quarter-load condition represents a much more severe test for a numerical flow solver. Figure 8.15 shows the results obtained with LES at $0.25Q_d$. Although the LES results do show substantial deviations from the measurements in passage A, probably because of different inlet conditions, LES predicts with a remarkable accuracy both the

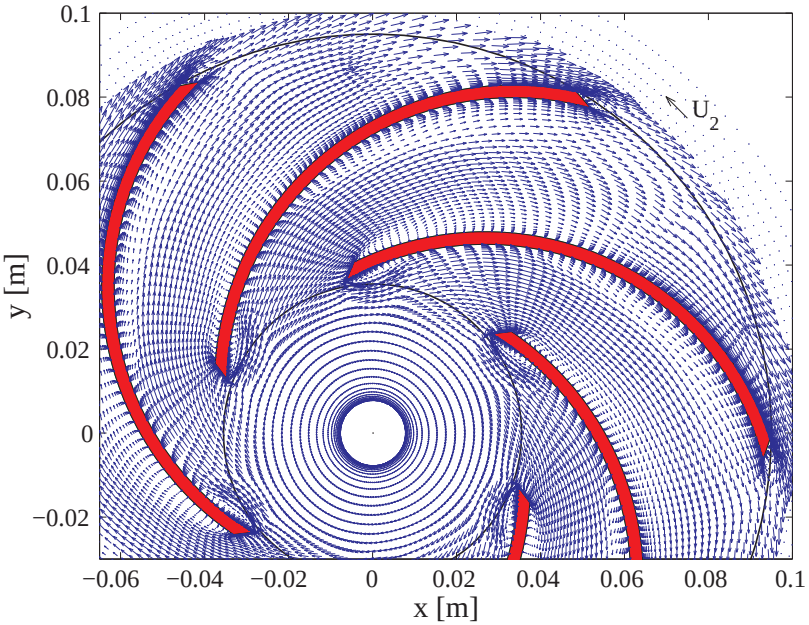

Figure 8.14: *Time averaged velocity field $\langle \vec{W} \rangle$ in the impeller mid-height, $z/b_2 = 0.5$, predicted by LES [18]. $(Q/Q_d = 1.0)$.*

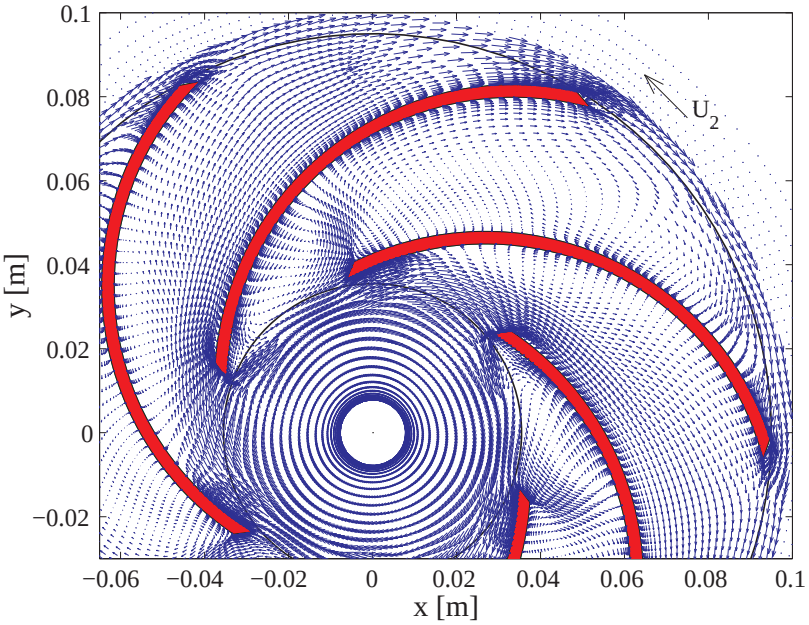

Figure 8.15: *Time averaged velocity field $\langle \vec{W} \rangle$ in the impeller mid-height, $z/b_2 = 0.5$, predicted by LES [18]. $(Q/Q_d = 0.25)$.*

inlet stall cell in passage B and the flow reversal along the pressure side. In contrast, the RANS models did not capture the stationary stall in passage B, but predicted identical non-separated flows in both passages and consequently provided an inaccurate prediction of the local flow behavior. Based on quantitative comparisons with the present PIV and LDV data, it was thus concluded by Byskov [18] that LES, especially at off-design, provides an improved insight into the basic fluid dynamic phenomena occurring in a centrifugal pump impeller.

8.5 Summary

In this chapter a quantitative study of blade-to-blade distributions extracted from the PIV data was performed, providing additional insight into local flow features. Among other features, the strength of the inlet stall cell leading to a reduced through-flow in passage B was revealed. Comparisons with LDV mean data showed a satisfactory agreement, although some discrepancies were observed. Overall, however, it was concluded that the accuracy of flow statistics calculated by ensemble averaging a large number of instantaneous PIV samples is indeed comparable to LDV. A significant advantage of using the PIV technique over LDV is the considerably reduced run times and the additional ability to identify instantaneous spatial flow structures.

To visualize the mean line flow development through the impeller, velocity triangles were constructed, based on mass-averaged velocities at different radial stations. This also allowed an estimate of the head produced by the impeller which agreed reasonably well with the value predicted by the pump scaling laws.

An analysis of hub-to-shroud distributions of various flow quantities revealed that although significant spanwise variations exist in the inlet section, the remaining parts of the impeller flow is well described by a two-dimensional approach.

Finally, the potential use of the present experimental data base as a means for validating CFD simulations *a posteriori* was demonstrated trough a condensed description of the promising result obtained by Byskov [18] in a recent Large Eddy Simulation of the present impeller flow. In contrast to traditional RANS turbulence models, the time-dependent LES predicted the same 'two-channel' phenomenon as observed in the present study. It remains to analyze instantaneous PIV and LES snapshots for higher-order statistics.

Chapter 9

Conclusions

The work presented in this dissertation was devoted to the application of the non-intrusive optical measurement technique, Particle Image Velocimetry (PIV), to two physically complex flows of engineering relevancy. The focus was on an investigation of the internal flow in a centrifugal pump impeller. This was motivated by the quest for more detailed knowledge of the local and instantaneous flow features in order to improve efficiencies and make the pump less sensitive to off-design operation.

Since the application of PIV to this industrial flow represents a challenging application, a feasibility study of the PIV technique in a geometrically simple, yet physically complex flow was performed first. The unsteady flow past a cylinder of square cross-section was chosen as test case, as the physics of this flow involves phenomena like separation, recirculation and large-scale turbulent coherent structures, similar to those encountered in pump impellers. Furthermore, this flow was well-suited to demonstrate the use of PIV data as a tool for an *apriori* evaluation of Large Eddy Simulations (LES) which may be considered the numerical counterpart of PIV.

Following this feasibility study, the main part of the dissertation concerned the application of PIV to the rotating passages of a centrifugal pump impeller of industrial design. The main objective was to investigate steady and unsteady flow phenomena occurring at severe off-design conditions. In the following, the main results obtained in each of the two applications are summarized.

9.1 Square cylinder

A statistically large number of conditionally sampled velocity vector maps were collected in the flow past a square cylinder in uniform cross-flow at four equidistant phases of the vortex shedding cycle. Both large and small scales of the flow were resolved. Measurements in the near wake behind the cylinder confirmed that the flow is not only temporally but also spatially extremely complex with direct interaction between the two separated shear layers. Measurements of the recirculation zone that forms on the cylinder side because of flow separation at the leading edge revealed a periodic flapping of the shear layer. Ensemble averaged statistics calculated at each phase showed good qualitative agreement with previous experimental and numerical investigations. The present PIV setup allowed measurements 1–3 millimeters from the faces of the cylinder which is closer than previous experimental investigations.

Based on the PIV data base, an experimental *a priori* test of five subgrid-scale (SGS) models used in Large Eddy Simulations of turbulent flows was performed. The study compared the measured instantaneous SGS stresses and SGS dissipation with the model predictions, and confirmed previous findings that eddy viscosity models cannot reproduce the details of the stresses and energy exchange very accurately on a local and instantaneous level. However, model coefficients deduced from the experimental data indicated that the Smagorinsky model, despite this incorrect local behavior, still predicts the global dissipation fairly accurately. Mixed and dynamic models based on similarity between scales proved better at reproducing the instantaneous details of the SGS physics. The results suggest that the presence of large-scale coherent structures strongly affects the distribution of subgrid-scale stresses and dissipation. Overall, the results are consistent with previous findings in simpler flows based on both experimental and DNS data, only now confirmed in a more complex flow.

This part of the study demonstrated that the PIV technique may provide valuable information on a complex unsteady flow at a variety of levels. Apart from a direct insight into the instantaneous spatial structures, reliable turbulence statistics as well as subgrid-scale quantities usable for SGS model evaluation may be deduced from a large ensemble of conditionally sampled vector maps.

9.2 Centrifugal pump impeller

The main part of the work concerned the application of PIV to the rotating passages of a pump impeller. The impeller under investigation was a medium specific-speed centrifugal pump impeller of industrial design, the Grundfos CR4. In order to allow optical access, the present measurements were undertaken in a specially designed test rig with a scaled impeller manufactured entirely in perspex. The experimental operating conditions were determined from the affinity laws to ensure flow similarity between the model and the original impeller. The experimental setup and technique proved to be efficient in providing reliable and detailed data over a full blade passage, also in the close vicinity of walls due to the use of fluorescent seeding.

Measurements performed at the design operating point, $Q = Q_d$, showed a well-behaved vane congruent flow with no separation occurring, and revealed a distinct flow congruence between all six passages. The flow was dominated by rotational effects apart from local curvature effects in the inlet section.

The main focus of the investigation was to identify steady and unsteady flow features at severe off-design conditions. At a flow rate of $Q = 0.25Q_d$, a previously unreported steady 'two-channel' phenomenon consisting of alternate stalled and unstalled passages was observed, with distinct flow congruence between every second passage. A large high-turbulent recirculation cell blocked the inlet to the stalled passage and a strong relative eddy dominated the remaining parts of the passage causing backflow along the blade pressure side at large radii. This may be viewed as a quasi-inviscid behavior due to the dominating effect of the potential flow characteristics over viscous effects.

The detected stall phenomenon is steady and non-rotating. This may be due to the even number of vanes and the fact that the stall is not initiated via the interaction with any stationary components. In these respects, the present stall phenomenon differs from

the periodic unsteadiness of the relative flow known as rotating stall, which typically moves in the direction of rotation at a lower speed than that of the impeller.

A qualitative study of the spatial flow structures associated with rotor-stator interaction was performed by installing a vaned diffuser with 11 straight vanes in the test rig. This highlighted the influence of impeller blade orientation on the flow and revealed considerable cyclic variations. The 'two-channel' stall phenomenon detected at part-load was not significantly influenced by the presence of the diffuser.

A quantitative study of blade-to-blade distributions extracted from the PIV data was performed, providing additional insight into local flow features. Comparisons with LDV mean data showed a satisfactory agreement, although some discrepancies were observed. Overall, however, it was concluded that the accuracy of flow statistics calculated by ensemble averaging a large number of instantaneous PIV samples is indeed comparable to LDV. A significant advantage of using the PIV technique over LDV is the considerably reduced run times and the additional ability to identify instantaneous spatial flow structures.

Based on LDV data, an analysis of hub-to-shroud distributions of various flow quantities revealed that although significant spanwise variations exist in the inlet section, the remaining parts of the impeller flow is well described by a two-dimensional approach.

Finally, the potential use of the present experimental data base as a means for validating CFD simulations *a posteriori* was demonstrated trough comparisons with result obtained by Byskov [18] in a recent Large Eddy Simulation of the present impeller flow. In contrast to traditional RANS turbulence models, the time-dependent LES predicted the same 'two-channel' phenomenon as observed in the present study.

9.3 Perspectives

The successful application of PIV to a centrifugal impeller of industrial design opens promising perspectives for the use of this experimental technique in the design of pumps. Nevertheless, many unanswered questions still need to be addressed before PIV may be fully incorporated into the design cycle. One important practical problem is the issue of providing optical access which was accomplished in the present work by performing the experiments in an isolated impeller mounted in a specially designed test rig. For design purposes it is desired to incorporate both rotor and stator stages in order to capture all details of the flow distortion induced by rotor-stator interaction, and this requires special remedies for providing optical access and sufficient seeding density. However, as many of these issues are shared with LDV which is routinely used in industry, the extension to PIV seems feasible.

The present study focused, to a large extent, on qualitative comparisons. It remains to analyze instantaneous PIV snapshots for higher-order statistics. In general, the presented results represent only a fraction of the information stored in the present PIV data base. The ability to acquire an enormous amount of data in a very short time underlines the need for new methods to reduce, visualize and interpret data. Such methods are currently under development, e.g. Proper Orthogonal Decomposition. Along with the rapid developments of lasers, CCD cameras and computers, it is unquestionable that PIV will find increased use in industrial applications in the future.

Nomenclature

Latin

b	Axial height of impeller blade
c_r	Optimum particle image width, $c_r = d_t/d_r$
C	Particle concentration
C	Absolute velocity
C	Model coefficient in subgrid-scale model
C_t	Absolute circumferential velocity
D_1	Inlet diameter
D_2	Outlet diameter
d_I	Size of interrogation area in object plane
d_p	Particle diameter
d_r	Pixel size
d_s	Diffraction-limited particle image diameter
d_t	Recorded particle image diameter
D	Cylinder side length
D	Impeller diameter
D_a	Aperture diameter
D_I	Size of interrogation area in image plane
DSR	Dynamic spatial range
DVR	Dynamic velocity range
f	Frequency
f	Focal length
$f^{\#}$	Numerical aperture (f-number) of recording lens
f_c	Cut-off frequency
f_s	Shedding frequency
$\mathcal{F}$	Fourier transform
g	Gravity
G	Filter function
H	Cylinder height
H	Head
i	Grid index in x-direction
I_1, I_2	Light intensities
IA	Interrogation area
j	Grid index in y-direction
k_{2D}	2D portion of turbulent kinetic energy
k_D	Geometric scale factor

k_n	Kinematic scale factor
l_i	Integral scale
L_r	Length of time-mean recirculation zone
L_u	Streamwise separation of streamwise vortices
L_x	Format of recording medium
$\mathcal{L}_{ij}$	Resolved turbulent stresses
m	Mass
$\dot{m}$	Mass flow rate
M	Magnification factor
n	Revolutions per minute
N	Number of vector maps
$\mathcal{N}_I$	Image density
N_s	Specific speed
N_S	Source density
p^*	Rotary stagnation pressure
P	Power
Q	Volume flow rate
r, R	Radius
R	Density ratio, $R = \rho_p/\rho_f$
R_2	Outlet radius
R_n	Radius of curvature of blade-to-blade section
R_m	Radius of curvature of meridional section
Re	Reynolds number
Ro	Rossby number
s	Standard deviation
S	Surface area
S, S_0, S_ε	Stokes' numbers
S_{ij}	Strain rate tensor
St	Strouhal number
t	Blade thickness
T	Torque
T_s	Shedding period
Tu	Turbulence intensity
u	Velocity component in x-direction
u_f	Fluid velocity
u_p	Particle velocity
U	Circumferential velocity
U_2	Circumferential velocity at impeller outlet
U_c	Convection velocity
U_z	Axial velocity
U_∞	Bulk flow velocity
v	Velocity component in y-direction
w	Velocity component in z-direction
W	Relative velocity
W_r	Relative radial velocity
W_t	Relative circumferential velocity

y^+	Non-dimensional wall distance
z	Axial position
z_c	Confidence factor
Z_i	Number of impeller blades
Z_d	Number of diffuser vanes

Greek

α	Absolute flow angle
β	Relative flow angle
Γ	Circulation
δ	Vector spacing
δz	Focal depth of recording lens
Δ	LES filter width
$\Delta\vec{C}$	Cyclic velocity
Δt	Time between illumination pulses
Δu	Slip velocity between particle and fluid
$\Delta\vec{X}$	Particle image displacement
Δz_0	Light sheet thickness
ϵ	Dissipation rate
ϵ_{SGS}	Subgrid-scale dissipation
ϵ_t	Total measurement error
η	Kolmogorov scale
η	Two-dimensional divergence
λ	Laser light wavelength
λ	Taylor scale
μ	Dynamic viscosity
ν	Kinematic viscosity
ν_{sgs}	Subgrid-scale kinematic viscosity
Π	Energy-flux from resolved to unresolved scales, $\Pi = -\langle\epsilon_{SGS}\rangle$
ρ	Density
ρ	Correlation coefficient
τ_{ij}	Subgrid-scale stress tensor
τ_p	Relaxation time
ϕ	Flow coefficient
Φ	Discrete spatial cross-correlation
ψ	Angular momentum parameter
ψ	Stream function
Ψ	Head coefficient
ω	Angular velocity
$\vec{\Omega}$	Vorticity vector
Ω_z	Out-of-plane vorticity component

Sub scripts

$_1$	Inlet section
$_2$	Outlet section
$_d$	Design flow
$_f$	Fluid
$_N$	Normal mode
$_p$	Particle
$_{SGS}$	Subgrid-scale
$_Z$	Zoom mode

Super scripts

$'$	Temporal or spatial fluctuation
$^+$	Wall units

Abbreviations

CCD	Charge Coupled Device
CFD	Computational Fluid Dynamics
DNS	Direct Numerical Simulation
DMX	Dynamic Mixed Model
DSM	Dynamic Smagorinsky Model
DPIV	Digital Particle Image Velocimetry
LDV	Laser Doppler Velocimetry
LES	Large Eddy Simulation
MX	Mixed Model
PIV	Particle Image Velocimetry
PS	Pressure side of impeller blade
RANS	Reynolds Averaged Navier-Stokes
SGS	Subgrid-scale
SM	Smagorinsky Model
SS	Scale-similarity Model
SS	Suction side of impeller blade

Bibliography

[1] M. Abramian and J.H.G. Howard. Experimental investigation of the steady and unsteady relative flow in a model centrifugal impeller passage. *J. of Turbomachinery*, 116:269–279, 1994.

[2] R.J. Adrian. Scattering particle characteristics and their effect on pulsed laser measurements of fluid flow; speckle velocimetry vs particle image velocimetry. *Appl. Optics*, 23(11):1690–1691, 1984.

[3] R.J. Adrian. Particle-imaging techniques for experimental fluid mechanics. *Ann. Rev. Fluid Mech.*, 23:261–304, 1991.

[4] R.J. Adrian. Dynamic ranges of velocity and spatial resolution of particle image velocimetry. *Meas. Sci. Technology*, 8:1393–1398, 1997.

[5] J.C. Agüí and J. Jiménez. On the performance of particle tracking. *J. Fluid Mech.*, 185:447–468, 1987.

[6] A. Akhras, M. El Hajem, R. Morel, and J.Y. Champagne. The internal flow investigation of a centrifugal pump. In *10th Intl. Symp. on Appl. Laser Techniques to Fluid Mechanics*, pages 28.5.1–28.5.9, Lisbon, Portugal, July 2000.

[7] O. Akin and D. Rockwell. Flow structure in a radial flow pumping system using high-image-density Particle Image Velocimetry. *J. Fluids Engng.*, 116:538–544, 1994.

[8] S. Aramaki and H. Hayami. Unsteady flow measurement in a rotating impeller using PIV. In *Proceedings of the 3rd International Workshop on PIV*, Santa Barbara, California, USA, 16-18 September 1999.

[9] N. Arndt, A.J. Acosta, C.E. Brennen, and T.K. Caughey. Experimental investigation of rotor-stator interaction in a centrifugal pump with several vaned diffusers. *J. of Turbomachinery*, 112:98–108, 1990.

[10] J. Bardina, J.H. Ferziger, and W.C. Reynolds. Improved subgrid-scale models for large-eddy simulation. Technical Report 80-1357, AIAA, 1980.

[11] R.J. Beaudoin, S.M. Miner, and R.D. Flack. Laser velocimeter measurements in a centrifugal pump with a synchronously orbiting impeller. *J. of Turbomachinery*, 114:340–439, 1992.

[12] J.S. Bendat and A.G. Piersol. *Random Data: Analysis and Measurement Procedures*. John Wiley & Sons, New York, 1971.

[13] P. Bradshaw. Effects of streamline curvature on turbulent flow. *AGARDograph*, 169, 1973.

[14] R. van den Braembussche. Description of secondary flows in radial flow machines. In A.S. Ucer, P. Stow, and Ch. Hirsch, editors, *Thermodynamics and Fluid Mechanics of Turbomachinery*, volume II of *NATO ASI Series*, pages 665–684. 1985.

[15] C.E. Brennen. *Hydrodynamics of Pumps*. Concepts ETI, Inc. and Oxford University Press, 1994.

[16] P. Buchhave, W.K. George, and J.L. Lumley. The measurement of turbulence with the laser-doppler anemometer. *Ann. Rev. Fluid Mech.*, 11:443–503, 1979.

[17] R. K. Byskov. *Large Eddy Simulation of Flow Structures in a Centrifugal Pump Impeller. Part 2: Code Validation*. PhD thesis, Aalborg University, Institute of Energy Technology, Aalborg, Denmark, 2000.

[18] R. K. Byskov. *Large Eddy Simulation of Flow Structures in a Centrifugal Pump Impeller. Part 1: Theory and Simulation of Pump Flow*. PhD thesis, Aalborg University, Institute of Energy Technology, Aalborg, Denmark, 2000.

[19] R.K. Byskov and N. Pedersen. Large Eddy Simulation of Unsteady Flow in Pump Impeller. Master's thesis, Aalborg University, Aalborg, Denmark, June 1997. (In danish).

[20] B.T. Chao. Turbulent transport behaviour of small particles in a turbulent fluid. *Österreichisches Ingenieur-Archiv*, 18:7, 1964.

[21] X Chen, Ch. C. S. Song, K. Tani, K. Shinmei, K. Niikura, and J. Sato. Comprehensive modeling of francis turbine system by large eddy simulation approach. In H. Brekke, C. G. Duan, R. K. Fisher, R. Schilling, S. K. Tan, and S. H. Winnoto, editors, *Hydraulic Machinary and Cavitation*, volume 1, pages 236–244. XIX IAHR Symposium, World Scientific Publishing Co., 1998.

[22] S. Chu, R. Dong, and J. Katz. Relationship between unsteady flow, pressure fluctuations, and noise in a centrifugal pump - Part A: Use of PDV data to compute the pressure field. *J. Fluids Engng.*, 117:24–29, 1995.

[23] S. Chu, R. Dong, and J. Katz. Relationship between unsteady flow, pressure fluctuations, and noise in a centrifugal pump - Part B: Effects of blade-tongue interactions. *J. Fluids Engng.*, 117:30–35, 1995.

[24] R.A. Clark, J.H. Ferziger, and W.C. Reynolds. Evaluation of subgrid-scale models using an accurately simulated turbulent flow. *J. Fluid Mech.*, 91:1, 1979.

[25] G.T. Csanady. *Theory of Turbomachines*. McGraw-Hill, 1964.

[26] R. Dean and Y. Senoo. Rotating wakes in vaneless diffusers. *J. of Basic Engineering*, 82:563–574, 1961.

[27] R. Dong, S. Chu, and J. Katz. Quantitative visualization of the flow within the volute of a centrifugal pump. Part A: Technique. *J. Fluids Engng.*, 114: 390–395, 1992.

[28] R. Dong, S. Chu, and J. Katz. Quantitative visualization of the flow within the volute of a centrifugal pump. Part B: Results and analysis. *J. Fluids Engng.*, 114:396–403, 1992.

[29] R.P. Dring, H.D. Joslyn, L.W. Hardin, and J.H. Wagner. Turbine rotor-stator interaction. *J. Eng. Power*, 104:729–742, 1982.

[30] D.F.G. Durao, M.V. Heitor, and J.C.F. Pereira. Measurements of turbulent and periodic flows around a square cross-section cylinder. *Exp. Fluids*, 6: 298–304, 1988.

[31] D. Eckardt. Detailed flow investigations within a high-speed centrifugal compressor impeller. *J. Fluids Engng.*, 98:390–402, 1976.

[32] K. Eisele, Z. Zhang, and M.V. Casey. Flow analysis in a pump diffuser - Part 1: LDA and PTV measurements of the unsteady flow. *J. of Turbomachinery*, 119:968–977, 1997.

[33] T.Z. Farge and M.W. Johnson. Effect of flow rate on loss mechanisms in a backswept centrifugal impeller. *Int. J. Heat and Fluid Flow*, 13(2):189–196, 1992.

[34] K. Fischer and D. Thoma. Investigation of the flow conditions in a centrifugal pump. *Trans. ASME*, 54:141, 1932. Paper No. HYD-54-8.

[35] D.J. Forliti, P.J. Strykowski, and K. Debatin. Bias and precision errors of digital particle image velocimetry. *Exp. Fluids*, 28:436–447, 2000.

[36] H.S. Fowler. The distribution and stability of flow in a rotating channel. *J. Eng. Power*, pages 229–236, 1968.

[37] R. W. Fox and A. T. McDonald. *Introduction to fluid mechanics*. Wiley, 4th edition, 1994.

[38] M. Germano, U. Piomelli, P. Moin, and W.H. Cabot. A dynamic subgrid-scale eddy viscosity model. *Phys. Fluids.*, A3(7):1760–1765, 1991.

[39] I. Grant. Particle image velocimetry: a review. *Proc Instn Mech Engrs*, 211 (C):55–76, 1997.

[40] Grundfos A/S. WinCAPS Catalogue, Ver 7.0. Product No: 41260001 CR4-20/1.

[41] M. Hajem, R. Morel, J.Y. Champagne, and F. Spettel. Detailed measurements of the internal flow of a backswept centrifugal impeller. In *9th Intl. Symp. on Appl. of Laser Techniques to Fluid Mechanics*, pages 36.2.1–36.2.6, Lisbon, Portugal, July 1998.

[42] N. Hakimi. *Preconditioning Methods for Time Dependent Navier-Stokes Euations. Application to Environmental and Low Speed Flows.* PhD thesis, Dept. of fluid Mechanics. Vrije Universiteit, Brussel, Belgium, 1997.

[43] C.P. Hamkins and R.D. Flack. Laser velocimeter measurements in shrouded and unshrouded radial flow pump impellers. *J. of Turbomachinery*, 109:70–76, 1987.

[44] D.P. Hart. PIV error correction. *Exp. Fluids*, 29:13–22, 2000.

[45] W.R. Hawthorne. Secondary vorticity in stratified compressible fluids in rotating systems. Technical report, CUED/A-Turbo/TR 63, Cambridge Univ., Eng. Dept., U.K., 1974.

[46] H. Hayami, S. Aramaki, and Y. Watanabe. PC-PIV system for a measurement of relative flow in a rotating impeller impeller. In *The Second International Workshop on PIV'97-Fukui*, pages 105–108, Fukui, Japan, July 1997.

[47] N.H. Hesse and J.H.G. Howard. Experimental investigation of blade loading effects at design flow in rotating passages of centrifugal impellers. *J. Fluids Engng.*, 121:813–823, 1999.

[48] C. Hirsch, S. Kang, and G. Pointel. A numerically supported investigation of the 3D flow in centrifugal impellers. Part II: Secondary flow structure. In *Intl. Gas Turbine and Aeroengine Congress & Exhibition*, Birmingham, UK, 1996.

[49] A.T. Hjelmfelt and L.F. Mockros. Motion of discrete particles in a turbulent fluid. *App. Sci. Res.*, 16:149–161, 1966.

[50] H. Huang, D. Dabiri, and M. Gharib. On errors of digital particle image velocimetry. *Meas. Sci. Technology*, 8:1427–1440, 1997.

[51] J.A.C. Humphrey, A.M.K. Taylor, and J.H. Whitelaw. Laminar flow in a square duct of strong curvature. *J. Fluid Mech.*, 83(3):509–527, 1977.

[52] J.A.C. Humphrey, J.H. Whitelaw, and G. Yee. Turbulent flow in a square duct of strong curvature. *J. Fluid Mech.*, 103:443–463, 1981.

[53] A.K.M.F. Hussain and M. Hayakawa. Eduction of large-scale organized structures in a turbulent plane wake. *J. Fluid Mech.*, 180:193–229, 1987.

[54] K. Imaichi and K. Ohmi. Numerical processing of flow-visualization pictures - measurement of two-dimensional vortex flow. *J. Fluid Mech.*, 129:283–311, 1983.

[55] D. Japikse and N.C. Baines. *Introduction to Turbomachinery.* Concepts ETI, Inc. and Oxford University Press, 1994.

[56] M.W. Johnson. Secondary flow in rotating bends. *J. Eng. Power*, 100:553–560, 1978.

[57] M.W. Johnson and J. Moore. The influence of flow rate on the wake in a centrifugal impeller. *J. Eng. Power*, 105:33–39, 1983.

[58] M.W. Johnson and J. Moore. Secondary flow mixing losses in a centrifugal impeller. *J. Eng. Power*, 105:24–32, 1983.

[59] C. Kato, H. Shimizu, and T. Okamura. Large eddy simualtion of unsteady flow in a mixed-flow pump. In *3rd ASME/JSME Joint Fluids Engeneering Conference*, pages 1–8, 1999.

[60] R.D. Keane and R.J. Adrian. Optimization of particle image velocimeters. Part I: Double pulsed systems. *Meas. Sci. Technology*, 1:1202–1215, 1990.

[61] R.D. Keane and R.J. Adrian. Theory of cross-correlation analysis of PIV images. *Applied Scientific Research*, 49:191–215, 1992.

[62] R.D. Keane, R.J. Adrian, and Y. Zhang. Super-resolution particle imaging velocimetry. *Meas. Sci. Technology*, 6:754–768, 1995.

[63] C. Lacor, P. Alavilli, Ch. Hirsch, P. Eliasson, I. Lindblad, and A. Rizzi. Hypersonic Navier-Stokes computations about complex configurations. In Ch Hirsch, editor, *Proceedings from First European CFD conference*, volume 2, pages 1089–1096, 1992.

[64] E. Lennemann. *Secondary flows in rotating passages.* PhD thesis, University of Waterloo, Waterloo, Ontario, Canada, 1969.

[65] E. Lennemann and J.H.G. Howard. Unsteady flow phenomena in centrifugal impeller passages. *J. Eng. Power*, 92(1):65–72, 1970.

[66] M. Lesieur and O. Métais. Neew trends in large-eddy simulations of turbulence. *Ann. Rev. Fluid Mech.*, 28:45–82, 1996.

[67] D. K. Lilly. A proposed modification of the Germano subgrid-scale closure method. *Phys. Fluids.*, A 4(3):633–635, 1992.

[68] C.H. Liu, C. Vafidis, and J.H. Whitelaw. Flow characteristics of a centrifugal pump. *J. Fluids Engng.*, 116:303–309, 1994.

[69] S. Liu, C. Meneveau, and J. Katz. On the properties of similarity subgrid-scale models as deduced from measurements in a turbulent jet. *J. Fluid Mech.*, 275:83–119, 1994.

[70] L. Lourenco and A. Krothapalli. On the accuracy of velocity and vorticity measurements with PIV. *Exp. Fluids*, 18:421–428, 1995.

[71] J.D. Luff, T. Drouillard, A.M. Rompage, M.A. Linne, and J.R. Hertzberg. Experimental uncertainties associated with particle image velocimetry (PIV) based vorticity algorithms. *Exp. Fluids*, 26:36–54, 1999.

[72] D. A. Lyn, S. Einav, W. Rodi, and J.-H. Park. A laser-doppler velocimetry study of ensemble-averaged characteristics of the turbulent near wake of a square cylinder. *J. Fluid Mech.*, 304:285–319, 1995.

[73] D.A. Lyn and W. Rodi. The flapping shear layer formed by flow separation from the forward corner of a square cylinder. *J. Fluid Mech.*, 267:353–376, 1994.

[74] O.J. McMillan and J.H. Ferziger. Direct testing of subgrid-scale models. *AIAA J.*, 17:1340, 1979.

[75] R. Mei. Velocity fidelity of flow tracer particles. *Exp. Fluids*, 22(1):1–13, 1996.

[76] A. Melling. Tracer particles and seeding for particle image velocimetry. *Exp. Fluids*, 8:1406–1416, 1996.

[77] C. Meneveau. Statistics of turbulence subgrid-scale stresses: Necessary conditions and experimental tests. *Phys. Fluids.*, 6(2):815–833, 1994.

[78] C. Meneveau and J. Katz. Dynamic testing of subgrid models in large eddy simulation based on the germano identity. *Phys. Fluids.*, 11(2):245–247, 1999.

[79] C. Meneveau, T. Lund, and W. Cabot. A lagrangian dynamic subgrid-scale model of turbulence. *J. Fluid Mech.*, 319:353, 1996.

[80] S.M. Miner, R.J. Beaudoin, and R.D. Flack. Laser velocimeter measurements in a centrifugal flow pump. *J. of Turbomachinery*, 111:205–212, 1989.

[81] J. Moore. A wake and an eddy in a rotating, radial-flow passage. Part 1: Experimental observations. *J. Eng. Power*, 95:205–212, 1973.

[82] J. Moore. A wake and an eddy in a rotating, radial-flow passage. Part 2: Flow model. *J. Eng. Power*, 95:213–219, 1973.

[83] S.P. Müeller. Secondary flows in a curved channel. Master's thesis, Department of Energy Engineering, Technical University of Denmark, Copenhagen, Denmark, 1998. EP 98-23.

[84] F.A. Muggli, K. Eisele, M.V. Casey, Gülich, and A. Schachenmann. Flow analysis in a pump diffuser - Part 2: Validation and limitations of CFD for diffusor flows. *J. of Turbomachinery*, 119:978–984, 1997.

[85] S. Murakami and A. Mochida. On turbulent vortex shedding flow past 2D square cylinder predicted by CFD. *J. Wind Engng. and Industrial Aerodynamics*, 54/55:191–211, 1995.

[86] J. S. Murray, U. Piomelli, and J. M. Wallace. Spatial and temporal filtering of experimental data for a priori studies of subgrid-scale stresses. *Phys. Fluids.*, 8(7):1978–1980, 1996.

[87] S. Nakagawa, K. Nitta, and M. Senda. An experimental study on unsteady turbulent near wake of a rectangular cylinder in channel flow. *Exp. Fluids*, 27: 284–294, 1999.

[88] A. Okajima. Strouhal numbers of rectangular cylinders. *J. Fluid Mech.*, 123: 379–398, 1982.

[89] M. Oldenburg and E. Pap. Velocity measurements in the impeller and in the volute of a centrifugal pump by Particle Image Displacement Velocimetry. In *Proceedings of the 8th International Symposium on Applications of Laser Techniques to Fluid Mechanics*, pages 8.2.1–8.2.5, Lisbon, Portugal, 1996.

[90] J. O'Neil and C. Meneveau. Subgrid-scale stresses and their modelling in a turbulent plane wake. *J. Fluid Mech.*, 349:253–293, 1997.

[91] N. Paone, M.L. Riethmuller, and R. Van den Braembussche. Application of Particle Image Displacement Velocimetry to a centrifugal pump. *4th Intl. Symp. on Appl. of Laser Techniques to Fluid Mechanics*, page 6, 1988.

[92] C. Pfleiderer and H. Petermann. *Strömungsmaschinen*. Springer Verlag, Berlin, 6th edition, 1998. (In german).

[93] U. Piomelli, C.H. Cabot, P. Moin, and S. Lee. Subgrid-scale backscatter in turbulent and transitional flows. *Phys. Fluids.*, A 3:1766, 1991.

[94] U. Piomelli, G.N. Coleman, and J. Kim. On the effects of nonequilibrium on the subgrid-scale stresses. *Phys. Fluids.*, 9(9):2740–2748, 1997.

[95] U. Piomelli and J. Liu. Large-eddy simulation of rotating channel flow using a localized dynamic model. *Phys. Fluids.*, 7(4):839–848, 1995.

[96] U. Piomelli, P. Moin, and J.H. Ferziger. Model consistency in large eddy simulations of turbulent channel flows. *Phys. Fluids.*, 31:1884, 1988.

[97] U. Piomelli, Y. Yu, and R.J. Adrian. Subgrid-scale energy transfer and near-wall turbulence structure. *Phys. Fluids.*, 8(1):215–224, 1996.

[98] A.K. Prasad. Stereoscopic particle image velocimetry. *Exp. Fluids*, 29:103–116, 2000.

[99] M. Raffel, C. Willert, and J. Kompenhans. *Particle Image Velocimetry - A Practical Guide*. Springer Verlag, 1998.

[100] J. Revstedt. *On the Modelling of Turbulent Flow and Mixing in Stirred Reactors*. PhD thesis, Lund Institute of Technology, Dept. of Heat and Power Engineering/Fluid Mechanics, 1999.

[101] W. Rodi. Comparison of LES and RANS calculations of the flow around bluff bodies. *J. Wind Engng. and Industrial Aerodynamics*, 69-71:55–75, 1997.

[102] W. Rodi, J.H. Ferziger, M. Breuer, and M. Pourquie. Status of Large Eddy Simulation: Results of a Workshop. *J. Fluids Engng.*, 119:248–262, 1997.

[103] R.S. Rogallo and P. Moin. Numerical simulation of turbulent flows. *Ann. Rev. Fluid Mech.*, 16:99–137, 1984.

[104] F. Sarghini, U. Piomelli, and E. Balaras. Scale-similar models for large-eddy simulations. *Phys. Fluids.*, 11(6):1596–1607, 1999.

[105] F. Scarano and M.L. Riethmuller. Iterative multigrid approach in PIV image processing with discrete window offset. *Exp. Fluids*, 26:513–523, 1999.

[106] M. Sinha, J. Katz, and C. Meneveau. Quantitative visualization of the flow in a centrifugal pump with diffuser vanes - I: On flow structures and turbulence. *J. Fluids Engng.*, 122:97–107, 2000.

[107] J. Smagorinsky. General circulation experiments with primitive equations, 1, The basic equations. *Mon. Weather Review*, 91:99–165, 1963.

[108] A.G. Smith. On the generation of the streamwise component of vorticity for flows in rotating passages. *Aeronautical Quarterly*, 8:369–383, 1957.

[109] A. Sohankar. *Numerical study of laminar, transitional and turbulent flow past rectangular cylinders*. PhD thesis, Dept. of Thermo and Fluid Dynamics, Chalmers University of Technology, Gothenburg, Sweden, 1998.

[110] Ch. Song and X. Chen. Simulation of flow through Francis turbine by LES method. In E. Cabrera, V. Espert, and F. Matinez, editors, *XVIII IAHR Symposium on Hydraulic Machinary and Cavitation*, volume 1, pages 267–276. Kluwer Academic Publisher, 1996.

[111] M. Stanislas and J.C. Monnier. Practical aspects of image recording in particle image velocimetry. *Meas. Sci. Technology*, 8:1417–1426, 1997.

[112] A.J. Stepanoff. *Centrifugal and axial flow pumps*. John Wiley & Sons, Inc., 2nd edition, 1957.

[113] A.M.K.P. Taylor, J.H. Whitelaw, and M. Yianneskis. Curved ducts with strong secondary motion: Velocity measurements of developing laminar and turbulent flow. *J. Fluids Engng.*, 104:350–359, 1982.

[114] H. Tennekes and J. L. Lumley. *A First Course in Turbulence*. The MIT Press, Cambridge, Massachusetts, 12th edition, 1974.

[115] M. Ubaldi, P. Zunino, and A. Cattanei. Relative flow and turbulence measurements downstream of a backward centrifugal impeller. *J. of Turbomachinery*, 115:543–551, 1993.

[116] M. Ubaldi, P. Zunino, and A. Ghiglione. Detailed flow measurements within the impeller and the vaneless diffuser of a centrifugal turbomachine. *Exp. Thermal and Fluid Science*, 17:147–155, 1998.

[117] U. Ullum. *Imaging techniques for planar velocity and concentration measurements*. PhD thesis, Dept. of Energy Engineering, Fluid Mechanics Section, Technical University of Denmark, Copenhagen, Denmark, 1999. ET-PHD 1999-03, ISBN 87-7475-223-5.

[118] U. Ullum, J.J. Schmidt, P.S. Larsen, and D.R. McCluskey. Temporal evolution of the perturbed and unperturbed flowfield behind a fence: PIV analysis and comparison with LDA data. *7th International conference on laser anemometry advances and applications*, 1997.

[119] U. Ullum, J.J. Schmidt, P.S. Larsen, and D.R. McCluskey. Statistical analysis and accuracy of PIV data. *Journal of Visualization*, 1(2):205–216, 1998.

[120] F.C. Visser, J.J.H. Brouwers, and J.B. Jonker. Fluid flow in a rotating low-specific-speed centrifugal impeller passage. *Fluid Dynamics Research*, 24: 275–292, 1999.

[121] M.P. Wernet. Development of digital particle imaging velocimetry for use in turbomachinery. *Exp. Fluids*, 28:97–115, 2000.

[122] J. Westerweel. *Digital Particle Image Velocimetry - Theory and Application*. PhD thesis, Delft University of Technology, Delft, The Netherlands, 1993.

[123] J. Westerweel. Efficient detection of spurious vectors in particle image velocimetry. *Exp. Fluids*, 16:236–247, 1994.

[124] J. Westerweel. Fundamentals of digital particle image velocimetry. *Meas. Sci. Technology*, 8:1379–1392, 1997.

[125] J. Westerweel. Effect of sensor geometry on the performance of PIV interrogation. In *9th Intl. Symp. on Appl. of Laser Techniques to Fluid Mechanics*, pages 1.2.1–1.2.8, 1998.

[126] J. Westerweel, D. Dabiri, and M. Gharib. The effect of a discrete window offset on the accuracy of cross-correlation analysis of PIV recordings. *Exp. Fluids*, 23:20–28, 1997.

[127] C.E. Willert and M. Gharib. Digital particle image velocimetry. *Exp. Fluids*, 10:181–193, 1991.

[128] J. Wu, J. Sheridan, M.C. Welsh, and K. Hourigan. Three-dimensional vortex structures in a cylinder wake. *J. Fluid Mech.*, 312:201–222, 1996.

[129] Y. Yoshida, Y. Murakami, T. Tsurusaki, and Y. Tsujimoto. Rotating stalls in centrifugal impeller/vaned diffuser systems. In *Proc First ASME/JSME Joint Fluids Eng. Conf.*, pages 125–130, 1991.

[130] Y. Zang, R.L. Street, and J.R. Koseff. A dynamic mixed subgrid-scale model and its application to turbulent recirculating flows. *Phys. Fluids.*, A 5(12): 3186–3196, 1993.

[131] M. Zangeneh, A. Goto, and H. Harada. On the design criteria for suppression of secondary flows in centrifugal and mixed flow impellers. In *International Gas Turbine and Aeroengine Congress and Exhibition*, 1997.